

# Scale dependence of galaxy biasing investigated by weak gravitational lensing: An assessment using semi-analytic galaxies and simulated lensing data

Patrick Simon<sup>1</sup> and Stefan Hilbert<sup>2,3</sup>

<sup>1</sup> Argelander-Institut für Astronomie, Universität Bonn, Auf dem Hügel 71, 53121 Bonn, Germany

<sup>2</sup> Faculty of Physics, Ludwig-Maximilians University, Scheinerstr. 1, 81679 München, Germany

<sup>3</sup> Excellence Cluster Universe, Boltzmannstr. 2, 85748 Garching, Germany

e-mail: psimon@astro.uni-bonn.de

Received July 24, 2019

## ABSTRACT

Galaxies are biased tracers of the matter density on cosmological scales. For future tests of galaxy models, we refine and assess a method to measure galaxy biasing as function of physical scale  $k$  with weak gravitational lensing. This method enables us to reconstruct the galaxy bias factor  $b(k)$  as well as the galaxy-matter correlation  $r(k)$  on spatial scales between  $0.01 h \text{ Mpc}^{-1} \lesssim k \lesssim 10 h \text{ Mpc}^{-1}$  for redshift-binned lens galaxies below redshift  $z \lesssim 0.6$ . In the refinement, we account for an intrinsic alignment of source ellipticities, and we correct for the magnification bias of the lens galaxies, relevant for the galaxy-galaxy lensing signal, to improve the accuracy of the reconstructed  $r(k)$ . For simulated data, the reconstructions achieve an accuracy of 3 – 7% (68% confidence level) over the above  $k$ -range for a survey area and a typical depth of contemporary ground-based surveys. Realistically the accuracy is, however, probably reduced to about 10 – 15%, mainly by systematic uncertainties in the assumed intrinsic source alignment, the fiducial cosmology, and the redshift distributions of lens and source galaxies (in that order). Furthermore, our reconstruction technique employs physical templates for  $b(k)$  and  $r(k)$  that elucidate the impact of central galaxies and the halo-occupation statistics of satellite galaxies on the scale-dependence of galaxy bias, which we discuss in the paper. In a first demonstration, we apply this method to previous measurements in the Garching-Bonn-Deep Survey and give a physical interpretation of the lens population.

**Key words.** gravitational lensing: weak – (cosmology:) large-scale structure of the Universe – galaxies: statistics

## 1. Introduction

The standard paradigm of cosmology describes the large-scale distribution of matter and galaxies in an expanding Universe (Dodelson 2003, and references therein). Strongly supported by observations, this model assumes a statistically homogeneous and isotropic Universe with cold dark matter (CDM) as dominating form of matter. Matter in total has the mean density  $\Omega_m \approx 0.3$  of which ordinary baryonic matter is just  $\Omega_b \approx 0.05$ ; as usual densities are in units of the critical density (or its energy equivalent). The largest fraction  $\Omega_\Lambda \approx 0.7$  in the cosmological energy density is given by a cosmological constant  $\Lambda$  or so-called dark energy, resulting in a flat or approximately flat background geometry with curvature parameter  $K = 0$  (Einstein 1917; Planck Collaboration et al. 2016, and references therein). The exact physical nature of dark matter is unknown but its presence is consistently inferred through visible tracers from galactic to cosmological scales at different epochs in the cosmic history (Bertone et al. 2005, for a review). In particular the coherent shear of distant galaxy images (background sources) by the tidal gravitational field of intervening matter gives direct evidence for the (projected) density field of dark matter (Clowe et al. 2004). The basic physics of galaxy formation inside dark-matter halos and the galaxy evolution seems to be identified and reasonably well matched by observations although various processes, such as star formation and galaxy-gas feedback, are still not well understood or worked out in detail (Mo et al. 2010). Ultimately,

the ability of the  $\Lambda$ CDM model to quantitatively describe the observed richness of galaxy properties from initial conditions will be a crucial validation test.

One galaxy property of importance is their spatial distribution. Galaxies are known to be differently distributed than the matter in general; they are so-called biased tracers of the matter density field (Kaiser 1984). The details of the biasing mechanism are related to galaxy physics (Springel et al. 2017, 2005; Weinberg et al. 2004; Somerville et al. 2001; Benson et al. 2000; Peacock & Smith 2000). An observed galaxy bias for different galaxy types and redshifts consequently provides input and tests for galaxy models. Additionally, its measurement is practical for studies that rely on fiducial values for the biasing of a particular galaxy sample or on the observational support for a high galaxy-matter correlation on particular spatial scales (e.g. van Uitert et al. 2017; Hildebrandt et al. 2013; Simon 2013; Mehta et al. 2011; Reyes et al. 2010; Baldauf et al. 2010). In this context, we investigate the prospects of weak gravitational lensing to measure the galaxy bias (e.g. Kilbinger 2015; Munshi et al. 2008; Schneider et al. 2006, for a review).

There are clearly various ways to express the statistical relationship between the galaxy and matter distribution, which both can be seen as realisations of statistically homogeneous and isotropic random fields (Desjacques et al. 2016). With focus on second-order statistics we use the common parameterisation in Tegmark & Bromley (1999). This defines galaxy bias in terms of auto- and cross-correlation power spectra of the random fields

for a given wave number  $k$ : (i) a bias factor  $b(k)$  for the relative strength between galaxy and matter clustering; and (ii) a factor  $r(k)$  for the galaxy-matter correlation. The second-order biasing functions can be constrained by combining galaxy clustering with cosmic-shear information in lensing surveys (Foreman et al. 2016; Cacciato et al. 2012; Simon 2012; Pen et al. 2003). In applications of these techniques, galaxy biasing is then known to depend on galaxy type, physical scale, and redshift, thus reflecting interesting galaxy physics (Chang et al. 2016; Buddendiek et al. 2016; Pujol et al. 2016; Prat et al. 2016; Comparat et al. 2013; Simon et al. 2013; Jullo et al. 2012; Simon et al. 2007; Pen et al. 2003; Hoekstra et al. 2002).

Our interest here is the quality of lensing measurements of galaxy bias. For this purpose, we focus on the method by van Waerbeke (1998) and Schneider (1998), first applied in Hoekstra et al. (2001) and Hoekstra et al. (2002), where one defines relative aperture measures of the galaxy number-density and the lensing mass to observe  $b(k)$  and  $r(k)$  as projections on the sky, averaged in bands of radial and transverse direction. The advantage of this method is its model independence apart from a cosmology-dependent normalisation. As improvement we define a new procedure to deproject the lensing measurements of the projected biasing functions, giving direct estimates of  $b(k)$  and  $r(k)$  for a selected galaxy population. In addition, we account for the intrinsic alignment of source galaxies that are utilised in the lensing analysis (Kirk et al. 2015). To eventually assess the accuracy and precision of our deprojection technique, we compare the results to the true biasing functions for various galaxy samples in a simulated, about  $1000 \text{ deg}^2$  wide survey, constructed with a semi-analytic galaxy model by Henriques et al. (2015), H15 hereafter, and data from the Millennium Simulation (Springel et al. 2005). To this end, a large part of this paper deals with the construction of flexible template models of  $b(k)$  and  $r(k)$  that we forward-fit to the relative aperture measures. These templates are based on a flexible halo-model prescription, which additionally allows us a physical interpretation of the biasing functions (Cooray & Sheth 2002). Some time is therefore also spent on a discussion of the scale-dependence of galaxy bias which will be eminent in future applications of our technique.

The structure of this paper is as follows. In Sect. 2, we describe the construction of data for a mock lensing survey to which we apply our deprojection technique. With respect to number densities of lens and source galaxies on the sky, the mock data are similar to realistic galaxy samples in the Canada-France-Hawaii Telescope Lensing Survey, CFHTLenS hereafter (Heymans et al. 2012). We increase the simulated survey area, however, to  $\sim 1000 \text{ deg}^2$  in order to assess the quality of our methodology for state-of-the-art (ground-based) surveys in future applications. In Sect. 3, we revise the relation of the spatial biasing functions to their projected counterparts which are observable through the aperture statistics. This section also adds to the technique of Hoekstra et al. (2002) as novelty potentially relevant higher-order corrections in the lensing formalism. It also incorporates a treatment of the intrinsic alignment of sources into the aperture statistics. Section 4 derives our template models of the spatial biasing functions, applied for a deprojection; Section 5 summarises the template parameters and explores their impact on the scale dependence of galaxy bias. The methodological details for the statistical inference of  $b(k)$  and  $r(k)$  from noisy measurements are presented in Sect. 6. We apply this inference technique to the mock data in the result Sect. 7 and assess its accuracy, precision, and robustness. As a first demonstration, we

**Table 1.** Selection criteria applied to our mock galaxies to emulate stellar-mass samples consistent with SES13 and for the two additional colour-selected samples RED and BLUE. The samples are further subdivided, as in SES13, into the two redshift bins low- $z$  ( $\bar{z} \approx 0.36$ ) and high- $z$  ( $\bar{z} \approx 0.52$ ) by a emulated selection in photometric redshift  $z_p$ . The redshift distributions of all samples are summarised by Fig. 1. The sample SOURCES is used as background sample for the mock lensing-analysis.

Galaxy Sample	Selection <sup>a</sup>
SM1	$0.5 \leq M_* < 1; i' < 22.5$
SM2	$1 \leq M_* < 2; i' < 22.5$
SM3	$2 \leq M_* < 4; i' < 22.5$
SM4	$4 \leq M_* < 8; i' < 22.5$
SM5	$8 \leq M_* < 16; i' < 22.5$
SM6	$16 \leq M_* < 32; i' < 22.5$
RED	$u - r > 1.93z + 1.85; i' < 22.5;$ $0.5 \leq M_* < 32$
BLUE	$u - r \leq 1.93z + 1.85; i' < 22.5;$ $0.5 \leq M_* < 32$
SOURCES	$i' \leq 24.7; 0.65 \leq z_p < 1.2$

**Notes.** <sup>(a)</sup>  $M_*$  refers to the stellar mass in units of  $10^{10} M_\odot$ ;  $i', u, r$  are apparent magnitudes as defined for CFHTLenS (Erben et al. 2013);  $z$  is the (cosmological) galaxy redshift;  $z_p$  is a photometric redshift with errors similar to CFHTLenS

apply our technique to previous measurements in Simon et al. (2007). We finally discuss our results in Sect. 8.

## 2. Data

This section details our mock data, that is lens and source catalogues, to which we apply our deprojection technique in the following sections. A reader more interested in the method details for the recovery of galaxy bias with lensing data could proceed to the next sections.

### 2.1. Samples of lens galaxies

Our galaxy samples use a semi-analytic model (SAM) according to H15 which is implemented on the Millennium Simulation (Springel et al. 2006). These SAMs are the H15 mocks that are also used in Saghiha et al. (2017). The Millennium Simulation (MS) is a  $N$ -body simulation of the CDM density field inside a comoving cubic volume of  $500 h^{-1} \text{ Mpc}$  side length, and it has a spatial resolution of  $5 h^{-1} \text{ kpc}$  sampled by  $10^{10}$  mass particles. The fiducial cosmology of the MS has the density parameters  $\Omega_m = 0.25 = 1 - \Omega_\Lambda$  and  $\Omega_b = 0.045$ ,  $\sigma_8 = 0.9$  for the normalisation of the linear matter power-spectrum, a Hubble parameter  $H_0 = 100 h \text{ km s}^{-1} \text{ Mpc}^{-1}$  with  $h = 0.73$ , and a spectral index for the primordial matter-power spectrum of  $n_{\text{spec}} = 1.0$ . All density parameters are in units of the critical density  $\bar{\rho}_{\text{crit}} = 3H_0^2/8\pi G_N$  where  $G_N$  denotes Newton's constant of gravity. The galaxy mocks are constructed by populating dark matter halos in the simulation based on the merger history of halos and in accordance with the SAM details. We project the

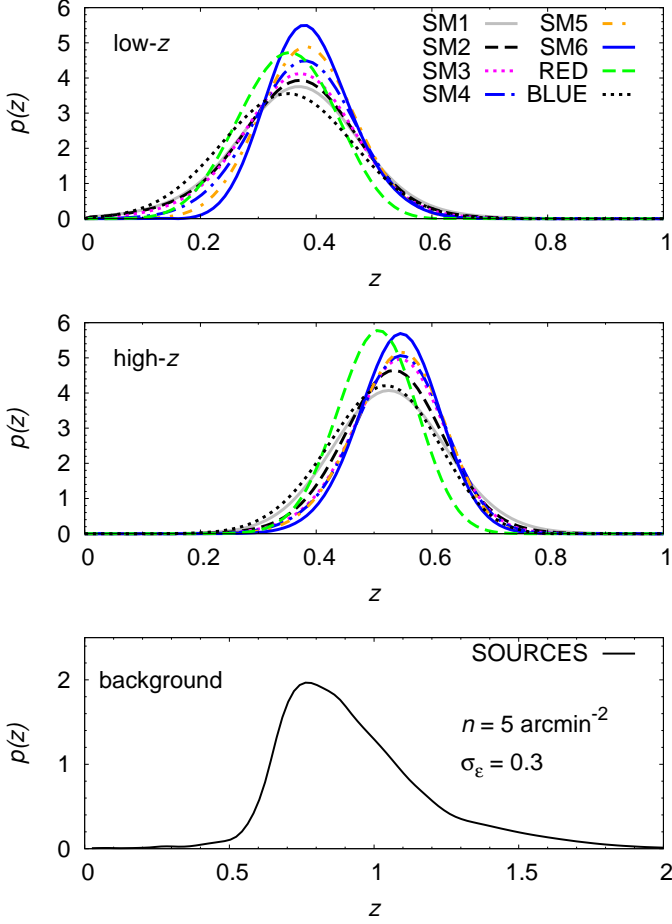


**Fig. 1.** Models of the probability densities  $p_d(z)$  of galaxy redshifts in our lens samples SM1 to SM6, RED and BLUE (two top panels), and the density  $p_s(z)$  of the source sample (bottom panel).

positions of the SAMs inside 64 independent light cones onto a  $4 \times 4 \text{ deg}^2$  piece of sky. The resulting total survey area is hence  $1024 \text{ deg}^2$ .

We then select galaxies from the mocks to emulate the selection in redshift and stellar mass in Simon et al. (2013), SES13 henceforth. Details on the emulation process can be found in Saghiha et al. (2017). We give only a brief summary here. The mock-galaxy and source samples are constructed to be compatible with those in recent lensing studies, dealing with data from the Canada-France-Hawaii Telescope Survey, CFHTLenS hereafter (Saghiha et al. 2017; Velander et al. 2014; Erben et al. 2013; Heymans et al. 2012). Our selection proceeds in two steps. First, we split the galaxy catalogues in stellar mass, including emulated measurement errors, and  $i'$ -band brightness to produce the stellar-mass samples SM1 to SM6; the photometry uses the AB-magnitude system. Second, we randomly discard galaxies in each stellar-mass sample to obtain a redshift distribution that is comparable to a given target distribution. As targets, we employ the photometric redshift bins ‘low- $z$ ’ and ‘high- $z$ ’ in SES13 which are the redshift distributions in CFHTLenS after a cut in photometric redshift  $z_p$ . The low- $z$  bin applies  $0.2 \leq z_p < 0.44$ , and the high- $z$  bin applies  $0.44 \leq z_p < 0.6$ . See Fig. 5. in SES13 for the different target distributions. Our selection criteria for SM1 to SM6 are listed in Table 1. We note here that randomly removing galaxies at redshift  $z$  adds shot noise but does not

change the matter-galaxy correlations and the (shot-noise corrected) galaxy clustering.

In addition to SM1-6, we define two more samples RED and BLUE based on the characteristic bimodal distribution of  $u-r$  colours (Table 1). Both samples initially consist of all galaxies in SM1 to SM6 but are then split depending on the  $u-r$  colours of galaxies: the division is at  $(u-r)(z) = 1.93z + 1.85$  which varies with  $z$  to account for the reddening with redshift. We crudely found  $(u-r)(z)$  by identifying by eye the mid-points  $(u-r)_i$  between the red and blue mode in  $u-r$  histograms of CFHTLenS<sup>1</sup> SM1-6 galaxies in four photometric-redshift bins with means  $\{z_i\} = \{0.25, 0.35, 0.45, 0.55\}$  and width  $\Delta z = 0.1$  (Hildebrandt et al. 2012). Then we fit a straight line to the four empirical data points  $\{(z_i, (u-r)_i)\}$  and obtain the above  $(u-r)(z)$  as best-fit. For splitting the mocks, we identify the precise redshifts  $z$  in H15 with the photometric redshifts  $z_p$  in CFHTLenS which, for the scope of this work, is a sufficient approximation. Similar to the previous stellar-mass samples, we combine the redshift posteriors of all CFHTLenS-galaxies RED or BLUE to define the target distributions for our corresponding mock samples.

For the following galaxy-bias analysis, we estimate the probability density function (PDF)  $p_d(z)$  of each galaxy sample from the mock catalogues in the foregoing step. Simply using histograms of the sample redshifts may seem like a good idea but are, in fact, problematic because the histograms depend on the adopted binning. This is especially relevant for the prediction of galaxy clustering which depends on  $p_d^2(z)$  (see Eq. 22). Instead, we fit for  $p_d(z)$  a smooth four-parameter Gram-Charlier series

$$p_d(z|\lambda, \Theta) = \lambda e^{-\frac{z^2}{2}} \left( 1 + \frac{s}{6} H_3(x) + \frac{k}{24} H_4(x) \right); \quad x = \frac{z - \bar{z}}{\sigma_z} \quad (1)$$

with the Hermite polynomials  $H_3(x) = x^3 - 3x$  and  $H_4(x) = x^4 - 6x^2 + 3$  to a mock sample  $\{z_i : i = 1 \dots n\}$  of  $n$  galaxy redshifts;  $\lambda$  is a normalisation constant that depends on the parameter combination  $\Theta = (\bar{z}, \sigma_z, s, k)$  and is defined by

$$\int_0^\infty dz p_d(z|\lambda, \Theta) = 1. \quad (2)$$

For an estimate  $\hat{\Theta}$  of the parameters  $\Theta$ , we maximise the log-likelihood

$$\ln \mathcal{L}(\Theta) = \sum_{i=1}^n \ln p_d(z_i|\lambda, \Theta) \quad (3)$$

with respect to  $\Theta$ . This procedure selects the PDF  $p_d(z|\lambda, \hat{\Theta})$  that is closest to the sample distribution of redshifts  $z_i$  in a Kullback-Leibler sense (Knight 1999). The mean  $\bar{z}$  and variance  $\sigma_z^2$  in the fit matches that of the redshift distribution in the mock lens sample. The resulting densities for all our lens samples are shown in the two top panels of Fig. 1.

## 2.2. Shear catalogues

For mock source catalogues based on the MS data, we construct lensing data by means of multiple-lens-plane ray-tracing as described in Hilbert et al. (2009). The ray-tracing produces the lensing convergence  $\kappa(\theta|z_s)$  and shear distortion  $\gamma(\theta|z_s)$  for  $4096^2$  line-of-sight directions  $\theta$  on 64 regular angular grids and a sequence of  $n_s = 31$  source redshifts  $z_{s,i}$  between  $z_s = 0$  and  $z_s = 2$ ; we denote by  $\Delta z_i = z_{s,i+1} - z_{s,i}$  the difference between

<sup>1</sup> <http://cfhtlens.org>

neighbouring source redshifts. Each grid covers a solid angle of  $\Omega = 4 \times 4 \text{ deg}^2$ . For each grid, we then compute the average convergence for sources with redshift PDF  $p_s(z)$  by

$$\kappa(\theta) = \frac{\sum_{i=1}^{n_s} p_s(z_{s,i}) \Delta z_i \kappa(\theta|z_{s,i})}{\sum_{i=1}^{n_s} p_s(z_{s,i}) \Delta z_i}, \quad (4)$$

and the average shear  $\gamma(\theta)$  from the sequence  $\gamma(\theta|z_s)$  accordingly. For  $p_s(z)$ , we employ the estimated PDF of CFHTLenS sources that is selected through  $i' < 24.7$  and  $0.65 \leq z_p < 1.2$ , weighted by their shear-measurement error (SES13); see the bottom panel in Fig. 1. The mean redshift of sources is  $\bar{z} \approx 0.93$ . To assign source positions on the sky, we uniform-randomly pick a sample  $\{\theta_i : i = 1 \dots n\}$  of positions for each grid; the amount of positions is  $n = \Omega \bar{n}_s$  for a number density of  $\bar{n}_s = 5 \text{ arcmin}^{-2}$  sources which roughly equals the effective number density of sources in SES13.

Depending on the type of our lensing analysis, we assign a source at  $\theta_i$  one of the following three values for the simulated sheared ellipticity  $\epsilon_i$ : (i)  $\epsilon_i = \gamma(\theta_i)$  for source without shape noise; (ii)  $\epsilon_i = A(\gamma(\theta_i), \epsilon_s)$  for noisy sources with shear; and (iii)  $\epsilon_i = A(g_i, \epsilon_s)$  for noisy sources with reduced shear  $g_i = \gamma(\theta_i)/[1 - \kappa(\theta_i)]$ . We define here by  $A(x, y) := (x + y)(1 + xy^*)^{-1}$  the conformal mapping of two complex numbers  $x$  and  $y$ , and by  $\epsilon_s$  a random shape-noise drawn from a bivariate, truncated Gaussian PDF with zero mean, 1D dispersion  $\sigma_\epsilon = 0.3$ , and an exclusion of values beyond  $|\epsilon_s| \geq 1$ .

### 2.3. Power spectra

We obtain the true spatial galaxy-galaxy, galaxy-matter, and matter-matter power spectra for all galaxy samples at a given simulation snapshot with Fast Fourier Transform (FFT) methods. For a choice of pair of tracers (i.e. simulation matter particles or galaxies from different samples) in a snapshot, we compute a series of raw power spectra by ‘chaining the power’ (Smith et al. 2003). We cover the whole simulation volume as well as smaller subvolumes (by a factor  $4^3$  to  $256^3$ , into which the whole box is folded) by regular meshes of  $512^3$  points (providing a spatial resolution from  $\sim 1 h^{-1} \text{ Mpc}$  for the coarsest mesh to  $\sim 5 h^{-1} \text{ kpc}$  for the finest mesh). We project the tracers onto these meshes using clouds-in-cells (CIC) assignment (Hockney & Eastwood 1981).

We FFT-transform the meshes, record their raw power spectra, apply a shot-noise correction (except for cross-spectra), a deconvolution to correct for the smoothing by the CIC assignment, and an iterative alias correction (similar to what is described in Jing 2005). From these power spectra, we discard small scales beyond half their Nyquist frequency as well as large scales that are already covered by a coarser mesh, and combine them into a single power spectrum covering a range of scales from modes  $\sim 0.01 h \text{ Mpc}^{-1}$  to modes  $\sim 100 h \text{ Mpc}^{-1}$ .

The composite power spectra are then used as input to estimate alias corrections for the partial power spectra from the individual meshes with different resolutions, and the process is repeated until convergence. From the resulting power spectra, we then compute the true biasing functions, Eq. (10), which we compare to our lensing-based reconstructions in Sect. 7.

### 3. Projected biasing functions as observed with lensing techniques

The combination of suitable statistics for galaxy clustering, galaxy-galaxy lensing, and cosmic-shear correlations on the sky

allows us to infer, without a concrete physical model, the  $z$ -averaged spatial biasing-functions  $b(k)$  and  $r(k)$  as projections  $b_{2D}(\theta_{ap})$  and  $r_{2D}(\theta_{ap})$  for varying angular scales  $\theta_{ap}$ . Later on, we forward-fit templates of spatial biasing functions to these projected functions to perform a stable deprojection. We summarise here the relation between  $(b(k), r(k))$  and the observable ratio-statistics  $(b_{2D}(\theta_{ap}), r_{2D}(\theta_{ap}))$ . We include corrections to the first-order Born approximation for galaxy-galaxy lensing and galaxy clustering, and corrections for the intrinsic alignment of sources.

#### 3.1. Spatial biasing functions

We define galaxy bias in terms of two biasing functions  $b(k)$  and  $r(k)$  for a given spatial scale  $2\pi k^{-1}$  or wave number  $k$  in the following way. Let  $\delta(\mathbf{x})$  in  $\rho(\mathbf{x}) = \bar{\rho}[1 + \delta(\mathbf{x})]$  be the density fluctuations at position  $\mathbf{x}$  of a random density field  $\rho(\mathbf{x})$ , and  $\bar{\rho}$  denotes the mean density. A density field is either the matter density  $\rho_m(\mathbf{x})$  or the galaxy number density  $n_g(\mathbf{x})$  with density contrasts  $\delta_m(\mathbf{x})$  and  $\delta_g(\mathbf{x})$ , respectively. We determine the fluctuation amplitude for a density mode  $\mathbf{k}$  by the Fourier transform of  $\delta(\mathbf{x})$ ,

$$\tilde{\delta}(\mathbf{k}) = \int d^3x \delta(\mathbf{x}) e^{-i\mathbf{x} \cdot \mathbf{k}}. \quad (5)$$

All information on the two-point correlations of  $\tilde{\delta}(\mathbf{k})$  is contained in the power spectrum  $P(k)$  defined through the second-order correlation function of modes,

$$\langle \tilde{\delta}(\mathbf{k}) \tilde{\delta}(\mathbf{k}') \rangle = (2\pi)^3 \delta_D(\mathbf{k} + \mathbf{k}') P(k), \quad (6)$$

where  $k = |\mathbf{k}|$  is the scalar wave-number and  $\delta_D(s)$  is the Dirac Delta distribution. Specifically, we utilise three kinds of power spectra,

$$\langle \tilde{\delta}_m(\mathbf{k}) \tilde{\delta}_m(\mathbf{k}') \rangle = (2\pi)^3 \delta_D(\mathbf{k} + \mathbf{k}') P_m(k); \quad (7)$$

$$\langle \tilde{\delta}_m(\mathbf{k}) \tilde{\delta}_g(\mathbf{k}') \rangle = (2\pi)^3 \delta_D(\mathbf{k} + \mathbf{k}') P_{gm}(k); \quad (8)$$

$$\langle \tilde{\delta}_g(\mathbf{k}) \tilde{\delta}_g(\mathbf{k}') \rangle = (2\pi)^3 \delta_D(\mathbf{k} + \mathbf{k}') (P_g(k) + \bar{n}_g^{-1}), \quad (9)$$

namely the matter power spectrum  $P_m(k)$ , the galaxy-matter cross-power spectrum  $P_{gm}(k)$ , and the galaxy power-spectrum  $P_g(k)$ . The latter subtracts the shot-noise  $\bar{n}_g^{-1}$  from the galaxy power spectrum by definition. In contrast to the smooth matter density, the galaxy number-density is subject to shot noise because it consists of a finite number of discrete points that make up the number density field. Traditionally, the definition of  $P_g(k)$  assumes a Poisson process for the shot noise in the definition of  $P_g(k)$  (Peebles 1980).

The biasing functions (of the second order) express galaxy bias in terms of ratios of the foregoing power spectra,

$$b(k) := \sqrt{\frac{P_g(k)}{P_m(k)}}; \quad r(k) := \frac{P_{gm}(k)}{\sqrt{P_g(k) P_m(k)}}. \quad (10)$$

Galaxies that sample the matter density by a Poisson process have  $b(k) = r(k) = 1$  for all scales  $k$  and are dubbed ‘unbiased’; for  $b(k) > 1$ , we find that galaxies cluster stronger than matter at scale  $k$ , and vice versa for  $b(k) < 1$ ; a decorrelation of  $r(k) \neq 1$  indicates either stochastic bias, non-linear bias, a sampling process that is non-Poisson, or combinations of these cases (Dekel & Lahav 1999; Guzik & Seljak 2001).

### 3.2. Aperture statistics and galaxy-bias normalisation

The projected biasing functions  $b(k)$  and  $r(k)$  are observable by taking ratios of the (co-)variances of the aperture mass and aperture number count of galaxies (van Waerbeke 1998; Schneider 1998). To see this, let  $\kappa_g(\theta) = N_g(\theta)/\bar{N}_g - 1$  be the density contrast of the number density of galaxies  $N_g(\theta)$  on the sky in the direction  $\theta$ , and  $\bar{N}_g = \langle N_g(\theta) \rangle$  is their mean number density. We define the aperture number count of  $N_g(\theta)$  for an angular scale  $\theta_{\text{ap}}$  at position  $\theta$  by

$$\mathcal{N}(\theta_{\text{ap}}; \theta) = \int d^2\theta' U(|\theta'|; \theta_{\text{ap}}) \kappa_g(\theta' + \theta), \quad (11)$$

where

$$U(\theta; \theta_{\text{ap}}) = \frac{1}{\theta_{\text{ap}}^2} u(\theta \theta_{\text{ap}}^{-1}); \quad u(x) = \frac{9}{\pi} (1 - x^2) \left( \frac{1}{3} - x^2 \right) H(1 - x) \quad (12)$$

is the aperture filter of the density field, and  $H(x)$  is the Heaviside step function of our polynomial filter profile  $u(x)$ . The aperture filter is compensated, that is  $\int_0^\infty dx x u(x) = 0$ . Similarly for the (average) lensing convergence  $\kappa(\theta)$  of sources in direction  $\theta$ , the aperture mass is given by

$$M_{\text{ap}}(\theta_{\text{ap}}; \theta) = \int d^2\theta' U(|\theta'|; \theta_{\text{ap}}) \kappa(\theta' + \theta). \quad (13)$$

The aperture statistics consider the variances  $\langle \mathcal{N}^2 \rangle(\theta_{\text{ap}})$  and  $\langle M_{\text{ap}}^2 \rangle(\theta_{\text{ap}})$  of  $\mathcal{N}(\theta_{\text{ap}}; \theta)$  and  $M_{\text{ap}}(\theta_{\text{ap}}; \theta)$ , respectively, across the sky as well as their co-variance  $\langle \mathcal{N} M_{\text{ap}} \rangle(\theta_{\text{ap}})$  at zero lag.

From these observable aperture statistics, we obtain the galaxy-bias factor  $b_{2D}(\theta_{\text{ap}})$  and correlation factor  $r_{2D}(\theta_{\text{ap}})$  through the ratios

$$b_{2D}(\theta_{\text{ap}}) = \sqrt{\frac{\langle \mathcal{N}^2 \rangle(\theta_{\text{ap}})}{\langle M_{\text{ap}}^2 \rangle(\theta_{\text{ap}})}} \times f_b(\theta_{\text{ap}}), \quad (14)$$

$$r_{2D}(\theta_{\text{ap}}) = \frac{\langle \mathcal{N} M_{\text{ap}} \rangle(\theta_{\text{ap}})}{\sqrt{\langle \mathcal{N}^2 \rangle(\theta_{\text{ap}}) \langle M_{\text{ap}}^2 \rangle(\theta_{\text{ap}})}} \times f_r(\theta_{\text{ap}}), \quad (15)$$

where

$$f_b(\theta_{\text{ap}}) := \sqrt{\frac{\langle M_{\text{ap}}^2 \rangle_{\text{th}}(\theta_{\text{ap}})}{\langle \mathcal{N}^2 \rangle_{\text{th}}(\theta_{\text{ap}}; 1)}}, \quad (16)$$

$$f_r(\theta_{\text{ap}}) := \frac{\sqrt{\langle M_{\text{ap}}^2 \rangle_{\text{th}}(\theta_{\text{ap}}) \langle \mathcal{N}^2 \rangle_{\text{th}}(\theta_{\text{ap}}; 1)}}{\langle \mathcal{N} M_{\text{ap}} \rangle_{\text{th}}(\theta_{\text{ap}}; 1)} \quad (17)$$

normalise the statistics according to a fiducial cosmology, that means the aperture statistics with subscript ‘th’ as in  $\langle M_{\text{ap}}^2 \rangle_{\text{th}}(\theta_j)$  denote the expected (co-)variance for a fiducial model. The normalisation is chosen such that we have  $b_{2D}(\theta_{\text{ap}}) = r_{2D}(\theta_{\text{ap}}) = 1$  for unbiased galaxies given the distributions of lenses and sources with distance  $\chi$  as in the survey, hence the ‘ $(\theta_{\text{ap}}; 1)$ ’ in the arguments of the normalisation. The normalisation functions  $f_i$  and  $f_b$  are typically weakly varying with angular scale  $\theta_{\text{ap}}$  (Hoekstra et al. 2002). In addition, they depend weakly on the fiducial matter power spectrum  $P_m(k; z)$ ; they are even invariant with respect to an amplitude change  $P_m(k; z) \mapsto \nu P_m(k; z)$  with some number  $\nu > 0$ . We explore the dependence on the fiducial cosmology quantitatively in Sect. 7.3.

For this study, we assume that the distance distribution of lenses is sufficiently narrow, which means that the bias evolution in the lens sample is negligible. We therefore skip the argument  $\chi$  in  $b(k; \chi)$  and  $r(k; \chi)$ , and we use a  $b(k)$  and  $r(k)$  independent of  $\chi$  for average biasing functions instead.

The relation between  $(b(k), r(k))$  and  $(b_{2D}(\theta_{\text{ap}}), r_{2D}(\theta_{\text{ap}}))$  is discussed in the following. Let  $p_d(\chi) d\chi$  and  $p_s(\chi) d\chi$  be the probability to find a lens or source galaxy, respectively, at comoving distance  $[\chi, \chi + d\chi]$ . The matter power spectrum at distance  $\chi$  shall be  $P_m(k; \chi)$ , and  $k_\ell^\chi := (\ell + 0.5)/f_K(\chi)$  is a shorthand for the transverse spatial wave-number  $k$  at distance  $\chi$  that corresponds to the angular wave-number  $\ell$ . The function  $f_K(\chi)$  denotes the comoving angular-diameter distance in the given fiducial cosmological model. The additive constant 0.5 in  $k_\ell^\chi$  applies a correction to the standard Limber approximation on the flat sky which gives more accurate results for large angular scales (Kilbinger et al. 2017; Loverde & Afshordi 2008). According to theory, the aperture statistics are then

$$\langle \mathcal{N}^2 \rangle_{\text{th}}(\theta_{\text{ap}}; b) = 2\pi \int_0^\infty d\ell \ell P_n(\ell; b) [I(\ell \theta_{\text{ap}})]^2, \quad (18)$$

$$\langle \mathcal{N} M_{\text{ap}} \rangle_{\text{th}}(\theta_{\text{ap}}; b, r) = 2\pi \int_0^\infty d\ell \ell P_{nk}(\ell; b, r) [I(\ell \theta_{\text{ap}})]^2, \quad (19)$$

$$\langle M_{\text{ap}}^2 \rangle_{\text{th}}(\theta_{\text{ap}}) = 2\pi \int_0^\infty d\ell \ell P_k(\ell) [I(\ell \theta_{\text{ap}})]^2, \quad (20)$$

with the angular band-pass filter

$$I(x) := \int_0^\infty ds s u(s) J_0(sx) = \frac{12}{\pi} \frac{J_4(x)}{x^2}, \quad (21)$$

the angular power spectrum of the galaxy clustering

$$P_n(\ell; b) = \int_0^{\chi_h} \frac{d\chi P_d^2(\chi)}{f_K^2(\chi)} b^2(k_\ell^\chi) P_m(k_\ell^\chi; \chi), \quad (22)$$

the galaxy-convergence cross-power

$$P_{nk}(\ell; b, r) = \frac{3H_0^2 \Omega_m}{2c^2} \int_0^{\chi_h} \frac{d\chi p_d(\chi) g_s(\chi)}{a(\chi) f_K(\chi)} b(k_\ell^\chi) r(k_\ell^\chi) P_m(k_\ell^\chi; \chi), \quad (23)$$

and the convergence power-spectrum

$$P_k(\ell) = \frac{9H_0^4 \Omega_m^2}{4c^4} \int_0^{\chi_h} \frac{d\chi g_s^2(\chi)}{a^2(\chi)} P_m(k_\ell^\chi; \chi), \quad (24)$$

all in the Born and Limber approximation. In the integrals, we use the lensing kernel

$$g_s(\chi) = \int_\chi^{\chi_h} d\chi' p_s(\chi') \frac{f_K(\chi' - \chi)}{f_K(\chi')}, \quad (25)$$

the scale factor  $a(\chi)$  at distance  $\chi$ , the maximum distance  $\chi_h$  of a source, and the  $n$ th-order Bessel function  $J_n(x)$  of the first kind. By  $c$  we denote the vacuum speed of light. The power spectra

and aperture statistics depend on specific biasing functions as indicated by the  $b$  and  $r$  in the arguments. For given biasing functions  $b(k)$  and  $r(k)$ , we obtain the normalised galaxy bias inside apertures therefore through

$$b_{2D}(\theta_{ap}; b) = \sqrt{\frac{\langle N^2 \rangle_{th}(\theta_{ap}; b)}{\langle N^2 \rangle_{th}(\theta_{ap}; 1)}}, \quad (26)$$

$$r_{2D}(\theta_{ap}; b, r) = \frac{1}{b_{2D}(\theta_{ap}; b)} \frac{\langle NM_{ap} \rangle_{th}(\theta_{ap}; b, r)}{\langle NM_{ap} \rangle_{th}(\theta_{ap}; 1)}, \quad (27)$$

which can be compared to measurements of the Eqs. (14) and (15).

### 3.3. Intrinsic alignment of sources

Recent studies of cosmic shear find evidence for an alignment of intrinsic source-ellipticities that contribute to the shear-correlation functions (Hildebrandt et al. 2017; Abbott et al. 2016; Troxel & Ishak 2015; Heymans et al. 2013; Joachimi et al. 2011; Mandelbaum et al. 2006). These contributions produce systematic errors in the reconstruction of  $b(k)$  and  $r(k)$  if not included in their normalisation  $f_b$  and  $f_r$ . Relevant are ‘II’-correlations between intrinsic shapes of sources in  $\langle M_{ap}^2 \rangle$  and ‘GI’-correlations between shear and intrinsic shapes in both  $\langle NM_{ap} \rangle$  and  $\langle M_{ap}^2 \rangle$ . The GI term in  $\langle NM_{ap} \rangle$  can be suppressed by minimising the redshift overlap between lenses and sources. Likewise, the II term is suppressed by a broad redshift distribution of sources which, however, increases the GI amplitude. The amplitudes of II and GI also vary with galaxy type and luminosity of the sources (Joachimi et al. 2011).

An intrinsic alignment (IA) of sources has an impact on the ratio statistics  $b_{2D}(\theta_{ap})$  and  $r_{2D}(\theta_{ap})$ , Eqs. (14) and (15), mainly through  $\langle M_{ap}^2 \rangle(\theta_{ap})$  if we separate sources and lenses in redshift. The impact can be mitigated by using an appropriate model for  $\langle M_{ap}^2 \rangle_{th}(\theta_{ap})$  and  $\langle NM_{ap} \rangle_{th}(\theta_{ap})$  in the normalisation of the measurements. For this study, we do not include II or GI correlations in our synthetic mock data but, instead, predict the amplitude of potential systematic errors when ignoring the intrinsic alignment for future applications in Sect. 7.3.

For a reasonable prediction of the GI and II contributions to  $\langle M_{ap}^2 \rangle_{th}(\theta_{ap})$ , we use the recent non-evolution model utilised in Hildebrandt et al. (2017). This model is implemented by using

$$P'_\kappa(\ell) = P_\kappa(\ell) + P_\kappa^{II}(\ell) + P_\kappa^{GI}(\ell) \quad (28)$$

instead of (24) in Eq. (20). The new II and GI terms are given by

$$P_\kappa^{II}(\ell) = \int_0^{\chi_h} \frac{d\chi}{f_K^2(\chi)} \frac{P_s^2(\chi)}{f_K^2(\chi)} F_{ia}^2(\chi) P_m(k_\ell^\chi; \chi); \quad (29)$$

$$P_\kappa^{GI}(\ell) = \frac{3H_0^2 \Omega_m}{c^2} \int_0^{\chi_h} \frac{d\chi}{a(\chi) f_K(\chi)} \frac{P_s(\chi) g_s(\chi)}{f_K(\chi)} F_{ia}(\chi) P_m(k_\ell^\chi; \chi), \quad (30)$$

where

$$F_{ia}(\chi) := -A_{ia} C_1 \bar{\rho}_{crit} \frac{\Omega_m}{D_+(\chi)} \approx -2.4 \times 10^{-2} \left( \frac{A_{ia}}{3.0} \right) \left( \frac{\Omega_m}{0.3} \right) \left( \frac{D_+(\chi)}{0.5} \right)^{-1} \quad (31)$$

controls the correlation amplitude in the so-called ‘non-linear linear’ model; see Hirata & Seljak (2004), Bridle & King (2007), or Joachimi et al. (2011) for details. The factor  $A_{ia}$  scales the amplitude; it broadly falls within  $A_{ia} \in [-3, 3]$  for recent cosmic-shear surveys and is consistent with  $A_{ia} \approx 2$  for sources in the

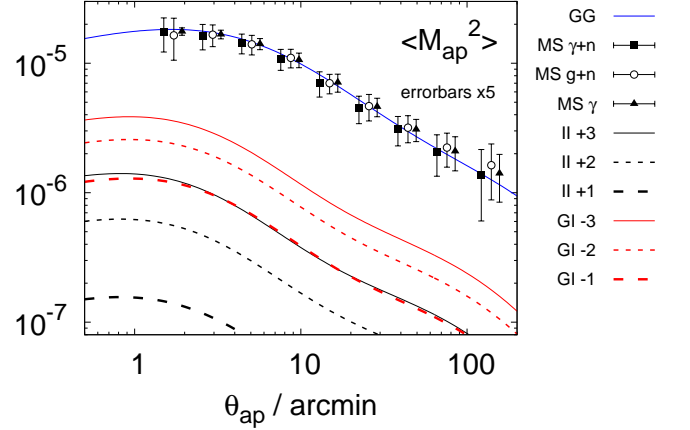


**Fig. 2.** Levels of GI and II contributions to  $\langle M_{ap}^2 \rangle$  for different values of  $A_{ia}$  (red and black lines labelled ‘II  $\pm A_{ia}$ ’ and ‘GI  $\pm A_{ia}$ ’). The line ‘GG’ is the theoretical  $\langle M_{ap}^2 \rangle$  without GI and II terms; the data points are measurements on the mocks for sources with shear and shape noise (MS  $\gamma+n$ ), reduced shear and shape noise (MS  $g+n$ ), and shear without shape noise (MS  $\gamma$ ). The error bars indicate jackknife errors inflated by a factor of five for clarity (Appendix B).

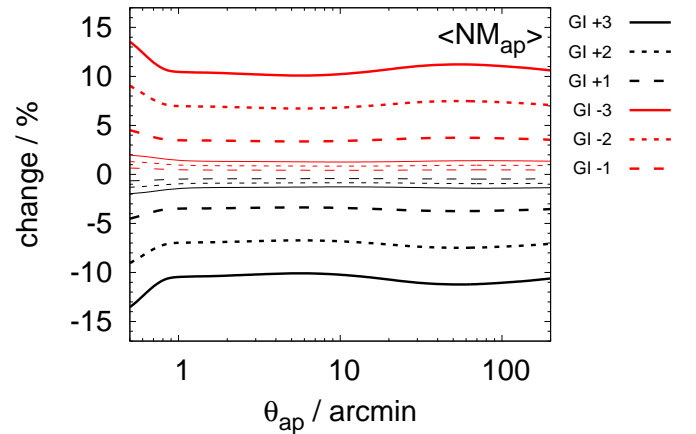


**Fig. 3.** Relative change of  $\langle NM_{ap} \rangle$  for present GI correlations with different amplitudes  $A_{ia}$  as indicated by ‘GI  $\pm A_{ia}$ ’. The figure uses SM4 as fiducial lens-sample; the results for other samples are similar. The thin lines within  $\pm 2\%$  are for the low- $z$  sample, and the thick lines are for the high- $z$  sample.

Kilo-Degree Survey (Joudaki et al. 2017; Hildebrandt et al. 2017; Heymans et al. 2013). For the normalisation of  $F_{ia}(\chi)$ , we use  $C_1 = 5 \times 10^{-14} h^{-2} M_\odot^{-1} \text{Mpc}^3$ , and the linear structure-growth factor  $D_+(\chi)$ , normalised to unity for  $\chi = 0$  (Peebles 1980). By comparing  $P_\kappa^{II}(\ell)$  and  $P_\kappa(\ell)$  in Eq. (22) we see that II contributions are essentially the clustering of sources on the sky (times a small factor). Likewise,  $P_\kappa^{GI}(\ell)$  is essentially the correlation between source positions and their shear on the sky, cf. Eq. (23). In this IA model, we assume a scale-independent galaxy bias for sources in the IA modelling since  $F_{ia}(\chi)$  does not depend on  $k$ .

In Fig. 2, we plot the predicted levels of II and GI terms in the observed  $\langle M_{ap}^2 \rangle$  for varying values of  $A_{ia}$  as black and red



lines for our MS cosmology and the  $p_s(z)$  in our mock survey. The corresponding value of  $A_{ia}$  is shown as number in the figure key. We use negative values of  $A_{ia}$  for GI to produce positive correlations for the plot; the corresponding predictions for  $-A_{ia}$  have the same amplitude as those for  $A_{ia}$  but with opposite sign. II terms, on the other hand, are invariant with respect to a sign flip of  $A_{ia}$ . All curves in the plot use a matter power spectrum  $P_m(k; \chi)$  computed with Halofit (Smith et al. 2003) and the update in Takahashi et al. (2012). For comparison, we plot as blue line GG the theoretical  $\langle M_{ap}^2 \rangle$  without GI and II terms. For  $|A_{ia}| \approx 3$ , GI terms can reach levels up to 10 to 20 per cent of the shear-shear correlation signal for  $\theta_{ap} \gtrsim 1'$ , whereas II terms are typically below 10 per cent. GI and II terms partly cancel each other for  $A_{ia} > 0$  so that the contamination is worse for negative  $A_{ia}$ .

Moreover, we quantify the GI term in  $\langle NM_{ap} \rangle$  by using in (19) the modified power spectrum

$$P'_{nk}(\ell; b, r) = P_{nk}(\ell; b, r) + P_{nk}^{GI}(\ell; b, r) \quad (32)$$

with

$$P_{nk}^{GI}(\ell; b, r) = \int_0^{\chi_h} \frac{d\chi}{f_K^2(\chi)} \frac{p_s(\chi) p_d(\chi)}{f_K^2(\chi)} b(k_\ell^\chi) r(k_\ell^\chi) F_{ia}(\chi) P_m(k_\ell^\chi; \chi). \quad (33)$$

This is the model in Joudaki et al. (2017), see their Equation (11), with an additional term  $r(k_\ell^\chi)$  that accounts for a decorrelation of the lens galaxies. This GI model is essentially the relative clustering between lenses and unbiased sources on the sky and therefore vanishes in the absence of an overlap between the lens and source distributions, which means that  $\int d\chi p_s(\chi) p_d(\chi) = 0$ . In Fig. 3, we quantify the relative change in  $\langle NM_{ap} \rangle$  owing to the GI term for different values of  $A_{ia}$ . Since the change is very similar for all galaxy samples in the same redshift bin, we plot only the results for SM4. The overlap between sources and lenses is only around 4 per cent for low- $z$  samples and, therefore, the change stays within 2 per cent for all angular scales considered here (SES13). On the other hand, for high- $z$  samples where we have roughly 14 per cent overlap between the distributions, the change can amount to almost 10 per cent for  $A_{ia} \approx \pm 2$  and could have a significant impact on the normalisation.

### 3.4. Higher-order corrections

Corrections to the (first-order) Born approximation or for the magnification of the lenses cannot always be neglected as done in Eq. (23) (e.g., Ziour & Hui 2008; Hilbert et al. 2009; Hartlap 2009). This uncorrected equation over-predicts the power spectrum  $P_{nk}(\ell)$  by up to 10% depending on the galaxy selection and the mean redshift of the lens sample; the effect is smaller in a flux-limited survey but also more elaborate to predict as it depends on the luminosity function of the lenses. Hilbert et al. (2009) tests this for the tangential shear around lenses by comparing (23) to the full-ray-tracing results in the MS data which account for contributions from lens-lens couplings and the magnification of the angular number density of lenses.

For a volume-limited lens sample, Hartlap (2009), H09 hereafter, derives the second-order correction (in our notation)

$$P_{nk}^{(2)}(\ell) = -\frac{9H_0^4 \Omega_m^2}{2c^4} \int_0^{\chi_h} d\chi \frac{g_s(\chi) g_d(\chi)}{a^2(\chi)} P_m(k_\ell^\chi; \chi), \quad (34)$$

where

$$g_d(\chi) = \int_\chi^{\chi_h} d\chi' p_d(\chi') \frac{f_K(\chi' - \chi)}{f_K(\chi')}, \quad (35)$$

for a more accurate power spectrum  $P'_{nk}(\ell) = P_{nk}(\ell) + P_{nk}^{(2)}(\ell)$  that correctly describes the correlations in the MS. Physically, this correction accounts for the magnification of the projected number density of lens galaxies by matter in the foreground. We find that the thereby corrected  $\langle NM_{ap} \rangle_{th}(\theta_{ap}; b, r)$  can be different to the uncorrected aperture statistic by up to a few per cent, see left-hand panel in Fig. 4. This directly affects the normalisation of  $r_{2D}(\theta_{ap})$ : the measured, normalised correlation  $r_{2D}(\theta_{ap})$  would be systematically low. We obtain Fig. 4 by comparing the uncorrected to the corrected  $\langle NM_{ap} \rangle_{th}$  for each of our lens-galaxy samples. In accordance with H09, we find that the systematic error is not negligible for some lens sample, and we therefore include this correction by employing  $P'_{nk}(\ell)$  instead of  $P_{nk}(\ell)$  in the normalisation  $f_t(\theta_{ap})$  and in the prediction  $r_{2D}(\theta_{ap}; b, r)$ . This improves the accuracy of the lensing reconstruction of  $r(k)$  by up to a few per cent, most notably the sample blue high- $z$ , especially around  $k \approx 1 h \text{ Mpc}^{-1}$  which corresponds to  $\theta_{ap} \approx 10'$ .

Additional second-order terms for  $P_{nk}(\ell)$  arise due to a flux limit of the survey (Equations 3.129 and 3.130 in H09), but they require a detailed model of the luminosity function for the lenses. We ignore these contributions here because our mock lens samples, selected in redshift bins of  $\Delta z \approx 0.2$  and for stellar masses greater than  $5 \times 10^9 M_\odot$ , are approximately volume limited because of the lower limit of stellar masses and the redshift binning (see Sect. 4.1 in Simon et al. 2017, which use our lens samples).

Similarly, by

$$P_n^{(2)}(\ell; b, r) = \frac{9H_0^4 \Omega_m^2}{c^4} \int_0^{\chi_h} d\chi \frac{g_d^2(\chi)}{a^2(\chi)} P_m(k_\ell^\chi; \chi) - \frac{6H_0^2 \Omega_m}{c^2} \int_0^{\chi_h} d\chi \frac{p_d(\chi) g_d(\chi)}{a(\chi) f_K(\chi)} b(k_\ell^\chi) r(k_\ell^\chi) P_m(k_\ell^\chi; \chi) \quad (36)$$

H09 gives a second-order correction for  $P_n(\ell; b)$  in addition to more corrections for flux-limited surveys (Equations 3.140-3.143). We include  $P_n^{(2)}(\ell; b, r)$  by using  $P'_n(\ell; b, r) = P_n(\ell; b) + P_n^{(2)}(\ell; b, r)$  instead of Eq. (22) in the following for  $f_b(\theta_{ap})$  and  $b_{2D}(\theta_{ap}; b, r)$ , although this correction is typically below half a per cent here; see the right-hand panel in Fig. 4.

## 4. Model templates of biasing functions

Apart from the galaxy-bias normalisation, the ratio statistics  $b_{2D}$  and  $r_{2D}$  are model-free observables of the spatial biasing functions, averaged for the radial distribution of lenses. The deprojection of the ratio statistics into (an average)  $b(k)$  and  $r(k)$  is not straightforward due to the radial and transverse smoothing in the projection. Therefore, for a deprojection we construct a parametric family of templates that we forward-fit to the ratio statistics. In principle, this family could be any generic function but we find that physical templates that can be extrapolated to scales unconstrained by the observations result in a more stable deprojection. To this end, we pick a template prescription that is motivated by the halo-model approach but with more freedom that is commonly devised (Cooray & Sheth 2002, for a review). Notably, we derive explicit expressions for  $b(k)$  and  $r(k)$  in a halo-model framework.

### 4.1. Separation of small and large scales

Before we outline the details of our version of a halo model, used to construct model templates, we point out that any halo model splits the power spectra  $P_m(k)$ ,  $P_{gm}(k)$ , and  $P_g(k)$  into one- and

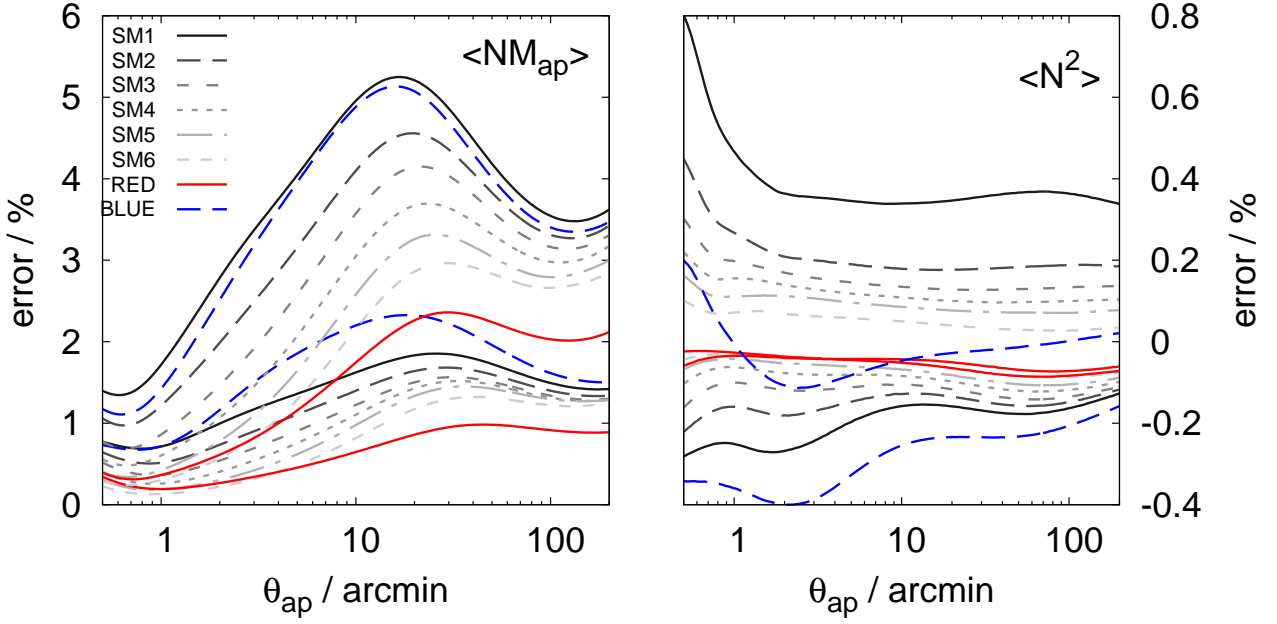


**Fig. 4.** Relative errors in the aperture statistics due to magnification bias of the lenses. *Left:* Errors for  $\langle NM_{\text{ap}} \rangle$  where different line styles distinguish the galaxy samples. Larger errors for the same sample correspond to the high- $z$  bin, smaller errors to low- $z$ . *Right:* Percentage errors for  $\langle N^2 \rangle$  where larger errors for the same line style are the high- $z$  bias.

two halo terms,

$$P(k) = P^{\text{1h}}(k) + P^{\text{2h}}(k). \quad (37)$$

The one-halo term  $P^{\text{1h}}(k)$  dominates at small scales, quantifying the correlations between density fluctuations within the same halo, whereas the two-halo term  $P^{\text{2h}}(k)$  dominates the power spectrum at large scales where correlations between fluctuations in different halos and the clustering of halos become dominant.

We exploit this split to distinguish between galaxy bias on small scales (one-halo terms) and galaxy bias on large scales (two-halo terms), namely

$$b^{\text{1h}}(k) := \sqrt{\frac{P_g^{\text{1h}}(k)}{P_m^{\text{1h}}(k)}}; \quad b^{\text{2h}}(k) := \sqrt{\frac{P_g^{\text{2h}}(k)}{P_m^{\text{2h}}(k)}} \quad (38)$$

and

$$r^{\text{1h}}(k) := \frac{P_{\text{gm}}^{\text{1h}}(k)}{\sqrt{P_g^{\text{1h}}(k) P_m^{\text{1h}}(k)}}; \quad r^{\text{2h}}(k) := \frac{P_{\text{gm}}^{\text{2h}}(k)}{\sqrt{P_g^{\text{2h}}(k) P_m^{\text{2h}}(k)}}, \quad (39)$$

and we derive approximations for both regimes separately. We will find that the two-halo biasing functions are essentially constants, and the one-halo biasing functions are only determined by the relation between matter and galaxy density inside halos.

To patch together both approximations of the biasing functions in the one-halo and two-halo regime, we then do the following. Based on Eq. (10), the function  $b^2(k)$  is a weighted mean of  $b^{\text{1h}}(k)$  and  $b^{\text{2h}}(k)$ :

$$\begin{aligned} b^2(k) &= \frac{P_g^{\text{1h}}(k) + P_g^{\text{2h}}(k)}{P_m(k)} \\ &= \frac{P_m^{\text{1h}}(k) [b^{\text{1h}}(k)]^2}{P_m(k)} + \frac{P_m^{\text{2h}}(k) [b^{\text{2h}}(k)]^2}{P_m(k)} \\ &= (1 - W_m(k)) [b^{\text{1h}}(k)]^2 + W_m(k) [b^{\text{2h}}(k)]^2, \end{aligned} \quad (40)$$

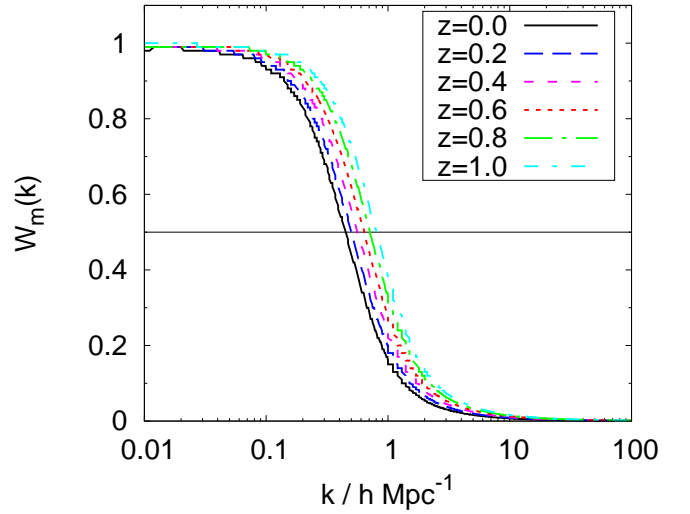


**Fig. 5.** The weight  $W_m(k)$  of the two-halo term in the matter-power spectrum for varying redshifts  $z$ .

where the weight

$$W_m(k) := \frac{P_m^{\text{2h}}(k)}{P_m(k)} \quad (41)$$

is the amplitude of the two-halo matter power spectrum relative to the total matter power spectrum. Deep in the one-halo regime we have  $W_m(k) \approx 0$  but  $W_m(k) \approx 1$  in the two-halo regime. Since the two-halo biasing is approximately constant, the scale-dependence of galaxy bias is mainly a result of the galaxy physics inside halos and the shape of  $W_m(k)$ .

Once the weight  $W_m(k)$  is determined for a fiducial cosmology, it does not rely on galaxy physics, we can use it for any



model of  $b^{1h}(k)$  and  $b^{2h}(k)$ . In principle, the weight  $W_m(k)$  could be accurately measured from a cosmological simulation by correlating only the matter density from different halos for  $P_m^{2h}(k)$  which is then normalised by the full power spectrum  $P_m(k)$  in the simulation. We, however, determine  $W_m(k)$  by computing the one-halo and two-halo term of  $P_m(k)$  with the setup of Simon et al. (2009). Our results for  $W_m(k)$  at different redshifts are plotted in Fig. 5. There we find that the transition between the one-halo and two-halo regime,  $W_m \sim 0.5$ , is at  $k \sim 0.3 h \text{ Mpc}^{-1}$  for  $z = 0$ , whereas the transition point moves to  $k \sim 1 h \text{ Mpc}^{-1}$  for  $z \sim 1$ .

Similar to  $b(k)$ , we can expand the correlation function  $r(k)$  in terms of its one-halo and two-halo biasing functions. To this end, let

$$W_g(k) := \frac{P_g^{2h}(k)}{P_g(k)} = \left( \frac{b^{2h}(k)}{b(k)} \right)^2 W_m(k) \quad (42)$$

be a weight by analogy to  $W_m(k)$ . For unbiased galaxies, that is  $b^{2h}(k) = b(k) = 1$ , we simply have  $W_g(k) = W_m(k)$ . Using the definition of  $r(k)$  in Eq. (10) and Eq. (39), we generally find

$$r(k) = \sqrt{(1 - W_m(k))(1 - W_g(k))} r^{1h}(k) + \sqrt{W_m(k)W_g(k)} r^{2h}(k). \quad (43)$$

#### 4.2. Halo-model definitions

For approximations of the biasing functions in the one- and two-halo regime, we apply the formalism in Seljak (2000) and briefly summarise it here. All halo-related quantities depend on redshift. In the fits with the model later on, we use for this the mean redshift of the lens galaxies.

We shall denote by  $n(m) dm$  the (comoving) number density of halos within the halo-mass range  $[m, m + dm]$ ;  $\langle N|m \rangle$  is the mean number of galaxies inside a halo of mass  $m$ ;  $\langle N(N-1)|m \rangle$  is the mean number of galaxy pairs inside a halo of mass  $m$ . Let  $u(r, m)$  be the radial profile of the matter density inside a halo or the galaxy density-profile. Also let

$$\tilde{u}(k, m) = \frac{\int_0^\infty ds s k^{-1} u(s, m) \sin(ks)}{\int_0^\infty ds s^2 u(s, m)} \quad (44)$$

be its normalised Fourier transform. Owing to this normalisation, profiles obey  $\tilde{u}(k, m) = 1$  at  $k = 0$ . To assert a well-defined normalisation of halos, we truncate them at their virial radius  $r_{\text{vir}}$ , which we define by the over-density  $\Omega_m \bar{\rho}_{\text{crit}} \Delta_{\text{vir}}(z)$  within the distance  $r_{\text{vir}}$  from the halo centre and by  $\Delta_{\text{vir}}(z)$  as in Bullock et al. (2001). Furthermore, the mean matter and galaxy number density (comoving) are

$$\bar{\rho}_m = \int dm n(m) m; \quad \bar{n}_g = \int dm n(m) \langle N|m \rangle. \quad (45)$$

The one-halo terms of the galaxy power spectrum  $P_g(k)$ , the matter power-spectrum  $P_m(k)$ , and the galaxy-matter cross-power spectrum  $P_{gm}(k)$  are

$$P_g^{1h}(k) = \int_0^\infty \frac{dm n(m)}{\bar{n}_g^2} \tilde{u}_g^{2p}(k, m) \langle N(N-1)|m \rangle; \quad (46)$$

$$P_m^{1h}(k) = \int_0^\infty \frac{dm n(m) m^2}{\bar{\rho}_m^2} \tilde{u}_m^2(k, m); \quad (47)$$

$$P_{gm}^{1h}(k) = \int_0^\infty \frac{dm n(m) m}{\bar{\rho}_m \bar{n}_g} \tilde{u}_m(k, m) \tilde{u}_g^q(k, m) \langle N|m \rangle. \quad (48)$$

In these equations, the exponents  $p$  and  $q$  are modifiers of the statistics for central galaxies which are accounted for in the following simplistic way: Central galaxies are by definition at the halo centre  $r = 0$ ; one galaxy inside a halo is always a central galaxy; their impact on galaxy power spectra is assumed to be only significant for halos that contain few galaxies. Depending on whether a halo contains few galaxies or not, the factors  $(p, q)$  switch on or off a statistics dominated by central galaxies through

$$\begin{aligned} p &= \begin{cases} 1 & , \text{ for } \langle N(N-1)|m \rangle > 1 \\ 1/2 & , \text{ otherwise} \end{cases}; \\ q &= \begin{cases} 1 & , \text{ for } \langle N|m \rangle > 1 \\ 0 & , \text{ otherwise} \end{cases}. \end{aligned} \quad (49)$$

We note that  $p$  and  $q$  are functions of the halo mass  $m$ . Later in Sect. 4.6, we consider also more general models where there can be a fraction of halos that contains only satellite galaxies. We achieve this by mixing (46)–(48) with power spectra in a pure-satellite scenario, this means a scenario where always  $p \equiv q \equiv 1$ .

We now turn to the two-halo terms in this halo model. We approximate the clustering power of centres of halos with mass  $m$  by  $b_h^2(m) P_{\text{lin}}(k)$ , where  $P_{\text{lin}}(k)$  denotes the linear matter power spectrum, and  $b_h(m)$  is the halo bias-factor on linear scales; the clustering of halos is thus linear and deterministic in this description. Likewise, this model approximates the cross-correlation power-spectrum of halos with the masses  $m_1$  and  $m_2$  by  $b_h(m_1) b_h(m_2) P_{\text{lin}}(k)$ . The resulting two-halo terms are then

$$P_g^{2h}(k) = \frac{P_{\text{lin}}(k)}{\bar{n}_g^2} \left( \int_0^\infty dm n(m) \langle N|m \rangle b_h(m) \tilde{u}_g(k, m) \right)^2; \quad (50)$$

$$P_m^{2h}(k) = \frac{P_{\text{lin}}(k)}{\bar{\rho}_m^2} \left( \int_0^\infty dm n(m) m b_h(m) \tilde{u}_m(k, m) \right)^2; \quad (51)$$

$$\begin{aligned} P_{gm}^{2h}(k) &= \frac{P_{\text{lin}}(k)}{\bar{n}_g \bar{\rho}_m} \int_0^\infty dm n(m) \langle N|m \rangle b_h(m) \tilde{u}_g(k, m) \\ &\quad \times \int_0^\infty dm n(m) m b_h(m) \tilde{u}_m(k, m). \end{aligned} \quad (52)$$

The two-halo terms ignore power from central galaxies because it is negligible in the two-halo regime.

#### 4.3. A toy model for the small-scale galaxy bias

We first consider an insightful toy model of  $b(k)$  and  $r(k)$  at small scales. In this model, both the matter and the galaxy distribution shall be completely dominated by halos of mass  $m_0$ , such that we find an effective halo-mass function  $n(m) \propto \delta_D(m - m_0)$ ; its normalisation is irrelevant for the galaxy bias. In addition, the halos of the toy model shall not cluster so that the two-halo terms of the power spectra vanish entirely. The toy model has practical relevance in what follows later because the one-halo biasing functions that we derive afterwards are weighted averages of toy models with different  $m_0$ . For this reason, most of the features can already be understood here, albeit not all, and it already elucidates biasing functions on small scales.

Let us define the variance  $\sigma_N^2(m_0) = \langle N^2|m_0 \rangle - \langle N|m_0 \rangle^2$  of the halo-occupation distribution (HOD) in excess of a Poisson variance  $\langle N|m_0 \rangle$  by

$$\Delta\sigma_N^2(m_0) = \sigma_N^2(m_0) - \langle N|m_0 \rangle. \quad (53)$$

If the model galaxies obey Poisson statistic they have  $\Delta\sigma_N^2(m_0) = 0$ . We can now write the mean number of galaxy

pairs as

$$\begin{aligned} \langle N(N-1)|m_0 \rangle &= \langle N^2|m_0 \rangle - \langle N|m_0 \rangle \\ &= \langle N|m_0 \rangle^2 \left( 1 + \frac{\Delta\sigma_N^2(m_0)}{\langle N|m_0 \rangle^2} \right). \end{aligned} \quad (54)$$

By using the Eqs. (46)–(48) with  $n(m) \propto \delta_D(m - m_0)$ , the correlation factor reads

$$\begin{aligned} R(k, m_0) &= \\ \frac{\tilde{u}_g^{q-p}(k, m_0) \langle N|m_0 \rangle}{\sqrt{\langle N(N-1)|m_0 \rangle}} &= \tilde{u}_g^{q-p}(k, m_0) \left( 1 + \frac{\Delta\sigma_N^2(m_0)}{\langle N|m_0 \rangle^2} \right)^{-1/2}, \end{aligned} \quad (55)$$

and the bias factor is

$$\begin{aligned} B(k, m_0) &= \\ \frac{\tilde{u}_g^p(k, m_0) \sqrt{\langle N(N-1)|m_0 \rangle}}{\tilde{u}_m(k, m_0) \langle N|m_0 \rangle} &= \frac{\tilde{u}_g^q(k, m_0)}{\tilde{u}_m(k, m_0)} \frac{1}{R(k, m_0)}. \end{aligned} \quad (56)$$

To avoid ambiguities in the following, we use capital letters for the biasing functions in the toy model.

We dub galaxies ‘faithful tracers’ of the matter density if they have both (i)  $\tilde{u}_g(k, m) = \tilde{u}_m(k, m)$  and (ii) no central galaxies ( $p = q = 1$ ). Halos with relatively small numbers of galaxies, that is  $\langle N|m_0 \rangle, \langle N(N-1)|m_0 \rangle \lesssim 1$ , are called ‘low-occupancy halos’ in the following. This toy model then illustrates the following points.

- Owing to galaxy discreteness, faithful tracers are biased if they not obey Poisson statistics. Namely, for a sub-Poisson variance,  $\Delta\sigma_N^2(m_0) < 0$ , they produce opposite trends  $R(k, m_0) > 1$  and  $B(k, m_0) < 1$  with  $k$ , and vice versa for a super-Poisson sampling, but generally we find the relation  $R(k, m_0) \times B(k, m_0) = 1$ .
- Nevertheless faithful tracers obey  $B(k, m_0), R(k, m_0) \approx 1$  if the excess variance becomes negligible, that is if  $\Delta\sigma_N^2(m_0) \ll \langle N|m_0 \rangle^2$ . The discreteness of galaxies therefore becomes only relevant in low-occupancy halos.
- A value of  $R(k, m_0) > 1$  occurs once central galaxies are present ( $p, q < 1$ ). As a central galaxy is *always* placed at the centre, central galaxies produce a non-Poisson sampling of the profile  $u_m(r, m_0)$ . In contrast to faithful galaxies with a non-Poisson HOD, we then find agreeing trends with scale  $k$  for  $R(k, m_0)$  and  $B(k, m_0)$  if  $\Delta\sigma_N^2(m_0) = 0$ . Again, this effect is strong only in low-occupancy halos.
- The biasing functions in the toy model are only scale-dependent if galaxies are not faithful tracers. The bias function  $B(k, m_0)$  varies with  $k$  if either  $\tilde{u}_m(k, m_0) \neq \tilde{u}_g(k, m_0)$  or for central galaxies ( $p \neq 1$ ). The correlation function  $R(k, m_0)$  is scale-dependent only for central galaxies, that is  $p - q \neq 0$ , which then obeys  $R(k, m_0) \propto \tilde{u}_g^{-1/2}(k, m_0)$ . Variations with  $k$  become small for both functions, however, if  $\tilde{u}_m(k, m_0), \tilde{u}_g(k, m_0) \approx 1$ , which is on scales larger than the size  $r_{\text{vir}}$  of a halo.

We stress again that a counter-intuitive  $r(k) > 1$  is a result of the definition of  $P_g(k)$  relative to Poisson shot-noise and the actual presence of non-Poisson galaxy noise. One may wonder here if  $r > 1$  is also allowed for biasing parameters defined in terms of spatial correlations rather than the power spectra. That this is indeed the case is shown in Appendix A for completeness.

#### 4.4. Galaxy biasing at small scales

Compared to the foregoing toy model, no single halo mass scale dominates the galaxy bias at any wave number  $k$  for realistic galaxies. Nevertheless, we can express the realistic biasing functions  $b^{\text{lh}}(k)$  and  $r^{\text{lh}}(k)$  in the one-halo regime as weighted averages of the toy model  $B(k, m)$  and  $R(k, m)$  with modifications.

To this end, we introduce by

$$b(m) = \frac{\langle N|m \rangle \bar{\rho}_m}{m \bar{n}_g} \quad (57)$$

the ‘mean biasing function’ which is the mean number of halo galaxies  $\langle N|m \rangle$  per halo mass  $m$  in units of the cosmic average  $\bar{n}_g/\bar{\rho}_m$  (Cacciato et al. 2012). If galaxy numbers linearly scale with halo mass, that means  $\langle N|m \rangle \propto m$ , we find a mean biasing function of  $b(m) = 1$  while halos masses devoid of galaxies have  $b(m) = 0$ . For convenience, we make use of  $\langle N|m \rangle \propto m b(m)$  instead of  $\langle N|m \rangle$  in the following equations because we typically find  $\langle N|m \rangle \propto m^\beta$  with  $\beta \approx 1$ :  $b(m)$  is therefore usually not too different from unity.

Using the Eqs. (46) and (47) we then find

$$[b^{\text{lh}}(k)]^2 = \frac{P_g^{\text{lh}}(k)}{P_m^{\text{lh}}(k)} = \int_0^\infty dm w_{20}^{\text{lh}}(k, m) b^2(m) B^2(k, m) \quad (58)$$

with  $w_{20}^{\text{lh}}(k, m)$  being one case in a family of (one-halo) weights,

$$w_{ij}^{\text{lh}}(k, m) := \frac{n(m) m^2 \tilde{u}_m^i(k, m) [b(m) \tilde{u}_g(k, m)]^j}{\int_0^\infty dm n(m) m^2 \tilde{u}_m^i(k, m) [b(m) \tilde{u}_g(k, m)]^j}. \quad (59)$$

This family and the following weights  $w(k, m)$  are normalised, which means that  $\int dm w(k, m) = 1$ . The introduction of these weight functions underlines that the biasing functions are essentially weighted averages across the halo-mass spectrum as, for example,  $[b^{\text{lh}}(k)]^2$  which is the weighted average of  $b^2(m) B^2(k, m)$ .

The effect of  $w_{20}^{\text{lh}}(k, m)$  is to down-weight large halo masses in the bias function because  $w_{20}^{\text{lh}}(k, m_1)/w_{20}^{\text{lh}}(k, m_2) \propto \tilde{u}_m^2(k, m_1)/\tilde{u}_m^2(k, m_2)$  decreases with  $m_1$  for a fixed  $m_2 < m_1$  and  $k$ . Additionally, the relative weight of a halo with mass  $m$  decreases towards larger  $k$  because  $\tilde{u}_m(k, m)$  tends to decrease with  $k$ . As a result, at a given scale  $k$  only halos below a typical mass essentially contribute to the biasing functions (Seljak 2000).

We move on to the correlation factor  $r^{\text{lh}}(k)$  in the one-halo regime. Using the Eqs. (46)–(48) and the relations

$$\langle N(N-1)|m \rangle = R^{-2}(k, m) \tilde{u}_g^{2q-2p}(k, m) \langle N|m \rangle; \quad (60)$$

$$\tilde{\rho}_m(k, m) = m \tilde{u}_m(k, m); \quad (61)$$

$$\tilde{\rho}_g(k, m) = \langle N|m \rangle \tilde{u}_g(k, m) \quad (62)$$

we write

$$r^{\text{lh}}(k) = \frac{P_{\text{gm}}^{\text{lh}}(k)}{\sqrt{P_g^{\text{lh}}(k) P_m^{\text{lh}}(k)}} =: \zeta_{\text{sat}}(k) \zeta_{\text{cen}}(k) \zeta_{\Delta\sigma}(k) \quad (63)$$

as product of the three separate factors

$$\zeta_{\text{sat}}(k) := \frac{\int_0^\infty dm n(m) \tilde{\rho}_m(k, m) \tilde{\rho}_g(k, m)}{\left( \int_0^\infty dm n(m) \tilde{\rho}_g^2(k, m) \int_0^\infty dm n(m) \tilde{\rho}_m^2(k, m) \right)^{1/2}}; \quad (64)$$

$$\zeta_{\text{cen}}(k) := \int_0^\infty dm w_{11}^{\text{lh}}(k, m) \tilde{u}_g^{q-1}(k, m); \quad (65)$$

$$\zeta_{\Delta\sigma}(k) := \left( \int_0^\infty dm w_{02}^{\text{lh}}(k, m) \tilde{u}_g^{2q-2}(k, m) R^{-2}(k, m) \right)^{-1/2} \quad (66)$$

with the following meaning.

- The first factor  $\zeta_{\text{sat}}(k)$  quantifies, at spatial scale  $k$ , the correlation between the radial profiles of the matter density  $\bar{\rho}_m(k, m)$  and the (average) number density of satellite galaxies  $\bar{\rho}_g(k, m)$  across the halo mass-spectrum  $n(m)$ . As upper bound we always have  $|\zeta_{\text{sat}}(k)| \leq 1$  because of the Cauchy-Schwarz inequality when applied to the nominator of Eq. (64). Thus  $\zeta_{\text{sat}}(k)$  probably reflects best what we intuitively understand by a correlation factor between galaxies and matter densities inside a halo. Since it only involves the average satellite profile, the satellite shot-noise owing to a HOD variance is irrelevant at this point. The next two factors can be seen as corrections to  $\zeta_{\text{sat}}(k)$  owing to central galaxies or a non-Poisson HOD variance.
- The second factor  $\zeta_{\text{cen}}(k)$  is only relevant in the sense of  $\zeta_{\text{cen}}(k) \neq 1$  through low-occupancy halos with central galaxies ( $q \neq 1$ ). It has the lower limit  $\zeta_{\text{cen}}(k) \geq 1$  because of  $\tilde{u}_g(k, m) \leq 1$  and hence  $\tilde{u}_g^{q-1}(k, m) \geq 1$ . This correction factor can therefore at most increase the correlation  $r^{\text{lh}}(k)$ .
- The third factor  $\zeta_{\Delta\sigma}(k)$  is the only one that is sensitive to an excess variance  $\Delta\sigma_N^2(m) \neq 0$  of the HOD, namely through  $R(k, m)$ . In the absence of central galaxies, that means for  $p \equiv q \equiv 1$ ,  $\zeta_{\Delta\sigma}^2(k)$  is the (weighted) harmonic mean of  $R^2(k, m)$ , or the harmonic mean of the reduced  $[\tilde{u}_g(k, m) R(k, m)]^2 \leq R^2(k, m)$  otherwise.

As sanity check, we note the recovery of the toy model by setting  $n(m) \propto \delta_D(m - m_0)$  in (58) and (63). In contrast to the toy model, the templates  $b^{\text{lh}}(k)$  and  $r^{\text{lh}}(k)$  can be scale-dependent even if  $B(k, m)$  and  $R(k, m)$  are constants. This scale dependence can be produced by a varying  $w_{20}^{\text{lh}}(k, m)$  or  $\zeta_{\text{sat}}(k)$ .

#### 4.5. Galaxy biasing at large scales

From the two-halo terms (50)–(52), we can immediately derive the two-halo biasing functions. The bias factor is

$$b^{2h}(k) = \sqrt{\frac{P_g^{2h}(k)}{P_m^{2h}(k)}} = \frac{\int_0^\infty dm w_{10}^{2h}(m) b_h(m) \tilde{u}_g(k, m)}{\int_0^\infty dm w_{01}^{2h}(m) b_h(m) \tilde{u}_m(k, m)}, \quad (67)$$

where we have introduced into the integrals the normalised (two-halo) weights

$$w_{ij}^{2h}(m) := \frac{n(m) [m b(m)]^i m^j}{\int_0^\infty dm n(m) [m b(m)]^i m^j}. \quad (68)$$

We additionally approximate  $\tilde{u}(k, m) \approx 1$  for the two-halo regime. This is a reasonable approximation because virialised structures are typically not larger than  $\sim 10 h^{-1} \text{ Mpc}$  and hence exhibit  $\tilde{u}(k, m) \approx 1$  for  $k \ll 0.5 h \text{ Mpc}^{-1}$ . Therefore, we find an essentially constant bias function at large scales,

$$b^{2h}(k) \approx \int_0^\infty dm w_{10}^{2h}(m) b_h(m) =: b_{\text{ls}}. \quad (69)$$

We have used here  $\int dm w_{01}^{2h}(m) b_h(m) = 1$  which follows from the constraint  $P_m(k) \rightarrow P_{\text{lin}}(k)$  for  $k \rightarrow 0$  and the Eq. (51). To have more template flexibility, we leave  $b_{\text{ls}}$  as free parameter and devise the Eq. (69) only if no large-scale information is available by observations.

The two-halo correlation-function at large scales is exactly

$$r^{2h}(k) = \frac{P_{\text{gm}}^{2h}(k)}{\sqrt{P_g^{2h}(k) P_m^{2h}(k)}} = 1 = r_{\text{ls}} \quad (70)$$

due to  $P_h(k; m_1, m_2) = b_h(m_1) b_h(m_2) P_m(k)$  for the assumed halo clustering. Evidently, the large-scale matter-galaxy correlation is fixed to  $r_{\text{ls}} = 1$ . The correlation is necessarily high because the model galaxies are always inside halos so that galaxies closely follow the matter distribution at large scales.

We note that  $r_{\text{ls}} \neq 1$  is physically conceivable although it is usually excluded in halo models (Tegmark & Peebles 1998). To test for an actually high correlation  $r_{\text{ls}} = 1$  in real data, we may use  $r_{\text{ls}}$  as free parameter in the templates.

#### 4.6. Fraction of central galaxies

Up to here, we assumed either one central galaxy for every halo that hosts galaxies or pure samples of satellite galaxies, meaning  $p \equiv q \equiv 1$ . In reality where we select sub-populations of galaxies, not every sub-sample automatically provides a central galaxy in every halo; a central galaxy could belong to another galaxy population, for instance. For more template flexibility, we thus assume that only a fraction  $f_{\text{cen}}$  of halos can have central galaxies from the selected galaxy population; the other fraction  $1 - f_{\text{cen}}$  of halos has either only satellites or central galaxies from another population. Both halo fractions nevertheless shall contain  $\langle N|m \rangle$  halo galaxies on average. Importantly,  $f_{\text{cen}}$  shall be independent of halo mass. This is not a strong restriction because the impact of central galaxies becomes only relevant for low-occupancy halos whose mass scale  $m$  is confined by  $\langle N|m \rangle \lesssim 1$  anyway.

The extra freedom of  $f_{\text{cen}} \neq 1$  in the templates modifies the foregoing power spectra. On the one hand, the two-halo power spectra are unaffected because they do not depend on either  $p$  or  $q$ . On the other hand for the one-halo regime, we now find the linear combination

$$P_g^{\text{lh}}(k) = f_{\text{cen}} P_g^{\text{cen}}(k) + (1 - f_{\text{cen}}) P_g^{\text{sat}}(k), \quad (71)$$

$$P_{\text{gm}}^{\text{lh}}(k) = f_{\text{cen}} P_{\text{gm}}^{\text{cen}}(k) + (1 - f_{\text{cen}}) P_{\text{gm}}^{\text{sat}}(k) \quad (72)$$

because halos with (or without) central galaxies contribute with probability  $f_{\text{cen}}$  (or  $1 - f_{\text{cen}}$ ) to the one-halo term. In the equations, the  $P^{\text{cen}}(k)$  denote the one-halo power spectra of halos with central galaxies, and the  $P^{\text{sat}}(k)$  denote spectra of halos with only satellites. Both cases are covered in the foregoing formalism for appropriate values of  $p, q$ : Satellite-only halos with superscript ‘sat’ are obtained by using  $p \equiv q \equiv 1$ ; halos with central galaxies, superscript ‘cen’, use the usual mass-dependent expressions (49).

As result, we can determine the bias factor for the mixture scenario with (71) by

$$[b^{\text{lh}}(k)]^2 = f_{\text{cen}} [b_{\text{cen}}(k)]^2 + (1 - f_{\text{cen}}) [b_{\text{sat}}(k)]^2. \quad (73)$$

Here  $b_{\text{cen}}(k)$  denotes Eq. (58) in the central-galaxy scenario, whereas  $b_{\text{sat}}(k)$  denotes the satellite-only scenario of this equation. Similarly for the correlation,  $r^{\text{lh}}(k)$  we obtain with (71) and (72)

$$\begin{aligned} r^{\text{lh}}(k) &= \\ f_{\text{cen}} \frac{P_{\text{gm}}^{\text{cen}}(k)}{\sqrt{P_g^{\text{lh}}(k) P_m^{\text{lh}}(k)}} &+ (1 - f_{\text{cen}}) \frac{P_{\text{gm}}^{\text{sat}}(k)}{\sqrt{P_g^{\text{lh}}(k) P_m^{\text{lh}}(k)}} \\ &= f_{\text{cen}} \sqrt{\frac{P_g^{\text{cen}}(k)}{P_g^{\text{lh}}(k)}} r_{\text{cen}}(k) + (1 - f_{\text{cen}}) \sqrt{\frac{P_g^{\text{sat}}(k)}{P_g^{\text{lh}}(k)}} r_{\text{sat}}(k) \\ &= \frac{f_{\text{cen}} r_{\text{cen}}(k)}{\sqrt{f_{\text{cen}} + (1 - f_{\text{cen}}) \left(\frac{b_{\text{sat}}(k)}{b_{\text{cen}}(k)}\right)^2}} + \frac{(1 - f_{\text{cen}}) r_{\text{sat}}(k)}{\sqrt{1 - f_{\text{cen}} + f_{\text{cen}} \left(\frac{b_{\text{cen}}(k)}{b_{\text{sat}}(k)}\right)^2}}, \end{aligned} \quad (74)$$

because

$$P_g^{\text{lh}}(k) = f_{\text{cen}} [b_{\text{cen}}(k)]^2 P_m^{\text{lh}}(k) + (1 - f_{\text{cen}}) [b_{\text{sat}}(k)]^2 P_m^{\text{lh}}(k). \quad (75)$$

The function  $r_{\text{cen}}(k)$  denotes Eq. (63) in the central-galaxy scenario, and  $r_{\text{sat}}(k)$  is the satellite-only scenario.

## 5. Parameters of model templates and physical discussion

In this section, we summarise the concrete implementation of our templates, and we discuss their parameter dependence for a physical discussion on the scale-dependent galaxy bias.

### 5.1. Normalised excess-variance

For a practical implementation of our templates, we find it useful to replace  $\Delta\sigma_N^2(m)$  in Eq. (53) by the ‘normalised excess-variance’

$$V(m) = \frac{\Delta\sigma_N^2(m)}{\langle N|m \rangle} = \frac{\sigma_N^2(m)}{\langle N|m \rangle} - 1, \quad (76)$$

which typically has a small dynamic range with values between minus and plus unity. To see this, we discuss its upper and lower limits in the following.

First, the normalised excess-variance has a lower limit because the average number of galaxy pairs is always positive,

$$\langle N(N-1)|m \rangle = \langle N|m \rangle^2 \left( 1 + \frac{V(m)}{\langle N|m \rangle} \right) \geq 0, \quad (77)$$

which imposes  $V(m) \geq -\langle N|m \rangle$ . As additional constraint we have a positive variance

$$\sigma_N^2(m) = \langle N|m \rangle (V(m) + 1) \geq 0 \quad (78)$$

or  $V(m) \geq -1$  so that we use

$$V(m) \geq \max \left\{ -1, -\langle N|m \rangle \right\} \quad (79)$$

for a valid set of template parameters.

Second for the upper limit of  $V(m)$ , we imagine that there is a maximum  $N_{\text{max}}(m)$  for the amount of halo galaxies (of the selected population) inside a halo of mass  $m$ . A maximum  $N_{\text{max}}(m)$  makes physically sense because we cannot squeeze an arbitrary number of galaxies into a halo. Nevertheless, their amount  $0 \leq N(m) \leq N_{\text{max}}(m)$  shall be random with PDF  $P(N|m)$ . Of this PDF we already know that its mean is  $\langle N|m \rangle$ . For its the maximum possible variance  $\sigma_{\text{max}}^2(m)$ , we note that  $\sigma_N^2(m)$  cannot be larger than that for halos with a bimodal distribution of only two allowed galaxy numbers  $N(m) \in \{0, N_{\text{max}}(m)\}$  that shall occur with probability  $1 - \lambda$  and  $\lambda$ , respectively. The mean of this bimodal PDF is  $\langle N|m \rangle = \lambda N_{\text{max}}(m)$ , and its variance  $\sigma_{\text{max}}^2(m) = \langle N^2|m \rangle - \langle N|m \rangle^2$  consequently satisfies

$$\sigma_{\text{max}}(m) = \sqrt{N_{\text{max}}^2(m) \lambda - N_{\text{max}}^2(m) \lambda^2} = \langle N|m \rangle^{1/2} \sqrt{N_{\text{max}}(m) - \langle N|m \rangle}, \quad (80)$$

which is the upper limit for any  $P(N|m)$ . Together with the lower bound of  $V(m)$ , we thus arrive at

$$\max \left\{ -1, -\langle N|m \rangle \right\} \leq V(m) \leq N_{\text{max}}(m) - 1 - \langle N|m \rangle. \quad (81)$$

**Table 2.** List of free template parameters

Param	Description	Dim
$b_{\text{ls}}$	large-scale bias factor	1
$r_{\text{ls}}$	large-scale correlation factor	(1)
$b(m)$	mean biasing function (interp.)	22
$V(m)$	normalised excess-variance (interp.)	22
$m_{\text{piv}}$	$\langle N m_{\text{piv}} \rangle = 1$ ; pivotal halo mass	1
$f_{\text{cen}}$	halo fraction open for central galaxies	1

$$\Sigma = 47 \quad (48)$$

**Notes.** The parameters  $b(m)$  and  $V(m)$  cover the mass range  $10^4 - 10^{16} h^{-1} M_{\odot}$ . The numbers “(1)” in brackets indicate optional degrees of freedom of the template. See text for more details.

This means: halos that are (on average) filled close to the limit, that is  $\langle N|m \rangle \approx N_{\text{max}}(m) \geq 1$ , have a HOD variance that is sub-Poisson, close to  $V(m) = -1$ . This should be especially the case for halos with  $\langle N|m \rangle \approx 1$ . On the other hand, halos with  $N_{\text{max}}(m) \approx 1$  and low occupancy,  $\langle N|m \rangle \ll 1$ , necessarily obey Poisson statistics or are close to that, which means that  $V(m) \approx 0$ . On the other extreme end, spacious halos well below the fill limit,  $N_{\text{max}}(m) \gg 1$  and  $N_{\text{max}}(m) \gg \langle N|m \rangle$ , have sufficient headroom to allow for a super-Poisson variance which means that  $V(m) > 0$ . In the following, we adopt the upper limit  $V(m) \leq +1$  meaning that we a-priori do not allow the HOD variance to become larger than twice the Poisson variance.

### 5.2. Implementation

Generally the functions  $V(m)$  and  $b(m)$  are continuous functions of the halo mass  $m$ . We apply, however, an interpolation with 20 interpolation points on a equidistant logarithmic  $m$ -scale for these functions, spanning the range  $10^8 h^{-1} M_{\odot}$  to  $10^{16} h^{-1} M_{\odot}$ ; between adjacent sampling points we interpolate linearly on the log-scale; we set  $b(m) = V(m) = 0$  outside the interpolation range. Additionally, we find in numerical experiments with unbiased galaxies that the halo mass-scale has to be lowered to  $10^4 h^{-1} M_{\odot}$  to obtain correct descriptions of the bias. We therefore include two more interpolation points at  $10^4$  and  $10^6 h^{-1} M_{\odot}$  to extend the mass scale to very low halo masses. For the large-scale bias, we set  $r_{\text{ls}} \equiv 1$  but leave  $b_{\text{ls}}$  as free parameter.

To predict the number density  $\bar{n}_g$  of galaxies, Eq. (45), and to determine  $(p, q)$  for a given mass  $m$  we have to obtain  $\langle N|m \rangle$  from  $b(m)$ . For this purpose, we introduce another parameter  $m_{\text{piv}}$  which is the pivotal mass of low-occupancy halos, defined by  $\langle N|m_{\text{piv}} \rangle = 1$  such that

$$\langle N|m \rangle = \frac{m}{m_{\text{piv}}} \frac{b(m)}{b(m_{\text{piv}})}. \quad (82)$$

The (comoving) number density of galaxies  $\bar{n}_g$  is then given by

$$\frac{\bar{n}_g}{\bar{\rho}_m} = \frac{\int_0^\infty dm n(m) \langle N|m \rangle}{\bar{\rho}_m} = \int_0^\infty \frac{dm w_{01}^{2h}(m)}{m_{\text{piv}}} \frac{b(m)}{b(m_{\text{piv}})}, \quad (83)$$

for which we use  $\bar{\rho}_m = \Omega_m \bar{\rho}_{\text{crit}}$ . With this parameterisation, the normalisation of  $b(m)$  is irrelevant in all equations of our bias

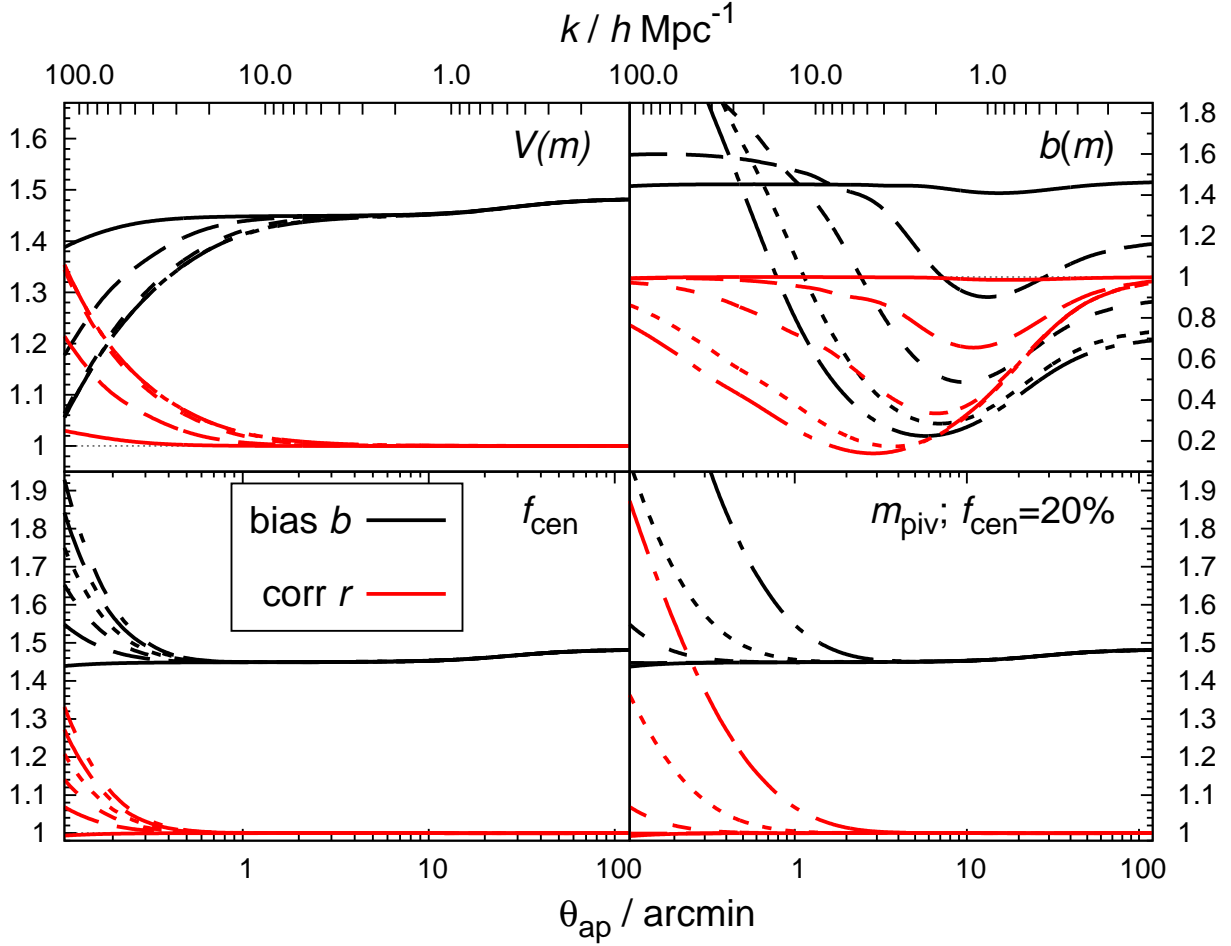


**Fig. 6.** Family of templates  $b(k)$  (black lines) and  $r(k)$  (red lines) for the range of wave numbers  $k$  in the top axis; the left-hand y-axis applies to the panels in the first column, the right-hand axis to the second column. The aperture scale  $\theta_{\text{ap}} = 4.25/(k f_K(z_d))$  (bottom axis) crudely traces the projected  $b_{2D}(\theta_{\text{ap}})$  and  $r_{2D}(\theta_{\text{ap}})$  for lens galaxies at  $z_d = 0.3$ . Each panel varies only one template parameter. See text for more details.

templates. Nevertheless,  $b(m)$  can be shown to obey

$$\int_0^\infty dm n(m) m b(m) = \bar{\rho}_m \iff \int_0^\infty dm w_{01}^{2h}(m) b(m) = 1 \quad (84)$$

which follows from the Eqs. (57) and (45). When plotting  $b(m)$ , we make sure that it is normalised correspondingly.

Furthermore for the templates, we assume that satellite galaxies always trace the halo matter density so that  $\tilde{u}_g(k, m) \equiv \tilde{u}_m(k, m)$ . This assumption could be relaxed in a future model extension. For the matter density profile  $\tilde{u}_m(k, m)$ , we assume a NFW profile (Navarro et al. 1996) with a mass concentration as in Seljak (2000) and a halo mass spectrum  $n(m)$  according to Sheth & Tormen (1999). For the average biasing functions  $b(k)$  and  $r(k)$ , we evaluate  $n(m)$ ,  $b_h(m)$ , and  $\tilde{u}_m(k, m)$  at the mean redshift of the lens galaxies. As model for  $P_m(k; \chi)$  in Sect. 3.2 we employ the publicly available code *nicaea*<sup>2</sup> version 2.5 (Kilbinger et al. 2009) that provides an implementation of Halofit with the recent update by Takahashi et al. (2012) and the matter transfer-function in Eisenstein & Hu (1998) for baryonic oscillations.

We list all free parameters of the templates in Table 2. Their total number is 47 by default. In a future application, we may also consider  $r_{\text{ls}}$  a free parameter to test, for instance, the validity of  $r_{\text{ls}} = 1$ . If no large-scale information on the aperture statistics

is available, we predict  $b_{\text{ls}}$  from Eq. (69), reducing the degrees of freedom in the model by one.

To obtain the biasing functions  $b(k)$  and  $r(k)$  from the set of parameters we proceed as follows. We first compute the one-halo terms (58) and (63) for two separate scenarios: with and without central galaxies. Both scenarios are then mixed according to the Eqs. (73) and (74) for the given value of  $f_{\text{cen}}$ . Finally, we patch together the one- and two-halo biasing functions according to Eqs. (43) and (40) with a weight  $W_m(k)$  for the fiducial cosmology.

### 5.3. Physical discussion

Fig. 6 is a showcase of conceivable biasing functions and their relation to the underlying galaxy physics which we compute in the aforementioned way. The wave number  $k$  is plotted on the top axis, whereas the bottom axis is defined by  $\theta_{\text{ap}} = 4.25/(k f_K(z_d))$  for a lens redshift of  $z_d = 0.3$ , which is essentially a simplistic prediction for  $b_{2D}(\theta_{\text{ap}})$  and  $r_{2D}(\theta_{\text{ap}})$  as observed by the lensing technique in Sect. 3. For the discussion here, we concentrate on the spatial biasing functions.

We plot both  $b(k)$  and  $r(k)$  inside each panel. The black lines show a family of  $b(k)$  that we obtain by varying one template parameter at a time in a fiducial model; the red lines are families of  $r(k)$ . The varied parameter is indicated in the top right

<sup>2</sup> <http://www.cosmostat.org/software/nicaea/>

corner of each panel. We assume a large-scale bias  $b_{ls}$  according to Eq. (69) with the theoretical halo bias  $b_h(m)$  in Tinker et al. (2005). The fiducial model has: (i) no central galaxies,  $f_{cen} = 0$ ; (ii) a constant  $b(m) > 0$  for  $m \in [10^9, 10^{15}] h^{-1} M_\odot$  but vanishing everywhere else; (iii) a Poisson HOD-variance,  $V(m) = 0$ , for all halo masses; and (iv) a pivotal mass of  $m_{piv} = 10^{11} h^{-1} M_\odot$ . This setup results in a large-scale bias factor of  $b_{ls} = 1.48$ . The details of the panels are as follows.

- The bottom left panel varies  $f_{cen}$  between zero and 100% in steps of 20% (bottom to top lines). Affected by a change of  $f_{cen}$  are only the small scales  $k \gtrsim 10 h^{-1} \text{Mpc}$  (or  $\theta_{ap} \lesssim 1 \text{ arcmin}$ ) that are strongly influenced by low-mass, low-occupancy halos.
- The bottom right panel increases  $m_{piv}$  from  $10^9 h^{-1} M_\odot$  (bottom line) to  $10^{13} h^{-1} M_\odot$  (top line) in steps of one dex. An impact on the bias functions is only visible if we have either a non-Poisson HOD variance or central galaxies. We hence set  $f_{cen} = 20\%$  compared to the fiducial model. A greater value of  $m_{piv}$  shifts the mass scale of low-occupancy halos to larger masses and thus their impact on the bias functions to larger scales.
- In the top left panel, we adopt a sub-Poisson model of  $V(m) = \max\{-0.5, -\langle N|m \rangle\}$  for halos with  $m \leq m_v$ . We step up the mass scale  $m_v$  from  $10^{10} h^{-1} M_\odot$  (bottom line for  $r$ ; top line for  $b$ ) to  $10^{14} h^{-1} M_\odot$  (top line for  $r$ ; bottom line for  $b$ ) in one dex steps. Similar to the toy model in Sect. 4.3, a sub-Poisson variance produces opposite trends for  $b$  and  $r$ : if  $b$  goes up,  $r$  goes down, and vice versa. The effect is prominent at small scales where low-occupancy halos significantly contribute to the bias functions. Conversely to what is shown here, these trends in  $b$  and  $r$  change signs if we adopt a super-Poisson variance instead of a sub-Poisson variance for  $m \leq m_v$ , which means that  $V(m) > 0$ .
- The top right panel varies the mean biasing function  $b(m)$ . To achieve this we consider a mass-cutoff scale  $m_f$  beyond which halos not harbour any galaxies, that means  $b(m) = 0$ . We reduce this cutoff from  $m_f = 10^{15} h^{-1} M_\odot$  down to  $10^{11} h^{-1} M_\odot$  by one dex in each step (top to bottom line). This gradually excludes galaxies from high-mass halos on the mass scale. Broadly speaking, we remove galaxies from massive clusters first, then groups, and retain only field galaxies in the end. In the same way as for a non-Poisson HOD or present central galaxies this gives rise to a strong scale-dependence in the bias functions but now clearly visible on all scales. Despite its complex scale-dependence, the correlation factor stays always  $r(k) \leq 1$  because of the Poisson HOD variance and the absence of central galaxies in the default model.

This behaviour of the biasing functions is qualitatively similar to what is seen in the related analytic model by Cacciato et al. (2012), where deviations from either faithful galaxies, a Poissonian HOD, or a constant mean biasing function  $b(m) \equiv 1$  are also necessary for biased galaxies. Moreover, the scale-dependence that is induced by central galaxies or a non-Poisson HOD variance is there, as for our templates, restricted to small scales in the one-halo (low-occupancy halo) regime, typically below a few  $h^{-1} \text{Mpc}$ . However, their model has a different purpose than our templates and is therefore less flexible. To make useful predictions of biasing functions for luminosity-selected galaxies they assume (apart from different technicalities as to the treatment of centrals and satellites) that: the mean galaxy number  $\langle N|m \rangle$  is strongly confined by realistic conditional luminosity-functions ( $b(m)$  is not free); their ‘Poisson

function’  $\beta(m) := V(m)/\langle N|m \rangle + 1$  is a constant ( $V(m)$  is not free); the large-scale biasing factor  $b_{ls}$  is determined by  $b(m)$ . Especially, the freedom of  $b(m)$  facilitates our templates with the flexibility to vary over a large range of scales (top right panel in Fig. 6), which may be required for galaxies with a complex selection function.

## 6. Practical inference of biasing functions

In this section, we construct a methodology to statistically infer the biasing functions  $b(k)$  and  $r(k)$  from noisy observations of the lensing aperture statistics  $\langle N^2 \rangle$ ,  $\langle NM_{ap} \rangle$ , and  $\langle M_{ap}^2 \rangle$ . The general idea is to utilise the model templates in Sect. 5 and to constrain the space of their parameters by the likelihood of the observed ratio statistics  $b_{2D}(\theta_{ap})$  and  $r_{2D}(\theta_{ap})$ . The posterior distribution of templates will constitute the posterior of the deprojected biasing functions.

To estimate the aperture statistics from lens and source catalogues we employ standard techniques that we summarise in Appendix B for a practical reference. We shall assume that we have measurements of the aperture statistics and their joint error covariance in the following, based on estimates of lens-lens, lens-shear, and shear-shear correlation functions between 1.4 arcsec to 280 arcmin and 64 jackknife samples. The aperture statistics are computed for nine radii  $\theta_{ap}$  between 1.8 arcmin and 140 arcmin.

### 6.1. Statistical analysis

In our statistical analysis, we fit for a set of  $n_d$  aperture radii  $\theta_i$  a model of the aperture statistics  $b_{2D}(\theta_i; b)$  and  $r_{2D}(\theta_i; b, r)$ , Eqs. (26) and (27), to the measurement of the ratio statistics  $b_{2D}(\theta_i)$  and  $r_{2D}(\theta_i)$ , Eqs. (14) and (15). Ratios of the noisy aperture statistics result in a skewed error distribution for  $b_{2D}$  and  $r_{2D}$  which we account for in a non-Gaussian model likelihood that assumes Gaussian errors for the aperture moments  $\langle N^2 \rangle$ ,  $\langle NM_{ap} \rangle$ ,  $\langle M_{ap}^2 \rangle$  themselves (and positive values for the variances).

With regard to the validity of a (truncated) Gaussian model for the aperture moments, at least for current cosmic-shear studies this is known to be a sufficiently accurate approximation (e.g. Hildebrandt et al. 2017; Kilbinger et al. 2013). Nevertheless, our statistical tests in Appendix C find evidence for a non-Gaussian statistics in our mock data, especially for the variance  $\langle M_{ap}^2 \rangle$  on scales of one degree or larger. This may bias the reconstruction of  $b(k)$  and  $r(k)$  which will eventually be contained in our assessment of systematic errors later on.

To motivate our model likelihood for  $b_{2D}(\theta_i)$  and  $r_{2D}(\theta_i)$ , let us first consider a simpler case where  $\hat{x} = x + \delta x$  and  $\hat{y} = y + \delta y$  are measurements of two numbers  $x$  and  $y$ , respectively, with a bivariate PDF  $p_\delta(\delta x, \delta y)$  for the noise in the measurement. Our aim shall be to constrain the ratio  $R = \sqrt{y/x}$ . The posterior PDF  $p(R|\hat{x}, \hat{y})$  of  $R$  given  $\hat{x}$  and  $\hat{y}$  can be written as the marginal PDF

$$p(R|\hat{x}, \hat{y}) = \int dx p(R, x|\hat{x}, \hat{y}) \quad (85)$$

$$\propto \int dx \mathcal{L}(\hat{x}, \hat{y}|R, x) p(x) p(R) \quad (86)$$

$$= p(R) \int dx p_\delta(\hat{x} - x, \hat{y} - R^2 x) p(x), \quad (87)$$

where  $\mathcal{L}(\hat{x}, \hat{y}|R, x)$  shall be the likelihood of  $(\hat{x}, \hat{y})$  given a value pair  $(x, R)$ , and the product  $p(x) p(R)$  is the joint prior of  $(x, R)$



(see Gelman et al. 2003, for a introduction to Bayesian statistics). We see that the integral in the last line,

$$\mathcal{L}(\hat{x}, \hat{y}|R) := \int dx p_\delta(\hat{x} - x, \hat{y} - R^2 x) p(x), \quad (88)$$

has to be the likelihood of  $(\hat{x}, \hat{y})$  for a given ratio  $R$ . We are thus essentially fitting a two-parameter model  $(R, x)$  to  $\hat{y} = R^2 x$  and  $\hat{x} = x$  followed by a marginalising over  $x$ . Coming back to our statistical analysis of the aperture statistics,  $y$  and  $x$  would be here  $f_b^2 \langle \mathcal{N}^2 \rangle$  and  $\langle M_{\text{ap}}^2 \rangle$ , for example, and  $R = f_b \langle \mathcal{N}^2 \rangle^{1/2} \langle M_{\text{ap}}^2 \rangle^{-1/2}$  is the (projected) bias factor  $b_{2D}$ . For our full analysis, however, we have to jointly constrain  $b_{2D}$  and the correlation factor  $r_{2D}$  for a set of aperture radii  $\theta_i$  in a more general approach.

To implement a general approach involving  $n_d$  aperture radii and both the bias and correlation factors for all radii simultaneously, we combine the measurements of aperture moments inside the data vector with the (observed) elements

$$d_j = \begin{cases} \langle \mathcal{N}^2(\theta_j) \rangle, & 1 \leq j \leq n_d \\ \langle NM_{\text{ap}}(\theta_{j-n_d}) \rangle, & n_d < j \leq 2n_d \\ \langle M_{\text{ap}}^2(\theta_{j-2n_d}) \rangle, & 2n_d < j \leq 3n_d \end{cases}, \quad (89)$$

and we fit this vector by the parameters  $\mathbf{m}(\Theta, \mathbf{x})$  with template parameters  $\Theta$  (Table 2) and (theoretical) vector elements

$$m_j(\Theta, \mathbf{x}) = \begin{cases} \frac{\langle \mathcal{N}^2 \rangle_{\text{th}}(\theta_j; b) x_j}{\langle M_{\text{ap}}^2 \rangle_{\text{th}}(\theta_j)}, & 1 \leq j \leq n_d \\ \frac{\langle NM_{\text{ap}} \rangle_{\text{th}}(\theta_{j-n_d}; b, r) x_{j-n_d}}{\langle M_{\text{ap}}^2 \rangle_{\text{th}}(\theta_{j-n_d})}, & n_d < j \leq 2n_d \\ x_{j-2n_d}, & 2n_d < j \leq 3n_d \end{cases} \quad (90)$$

using a PDF  $p_\delta(\delta\mathbf{d})$  that accounts for the correlated noise  $\delta\mathbf{d}$  in the aperture statistics. The details of this PDF are given below. We note that the explicit normalisation  $f_b(\theta_i)$  and  $f_r(\theta_i)$  disappears here because both the theoretical and observed ratio-statistics  $\{(b_{2D}(\theta_i), r_{2D}(\theta_i))\}$  are normalised exactly the same way. However, the normalisation is indirectly present through the ratio of theoretical aperture moments in  $\mathbf{m}(\Theta, \mathbf{x})$  so that a wrong normalisation will introduce a bias in the reconstruction. Similar to the previous illustration, we integrate over the nuisance parameter  $x_i = \langle M_{\text{ap}}^2(\theta_i) \rangle$  to obtain the marginal likelihood

$$\mathcal{L}(\mathbf{d}|\Theta) = \int d^{n_d} x p_\delta(\mathbf{d} - \mathbf{m}(\Theta, \mathbf{x})) p(\mathbf{x}). \quad (91)$$

We adopt a uniform prior  $p(\mathbf{x})$  for  $\mathbf{x}$  with the additional condition that the variance of the aperture mass has to be positive or zero.

The measurement noise  $\delta\mathbf{d}$  in the aperture statistics approximately obeys Gaussian statistics which is characterised by a noise covariance  $\mathbf{N} = \langle \delta\mathbf{d} \delta\mathbf{d}^T \rangle$ ; the mean  $\langle \delta\mathbf{d} \rangle$  vanishes by definition. The exact covariance  $\mathbf{N}$ , however, is unknown so that we estimate  $\mathbf{N}$  from the data themselves by  $\hat{\mathbf{N}}$ , obtained with  $n_{\text{jk}}$  jackknife realisations of the data (Appendix B). We include the uncertainty of  $\hat{\mathbf{N}}$  in the posterior of the spatial biasing functions by analytically marginalising over its statistical error. As shown in Sellentin & Heavens (2016), this produces for Gaussian  $\delta\mathbf{d}$  a multivariate  $t$ -distribution for the noise model  $p_\delta(\delta\mathbf{d})$ ,

$$-2 \ln p_\delta(\delta\mathbf{d}) = \text{const} + n_{\text{jk}} \ln \left( 1 + \frac{\chi^2}{n_{\text{jk}} - 1} \right), \quad (92)$$

where  $\chi^2 := \delta\mathbf{d}^T \hat{\mathbf{N}}^{-1} \delta\mathbf{d}$ .

To approximately evaluate (91), we perform a numerical Monte-Carlo integration

$$\mathcal{L}(\mathbf{d}|\Theta) = \int d^{n_d} x q(\mathbf{x}) \frac{p_\delta(\mathbf{d} - \mathbf{m}(\Theta, \mathbf{x})) p(\mathbf{x})}{q(\mathbf{x})} \quad (93)$$

$$\approx \frac{1}{n_x} \sum_{i=1}^{n_x} \frac{p_\delta(\mathbf{d} - \mathbf{m}(\Theta, \mathbf{x}_i)) p(\mathbf{x}_i)}{q(\mathbf{x}_i)}, \quad (94)$$

for which

$$-2 \ln q(\mathbf{x}) = \text{const} + (\mathbf{x} - \mathbf{d}_{\text{map}})^T \mathbf{N}_{\text{map}}^{-1} (\mathbf{x} - \mathbf{d}_{\text{map}}) \quad (95)$$

is a so-called importance function of the Monte-Carlo integral, and  $\mathbf{d}_{\text{map},j} = \langle M_{\text{ap}}^2(\theta_j) \rangle$  are the measured variances of the aperture mass at  $\theta_j$ ; the vectors  $\mathbf{x}_i \sim q(\mathbf{x})$  are  $n_x$  random realisations of the importance function; the matrix  $\mathbf{N}_{\text{map}}^{-1}$  denotes our estimate for the inverse covariance of noise in  $\mathbf{d}_{\text{map}}$ , that is that of  $\langle M_{\text{ap}}^2 \rangle$  alone, which we also obtain from jackknife samples and the estimator in Hartlap et al. (2007). The purpose of the importance function  $q(\mathbf{x})$  is to improve the convergence of the Monte-Carlo sum (94) by producing a higher density of sampling points  $\mathbf{x}_i$  where the most of the probability mass of  $p_\delta(\mathbf{d} - \mathbf{m}(\Theta, \mathbf{x}))$  is located (e.g. Kilbinger et al. 2010). We note that for any  $q(\mathbf{x})$  the sum always converges to the same  $\mathcal{L}(\mathbf{d}|\Theta)$  as long as  $q(\mathbf{x})$  is proper and  $q(\mathbf{x}) > 0$  for all  $\mathbf{x}$ . To save computation time, we initially prepare  $n_x = 10^3$  realisations  $\mathbf{x}_i$  and reuse these for every new estimation of the marginal likelihood in (94).

We explore the posterior distribution of parameters  $\Theta$  in the template, that is

$$p(\Theta|\mathbf{d}) = E^{-1}(\mathbf{d}) \mathcal{L}(\mathbf{d}|\Theta) p(\Theta) \propto \mathcal{L}(\mathbf{d}|\Theta) p(\Theta), \quad (96)$$

by applying sampling with the Multiple-Try Metropolis, where the constant evidence  $E(\mathbf{d})$  is not of interest here (Martino & Read 2012). We assume that the prior  $p(\Theta)$  is uniform on a linear scale for all parameters within their defined boundaries, see Sect. 5.2, and  $0 < b_{\text{ls}} \leq 3$ . Different Monte-Carlo chains can be combined by joining the different sets of sampling points from independent Monte-Carlo runs. If the joint sample is too large to be practical, a resampling can be applied. This means we randomly draw a subset of points  $\Theta_i$  from the joint sample. Depending on the details of the adopted MCMC algorithm, the probability of drawing  $\Theta_i$  in the resampling has to be proportional to its weight in case points are not equally weighted.

Finally to conclude the reconstruction, we map the Monte-Carlo realisations of  $\Theta$  in the joint sample to a set of spatial biasing functions. The final set then samples the posterior distribution of  $b(k)$  and  $r(k)$ .

## 6.2. Marginalisation of errors in the galaxy-bias normalisation

For our analysis, the fiducial cosmology and the intrinsic alignment of sources is exactly known by the cosmological model in the mock data. For future applications, however, it may be necessary to additionally marginalise over an a priori uncertainty  $p(\boldsymbol{\pi})$  of cosmological parameters  $\boldsymbol{\pi}$  for the normalisation of the galaxy bias, meaning that the  $\Theta$  posterior is

$$p(\Theta|\mathbf{d}) \propto \int d\boldsymbol{\pi} p(\boldsymbol{\pi}) \mathcal{L}(\mathbf{d}|\Theta, \boldsymbol{\pi}) p(\Theta) \approx \sum_{i=1}^{n_\pi} \frac{\mathcal{L}(\mathbf{d}|\Theta, \boldsymbol{\pi}_i) p(\Theta)}{n_\pi}, \quad (97)$$

where  $\mathcal{L}(\mathbf{d}|\mathbf{\Theta}, \boldsymbol{\pi})$  is the likelihood of  $\mathbf{d}$  for a given set  $\mathbf{\Theta}$  and fiducial cosmology  $\boldsymbol{\pi}$ . Numerically the marginalisation over  $\boldsymbol{\pi}$  can be achieved, as indicated by the right-hand side of (97), by (i) randomly drawing a realisation  $\boldsymbol{\pi}_i$  from the prior  $p(\boldsymbol{\pi})$ , (ii) by performing the Monte-Carlo sampling of the posterior in Eq. (96) for the fixed fiducial cosmology  $\boldsymbol{\pi}_i \sim p(\boldsymbol{\pi})$ , and (iii) by combining the different chains with varying  $\boldsymbol{\pi}$ . Concretely, let us call the resulting Monte-Carlo sample from step (ii)  $\mathcal{M}_i$ . We repeat this step  $n_\pi$  times for different cosmologies. For joining the chains in step (iii), we randomly draw one  $\mathbf{\Theta}_i$  from each sample  $\mathcal{M}_i$  to produce  $n_\pi$  new vectors  $\mathbf{\Theta}$  that go into the final sample. We repeat this random selection of  $n_\pi$ -tupels until the final sample has the desired size. We may apply the same technique to also marginalise over errors in the redshift distributions of lenses and sources, or the uncertainties in the II and GI models.

### 6.3. Galaxy number density as prior

The halo model provides a prediction of the mean galaxy density  $\bar{n}_g(\mathbf{\Theta})$ , Eq. (83), that can be included in the template fit to improve the constraints on the otherwise poorly constrained pivot mass  $m_{\text{piv}}$ . We may achieve this by adding the log-normal likelihood

$$\ln \mathcal{L}(\bar{n}_g|\mathbf{\Theta}) = -\frac{(\log_{10} \bar{n}_g^{\text{est}} - \log_{10} \bar{n}_g(\mathbf{\Theta}))^2}{2\sigma_{\log n}^2}, \quad (98)$$

to the logarithm of the marginal likelihood in (94). Here we denote by  $\sigma_{\log n}^2$  the root-mean-square (RMS) error of the logarithmic number density  $\bar{n}_g^{\text{est}}$  estimated from the data.

A reasonable prior on  $\bar{n}_g$  can also be found if  $\bar{n}_g^{\text{est}}$  is not available as it is assumed here. The number density of galaxies is for redshifts  $z \lesssim 2$  typically of the order of  $10^{-2}$  to  $10^{-1} h^3 \text{Mpc}^{-3}$ , or smaller for sub-samples (e.g. Conselice et al. 2016). Therefore in the reconstruction of our biasing functions, we employ a weak Gaussian prior of

$$\log_{10} (\bar{n}_g^{\text{est}} h^{-3} \text{Mpc}^3) \pm \sigma_{\log n} = -3 \pm 2 \quad (99)$$

for the galaxy number density, and we impose an upper limit of  $\bar{n}_g(\mathbf{\Theta}) \leq 1 h^3 \text{Mpc}^{-3}$  to prevent an nonphysically high number density of galaxies. We found that the upper limit improves the convergence of the MCMCs as chains can get stuck at low values of  $m_{\text{piv}}$  with unrealistically high values of  $\bar{n}_g$ .

## 7. Results

In the following, we report our results for the reconstructed biasing functions for the galaxy samples SM1 to SM6, RED, and BLUE inside the two redshift bins low- $z$  ( $\bar{z}_d \approx 0.36$ ) and high- $z$  ( $\bar{z}_d \approx 0.52$ ). We concentrate on the reconstruction accuracy and precision although the template parameters found in the reconstructions are also available in the Appendix D. If not stated otherwise, the results are for mock sources with a shape-noise dispersion  $\sigma_\epsilon = 0.3$  and without reduced shear. As additional test of the methodology, we use generic templates for a non-physical model of the spatial biasing functions and compare the results to those of our physical templates. Furthermore, we estimate the systematic error in the bias normalisation originating from various conceivable sources. The final sub-section is a demonstration of our technique with data from the Garching-Bonn Deep Survey (GaBoDS).

### 7.1. Reconstruction accuracy and precision

The Figs. 7 and 8 are a direct comparison of our reconstructed biasing functions for all samples (shaded regions) to the true  $b(k; \bar{z})$  and  $r(k; \bar{z})$  in the three-dimensional simulation cube of the MS shown as red data points; we use the snapshot redshifts  $\bar{z} = 0.362, 0.509$  for low- $z$  and high- $z$  respectively. The shaded region indicate the 68% and 95% posterior intervals (PI) of our posterior constraints. In order to accommodate many reconstructions, we have shifted the biasing function along the y-axes by a constant value that is indicated in the legend of each plot. We note that most functions are shifted downwards so that relative errors might appear larger than in reality. The left panels show  $b(k)$ , the right panels  $r(k)$ . Figure 7 displays only reconstructions for the stellar-mass samples where the top row is for the low- $z$  samples and the bottom row for the high- $z$  samples. Similarly, Fig. 8 shows the results for the RED and BLUE samples, now low- $z$  and high- $z$  combined in one figure.

Overall we find a good agreement between a reconstruction and the true biasing functions although significant disagreements are also visible. Most prominently, we find disagreements at large scales, this means at small wave numbers  $k \approx 0.05 h \text{Mpc}^{-1}$ , for the low- $z$   $b(k)$  of RED, SM1, and SM5; or at small scales,  $k \approx 10 h^{-1} \text{Mpc}$ , for the high- $z$   $r(k)$  of SM2 or BLUE; the function low- $z$   $b(k)$  of SM2 and SM3 is a few per cent offset on all scales which may be an indication of a normalisation error. The disagreement at high  $k \gtrsim 10 h^{-1} \text{Mpc}$  could be related to insufficient sampling by our MCMC because the results improve significantly for samples without shape noise which reduces the statistical error at  $\theta_{\text{ap}} \approx 2'$  (not shown). It is also possible that the statistical model of the likelihood in Eq. (92) is inaccurate and, as a consequence, underestimates the error distribution in the tail of the posterior at large  $k$ .

To quantify the method accuracy we compare the reconstruction  $b(k)$  or  $r(k)$  to the true biasing function by the following metrics  $\sigma_f^2$  and  $\Delta_f$ ; the subscript ‘f’ is either ‘b’ for  $b(k)$  or ‘r’ for  $r(k)$ . The metrics compare the biasing functions at a discrete set  $\{k_i : i = 1 \dots n_k\}$  of  $n_k = 10$  wave numbers between  $0.05 \leq k \leq 10 h \text{Mpc}^{-1}$ , which we equally space on a log-scale. In the equations, we denote by  $f(k)$  the posterior median of either  $b(k)$  or  $r(k)$  in the reconstruction, and  $\sigma^2(k)$  is the variance of the posterior at a given  $k$ . In addition, we denote by  $f_{\text{true}}(k)$  the true biasing function and by  $\sigma_{\text{true}}^2(k)$  its standard error. The variance  $\sigma_{\text{true}}^2(k)$  is indicated by the error bars of the red data points in the Figs. 7 and 8; it is usually negligible compared to  $\sigma^2(k)$ . Our first metric

$$\sigma_f^2 = \left( \sum_{i=1}^{n_k} \sigma_i^{-2} \right)^{-1} \sum_{i=1}^{n_k} \sigma_i^{-2} \left( \frac{f(k_i)}{f_{\text{true}}(k_i)} - 1 \right)^2 \quad (100)$$

then quantifies the average fractional error over the range of  $k$ , weighted by the inverse statistical error  $\sigma_i^2 = \sigma^2(k_i) + \sigma_{\text{true}}^2(k_i)$ . For  $\sigma_f^2$ , we change the lower limit of  $k$  to  $0.3 h \text{Mpc}^{-1}$  to avoid a seemingly too optimistic metric: by definition  $r(k)$  is in the reconstruction close to the true  $r(k) = 1$  of the MS data which makes  $\sigma_i$  relatively small and therefore assigns too much weight to  $k \lesssim 0.3 h \text{Mpc}^{-1}$ . The second metric

$$\Delta_f = \max \left\{ \sigma_i^{-1} |f(k_i) - f_{\text{true}}(k_i)| : i = 1 \dots n_k \right\} \quad (101)$$

yields the most significant deviation in units of  $\sigma_i$ ; it is a measure for the strongest outlier within the  $k$ -range.

Table 3 lists  $\sigma_f$  (in per cent) and  $\Delta_f$  for all galaxy samples and redshift bins; the last rows are averages and dispersions for

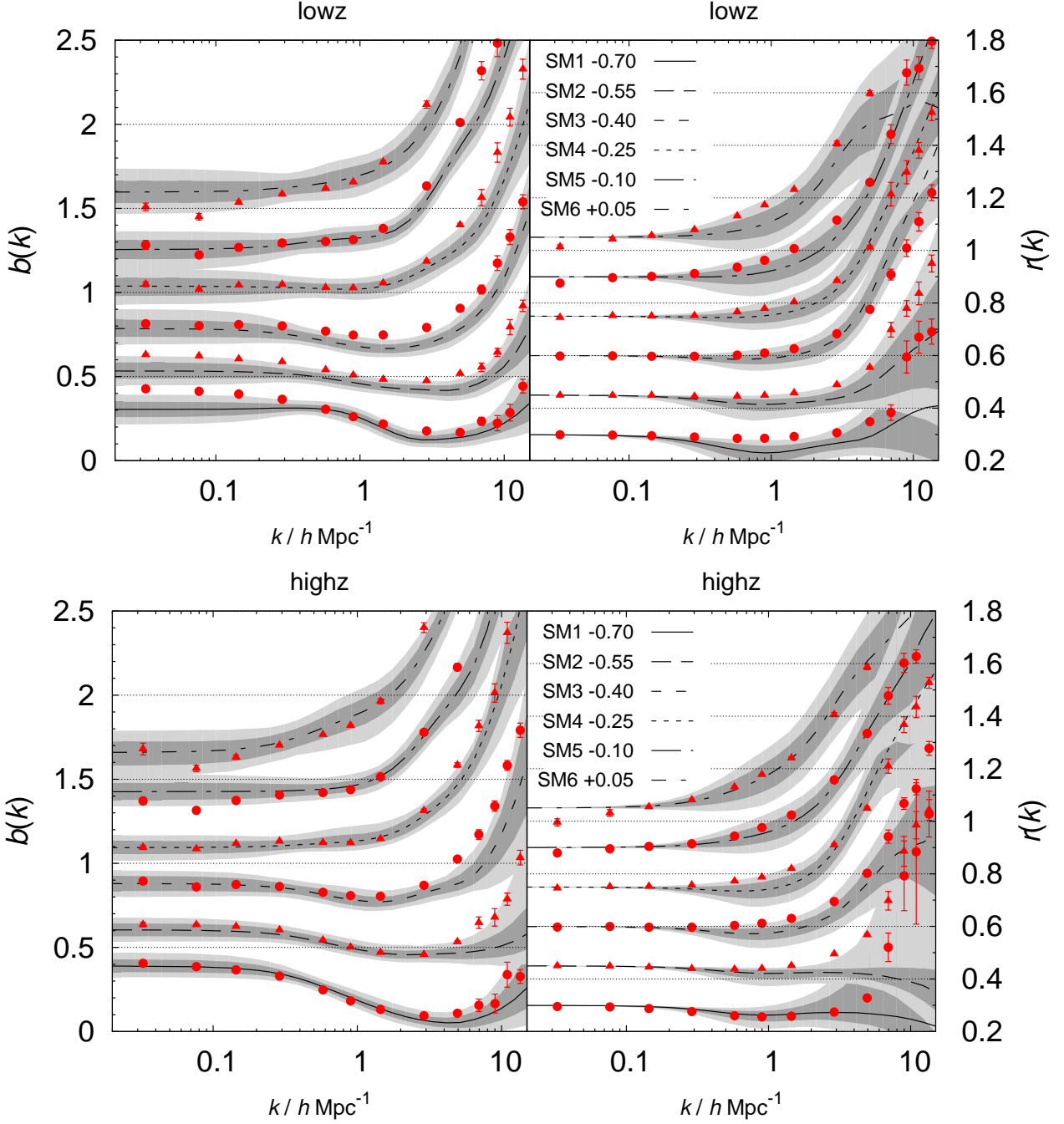


**Fig. 7.** Biasing functions  $b(k)$  (left panels) and  $r(k)$  (right panels) for all mock galaxy samples SM1 to SM6 and two redshift bins. The top figure is for the low- $z$  samples ( $\bar{z}_d \approx 0.36$ ); the bottom figure for the high- $z$  samples ( $\bar{z}_d \approx 0.52$ ). The shaded regions indicate the 68% and 95% PI of the reconstructed biasing functions. The red data points are the true biasing functions for comparison. For more visibility, we shifted the biasing functions by the constant value in the figure key.

each table column. The table consists of two blocks of which we summarise the left-hand columns ‘physical’ here and the right-hand column ‘generic’ in the Sect. 7.2 hereafter. The values for  $\sigma_b$  are typically in the range  $5.4 \pm 2.9\%$  for low- $z$  samples and slightly better with  $3.6 \pm 1.7\%$  for the high- $z$  samples. The accuracy of  $\sigma_r$  is consistently  $3.0 \pm 2.0\%$  for both redshift bins. For the outlier statistics, we find on average  $\Delta_b = 2.2 \pm 1.2\sigma$  and  $\Delta_r = 2.2 \pm 1.8\sigma$  for all redshifts, which, however, can attain high values of  $6 - 7\sigma$  in a few cases; see high- $z$  BLUE and SM2 for instance. We find these high values to be associated with mis-

matches of  $r(k)$  at  $k \approx 10 h \text{ Mpc}^{-1}$ . This corresponds to  $\theta_{\text{ap}} \approx 1'$ , thus to the lower limit of the angular scales that we sample in the mock analysis (cf. bottom and top  $x$ -axis in Fig. 6).

Moreover, we quantify the statistical precision of our reconstruction at wave number  $k_i$  by the ratio of  $\sigma(k_i)$  and the median of the posterior of either  $f(k_i)$ . For an average over all galaxy samples and the reconstruction within the range  $0.05 \leq k \leq 10 h \text{ Mpc}^{-1}$ , we find a precision of  $6.5 \pm 2.1\%$  for  $b(k)$  and  $5.5 \pm 5.7\%$  for  $r(k)$ ; we combine the low- $z$  and high- $z$

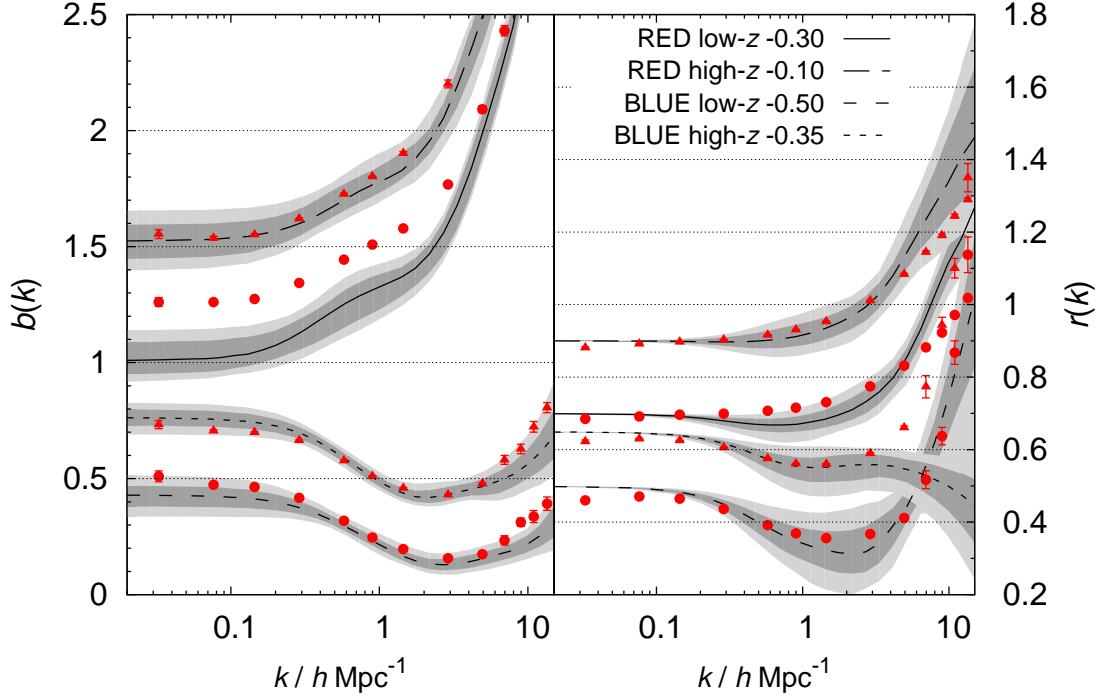


**Fig. 8.** As in Fig. 7 but now for the colour-selected samples RED and BLUE.

**Table 3.** Overview of the reconstruction accuracy by listing the mean fractional errors  $\sigma_{b,r}$  and extreme outliers  $\Delta_{b,r}$  of the inferred biasing functions  $b(k)$  and  $r(k)$ , respectively, in per cent.

Sample	<i>physical</i> low- <i>z</i>		<i>physical</i> high- <i>z</i>		<i>generic</i> low- <i>z</i>		<i>generic</i> high- <i>z</i>	
	$\sigma_b$ ( $\Delta_b$ )	$\sigma_r$ ( $\Delta_r$ )	$\sigma_b$ ( $\Delta_b$ )	$\sigma_r$ ( $\Delta_r$ )	$\sigma_b$ ( $\Delta_b$ )	$\sigma_r$ ( $\Delta_r$ )	$\sigma_b$ ( $\Delta_b$ )	$\sigma_r$ ( $\Delta_r$ )
SM1	4.9 (3.0 $\sigma$ )	3.9 (1.9 $\sigma$ )	3.0 (2.1 $\sigma$ )	1.4 (1.4 $\sigma$ )	3.4 (1.8 $\sigma$ )	4.9 (0.9 $\sigma$ )	4.4 ( <b>3.8</b> $\sigma$ )	<b>6.0</b> (4.6 $\sigma$ )
SM2	<b>6.2</b> (3.1 $\sigma$ )	2.7 (1.9 $\sigma$ )	4.4 ( <b>3.9</b> $\sigma$ )	4.6 ( <b>7.2</b> $\sigma$ )	<b>6.9</b> (7.5 $\sigma$ )	4.0 (1.2 $\sigma$ )	4.2 ( <b>3.2</b> $\sigma$ )	1.9 (1.5 $\sigma$ )
SM3	<b>6.5</b> (2.8 $\sigma$ )	1.7 (1.7 $\sigma$ )	3.4 (1.8 $\sigma$ )	2.9 (1.9 $\sigma$ )	<b>5.8</b> (3.4 $\sigma$ )	1.7 (1.6 $\sigma$ )	2.4 (2.2 $\sigma$ )	1.5 (1.5 $\sigma$ )
SM4	3.2 (1.9 $\sigma$ )	2.0 (1.0 $\sigma$ )	2.4 (1.6 $\sigma$ )	3.5 (1.7 $\sigma$ )	2.8 (2.7 $\sigma$ )	0.9 (1.1 $\sigma$ )	4.1 (2.3 $\sigma$ )	1.6 (1.3 $\sigma$ )
SM5	3.1 (1.4 $\sigma$ )	3.2 (1.2 $\sigma$ )	3.8 (1.5 $\sigma$ )	1.4 (0.6 $\sigma$ )	3.1 (1.6 $\sigma$ )	0.9 (0.5 $\sigma$ )	<b>19.3</b> (3.5 $\sigma$ )	<b>9.2</b> (2.2 $\sigma$ )
SM6	<b>5.2</b> (1.4 $\sigma$ )	4.5 (1.8 $\sigma$ )	<b>5.6</b> (1.4 $\sigma$ )	2.5 (1.0 $\sigma$ )	<b>5.8</b> (1.7 $\sigma$ )	<b>5.7</b> (1.5 $\sigma$ )	<b>7.6</b> (2.5 $\sigma$ )	<b>7.9</b> (1.3 $\sigma$ )
RED	<b>9.4</b> (2.2 $\sigma$ )	4.6 ( <b>3.1</b> $\sigma$ )	3.0 (1.1 $\sigma$ )	2.0 (1.2 $\sigma$ )	<b>11.1</b> (37.6 $\sigma$ )	3.7 ( <b>6.9</b> $\sigma$ )	<b>10.3</b> (19.8 $\sigma$ )	2.7 ( <b>5.7</b> $\sigma$ )
BLUE	4.6 ( <b>3.8</b> $\sigma$ )	1.7 (1.4 $\sigma$ )	3.2 (1.8 $\sigma$ )	<b>6.0</b> (5.6 $\sigma$ )	<b>5.4</b> (2.7 $\sigma$ )	3.1 (1.1 $\sigma$ )	2.7 (1.9 $\sigma$ )	<b>8.9</b> (2.0 $\sigma$ )
$\langle\sigma_{b,r}\rangle$	$5.4 \pm 2.9$	$3.0 \pm 1.7$	$3.6 \pm 1.7$	$3.0 \pm 2.0$	$5.5 \pm 3.4$	$3.1 \pm 2.2$	$6.9 \pm 6.2$	$5.0 \pm 3.9$
$\langle\Delta_{b,r}\rangle$	$2.5 \pm 1.3\sigma$	$1.8 \pm 0.9\sigma$	$1.9 \pm 1.1\sigma$	$2.6 \pm 2.6\sigma$	$7.4 \pm 12.7\sigma$	$1.9 \pm 2.2\sigma$	$4.9 \pm 6.3\sigma$	$2.5 \pm 1.9\sigma$

**Notes.** The columns ‘physical’ refer to results with a physical model (Sect. 7.1), ‘generic’ columns list the results with generic fitting functions (Sect. 7.2). Quoted values are for the errors in the domain  $k \in [0.05, 10] h \text{ Mpc}^{-1}$  for  $b(k)$  and  $k \in [0.3, 10] h \text{ Mpc}^{-1}$  for  $r(k)$ . The values  $\Delta_b$  and  $\Delta_r$  inside the brackets are the most significant deviations between reconstructed and true biasing functions. Errors  $\sigma_{b,r} \geq 5\%$  or outliers  $\Delta_{b,r} \geq 3\sigma$  are quoted in boldface. Values in the last rows with  $\langle\sigma_{b,r}\rangle$  (or  $\langle\Delta_{b,r}\rangle$ ) are averages and dispersions for  $\sigma_b$  and  $\sigma_r$  (or  $\Delta_b$  and  $\Delta_r$ ) of all samples in the same redshift bin.

samples because the precision is very similar for both bins. The errors denote the RMS variance of the precision.

In summary, we find that a method accuracy of around 5% with most significant deviations at scales of  $k \gtrsim 10 h \text{ Mpc}^{-1}$  which, however, are not supported by the measurements and have to be extrapolated by the templates. The statistical preci-

sion of the reconstructions is typically between 5 – 10% for our fiducial survey and lens samples.

### 7.2. Deprojection with generic templates

We repeat the reconstruction of  $b(k)$  and  $r(k)$  for our mock data with the Padé approximants

$$b(k) = \frac{b_0 + b_1 k + b_2 k^2}{1 + b_3 k + b_4 k^2}; \quad r(k) = \frac{1 + r_1 k + r_2 k^2}{1 + r_3 k + r_4 k^2 + r_0 k^3} \quad (102)$$

as generic templates of the biasing functions in Sect. 6.1 (without a  $\bar{n}_g$  regularisation). The  $b_i$  and  $r_i$  denote ten coefficients which we restrict to  $|b_i|, |r_i| \leq 100$  in the fit. These generic model templates are related to the fitting function for  $b^2(k)$  in Cole et al. (2005). We found that the Padé approximants are very good descriptions of the red data points in the Figs. 7 and 8. By fitting generic templates we therefore investigate whether the foregoing inaccuracies in the reconstruction with the physical templates might be related to a model bias. If this is the case, we should obtain a better reconstruction here. We note that the particular approximant of  $r(k)$  asserts  $r \rightarrow 1$  for  $k \rightarrow 0$ , and that in the generic templates, unlike the physical templates,  $b(k)$  is independent from  $r(k)$ .

Compared to the halo model, the generic templates produce a similar (low- $z$ ) or somewhat worse (high- $z$ ) reconstruction but is prone to more extreme deviations from the true biasing functions. The right-hand block of values ‘generic’ in Table 3 summarises the metrics of the reconstructions with the generic templates and compares them to the metrics with the physical templates ‘physical’ on the left-hand side. We find an increased inaccuracy for the high- $z$  samples, especially for SM5, SM6, and RED; in particular the reconstruction of low- $z$  RED has not improved here. The worse reconstruction for high- $z$  is because of the inability of the generic templates to extrapolate to small spatial scales which is more important for high- $z$  where the same angular range corresponds to larger spatial scales. In a few cases, the generic templates produce very significant deviations, mostly on small scales and indicated by  $\Delta_{b,r}$ , which are absent in the physical templates.

### 7.3. Errors in the galaxy-bias normalisation

The ratio statistics are normalised with respect to unbiased galaxies in a fiducial model. Systematic errors in the normalisation affect the amplitude of the deprojected biasing functions. Therefore, we explore the robustness of the overall amplitude of  $b(k)$  and  $r(k)$  with respect to changes in the fiducial cosmology and the adopted redshift distributions in the normalisation; see the Eqs. (16) and (17) that are evaluated for the unbiased galaxies. We note that  $f_b$  and  $f_r$  normally show little dependence on  $\theta_{ap}$  so that changes in the fiducial model mainly scale the projected biasing functions up or down.

The functions  $f_b(\theta_{ap})$  and  $f_r(\theta_{ap})$  shall be the correct normalisation of the galaxy bias. For Fig. 9, we then compute  $f'_b(\theta_{ap})$  (and  $f'_r(\theta_{ap})$ ) for variations in the normalisation parameters, and we compute the quadratic mean of relative errors  $\delta_b(\theta_{ap}) = f'_b(\theta_{ap})/f_b(\theta_{ap}) - 1$  over the angular range  $1' \leq \theta_{ap} \leq 140'$ . The data points inside the figure indicate these means  $\langle \delta_b^2(\theta_{ap}) \rangle^{1/2}$  (x-axis) and  $\langle \delta_r^2(\theta_{ap}) \rangle^{1/2}$  (y-axis) for particular lens samples. To have a good representation of the scatter between possible lens-galaxy samples, we show results for all galaxy samples SM1-SM6, RED, and BLUE in the same redshift bin together by the same point style if they are subject to the same parameter variation. We give the normalisation errors a plus sign if the average of  $\delta_b(\theta_{ap})$  is positive, and a negative sign otherwise. This flags  $b(k)$  (or  $r(k)$ ) that are overall too high (positive) or too low (negative). We apply variations relative to

**Table 4.** Summary of possible systematic errors and their expected impact on the reconstruction of  $b(k)$  or  $r(k)$  for a WMAP9 cosmology and our galaxy samples.

Origin	Error $b(k)$	Error $r(k)$
intr. align. $ A_{ia}  \approx 2$	$\lesssim 5.0\%$	$\lesssim 5.0\%$
fiducial cosmology and model of $P_m(k; \chi)$	2.8% (3.0%)	0.4% (1.1%)
lens $p_d(z); \delta_\sigma = 5\%$	2.5%	2.2% (2.7%)
lens $p_d(z); \delta_z = 1\%$	1.9%	0.5% (1.4%)
source $p_s(z); \delta_z = 1\%$	1.9%	0.5% (1.0%)
shear bias $m = 1\%$	1.0%	0.0%
shear bias $c \approx 10^{-3}\%$	$< 1.0\%$	$< 1.0\%$
source $p_s(z); \delta_\sigma = 5\%$	0.8%	0.5% (0.3%)
reduced shear	$\lesssim 0.5\%$	$\lesssim 0.5\%$
sampling noise of $p(z)$	0.4% (0.6%)	0.4% (0.5%)

**Notes.** Values in brackets are for the high- $z$  samples ( $\bar{z}_d \approx 0.52$ ) which are only shown if they differ from the low- $z$  values ( $\bar{z}_d \approx 0.35$ ). Sources have a mean redshift of  $\bar{z}_s = 0.93$ . By  $\delta_z$  and  $\delta_\sigma$  we denote the relative error in the mean redshift and the redshift dispersion, respectively, which refer to either the lens redshift distribution,  $p_d(z)$ , or that of the sources,  $p_s(z)$ . We assume a constant residual shear bias  $m$  here.

a default model which has: WMAP9+eCMB+BAO+ $H_0$  cosmological parameters (Hinshaw et al. 2013); redshifts distributions as shown in Fig. 1; a non-linear matter power-spectrum according to Takahashi et al. (2012). Inside the plot, data points have the styles shown in the figure key for low- $z$  samples and an inverted point style for high- $z$  samples, such as solid circles (low- $z$ ) and open circles (high- $z$ ). We vary the following parameters in the default model to quantify their impact on the normalisation.

- The data points ‘cosmo all’ randomly draw combinations of cosmological parameters from an error distribution centred on the fiducial model

$$\pi = (\Omega_m, \Omega_\Lambda, \Omega_b, n_s, h, \sigma_8) = (0.288, 0.712, 0.0472, 0.971, 0.6933, 0.83). \quad (103)$$

In this distribution, errors are uncorrelated and Gaussian with a dispersion of

$$\sigma_\pi = (4\%, n/a, 2\%, 1\%, 2\%, 3\%) \quad (104)$$

relative to the fiducial  $\pi$ . The exception is  $\Omega_\Lambda$  which we set to  $\Omega_\Lambda = 1 - \Omega_m$  in all realisations (a fixed  $K = 0$  geometry). These errors are on the optimistic side but consistent with constraints from combined cosmological probes. In addition for each set of parameters, we plot data points for three different transfer functions of  $P_m(k; \chi)$ : Bardeen et al. (1986), and Eisenstein & Hu (1998) with and without BAOs. These are combined with two different Halofit models of the non-linear power spectrum: Smith et al. (2003) and the more accurate Takahashi et al. (2012). By these variations we mean to broadly account for model uncertainties in the non-linear power spectrum which produces extra scatter in

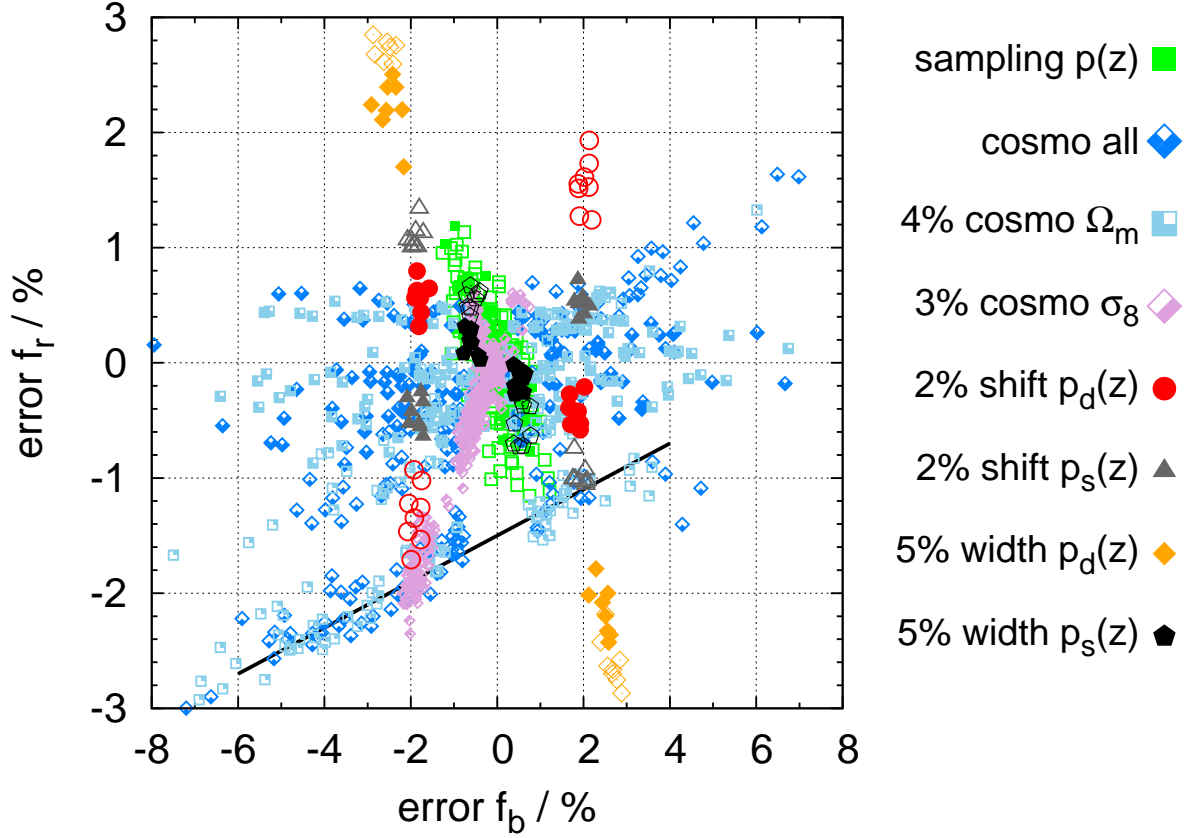


**Fig. 9.** Average error in the galaxy-bias normalisation  $f_b$  (x-axis) and  $f_r$  (y-axis). The points show indistinguishable the errors of all galaxy samples SM1-4, BLUE, and RED together; the point styles indicate the redshift bin and what is varied. Symbols as in the figure key indicate the low- $z$  samples, inverted symbols indicate the high- $z$  samples (e.g. solid and open circles). The ‘cosmo’ and ‘sampling  $p(z)$ ’ data points reuse the same galaxy samples many times with random normalisation errors. The solid line marks the estimated error for high- $z$  samples due to the baryon uncertainty. The fiducial cosmology is WMAP9. See text for more details.

the plot. In particular, the 10-20% difference between the two versions of Halofit in the regime  $k \gtrsim 1 h \text{ Mpc}^{-1}$  accounts to some extent for the theoretical uncertainty of baryons on the small-scale power spectrum (e.g. Springel et al. 2017; Foreman et al. 2016; Harnois-Déraps et al. 2015; Semboloni et al. 2011). We find that errors in the cosmological parameters or the non-linear power spectrum mainly affect the normalisation of  $b(k)$  which can be off by about 3.0% (68% confidence level, CL hereafter). The error in  $r(k)$  is within 1.1% (68% CL) for high- $z$  or smaller 0.4% (68% CL) for the low- $z$  samples (solid symbols). The straight line inside the figure indicates the locus of errors for the high- $z$  samples that are produced by the baryon uncertainty in the non-linear power spectrum.

- For ‘cosmo  $\Omega_m$ ’, we only vary  $\Omega_m$  in the cosmological parameters with the foregoing dispersion. This results in a distribution of data points that is very similar to ‘cosmo all’. For comparison, ‘cosmo  $\sigma_8$ ’ varies only  $\sigma_8$ . The scatter is now restricted to a small region. Therefore, the normalisation error owing to cosmological parameters is mainly explained by the variations in  $\Omega_m$ .
- For the data points ‘sampling  $p(z)$ ’, we add random shot noise to the redshift distributions. The idea here is that redshift distributions are estimated from a sub-sample of galaxies which gives rise to sampling noise in the estimated dis-

tributions used for normalisation; see e.g. Hildebrandt et al. (2017) which use a weighted sample of spectroscopic redshifts to model the redshift PDF of the full galaxy sample. To emulate the sampling shot-noise, we randomly draw  $n$  redshifts  $z \sim p(z)$  from the true  $p(z)$  to build a finely binned histogram of a noisy redshift distribution ( $\Delta z = 0.015$ ). We then employ this histogram for  $f'_b$  and  $f'_r$ . As fiducial values for our 1024 deg<sup>2</sup> survey, we adopt  $n = 10^4$  for the lenses and  $n = 10^5$  for the sources. These fiducial values imply that we estimate  $p(z)$  from spectroscopic redshifts of  $\sim 0.5\%$  of the sources and roughly 1%, 2%, 20%, 1% of the lenses in the samples SM1, SM4, SM6, RED/BLUE, respectively. The result is a similar scatter for the low- $z$  and the high- $z$  samples in Fig.1. The error is typically within 0.5% for  $b(k)$  and  $r(k)$  (68% CL).

- The data points ‘shift  $p_d(z)$ ’ vary the mean in the lens redshift distribution. For this, we systematically shift  $z \mapsto z(1 + \delta_z)$  by  $\delta_z = \pm 2\%$ , which is twice as large as the typical error on the mean redshift reported in Hildebrandt et al. (2017). The impact differs for the low- $z$  (solid circles) and the high- $z$  samples (open circles). For systematically higher redshifts in low- $z$ , this means  $\delta_z > 0$ ,  $b(k)$  is too large and  $r(k)$  is too low. For high- $z$  and  $\delta_z > 0$ , we find that both  $b(k)$  and  $r(k)$  are too high in amplitude. For  $\delta_z < 0$ , the effects are exactly reversed. The overall systematic normalisation error is nev-



ertheless not greater than typically 2% for  $b(k)$  and 1 – 2% for  $r(k)$ .

- The data points ‘width  $p_d(z)$ ’ vary the width of the lens redshift distribution. This we emulate by mapping  $p_d(z) \mapsto p_d(z)^{1/(1-\delta_\sigma)}$  to a new PDF that is then used for the normalisation. For a Gaussian density  $p_d(z)$ , this maps the dispersion to  $\sigma \mapsto \sigma(1-\delta_\sigma)$  while leaving the mean and Gaussian shape in the new PDF unchanged. For skewed distributions,  $\delta_\sigma \neq 0$  also moves the mean of the PDF. To account for this unwanted (small) side effect, we shift every PDF to assure that it retains its original mean redshift. We consider  $\delta_\sigma = \pm 5\%$  here. The effect of squeezing, this means  $\delta_\sigma > 0$ , is similar for low- $z$  and high- $z$ :  $b(k)$  is too low,  $r(k)$  is too high, with errors of around 2 – 3% for  $b(k)$  and  $r(k)$ . A stretching,  $\delta_\sigma < 0$ , has the reverse effect on both redshift bins.
- The data points ‘shift  $p_s(z)$ ’ and ‘width  $p_s(z)$ ’ explore the effect of errors in the mean or width of the source  $p_s(z)$ . Shifting by  $\delta_z = +2\%$  produces too high  $b(k)$  for low- $z$  and high- $z$  (1.9%), too high  $r(k)$  for low- $z$  (0.5%), and a too low  $r(k)$  for high- $z$  (1.0%). The reverse behaviour is present for systematically lower redshifts with  $\delta_z = -2\%$ . Changes in the width of the distribution with  $\delta_\sigma = \pm 5\%$  have a 0.5% effect for  $b(k)$  and  $r(k)$ , with low- $z$  samples being slightly less affected: a systematically wider distribution gives a too low  $b(k)$  and a too high  $r(k)$ ; the reverse effects apply for systematically narrower distributions, that is for  $\delta_\sigma > 0$ .
- The intrinsic alignment of sources contributes to both  $\langle M_{\text{ap}}^2 \rangle$  and  $\langle NM_{\text{ap}} \rangle$  and thereby can have an impact on  $b_{2D}$  and  $r_{2D}$ . We account for this in the normalisation by II and GI models; see Sect. 3.3. If unaccounted for, as assumed here, we bias  $b_{2D}$  by the error in  $\langle M_{\text{ap}}^2 \rangle_{\text{th}}^{1/2}$  that is used in the normalisation  $f_b$ , Eq. (16). This error is plotted in Fig. 10 for varying values of  $A_{\text{ia}}$  and angular scales  $\theta_{\text{ap}}$ . The normalisation error in  $r_{2D}$  is determined by error in  $\langle NM_{\text{ap}} \rangle_{\text{th}}^{-1} \langle M_{\text{ap}}^2 \rangle_{\text{th}}^{1/2}$  used for  $f_r$ , Eq. (17), which is plotted in Fig. 11 for SM4 high- $z$  as example; the errors of other high- $z$  samples are comparable. For the low- $z$  samples, the overlap of lens and source redshifts is small so that the error in  $\langle NM_{\text{ap}} \rangle_{\text{th}}^{-1}$  is negligible compared to the error in  $\langle M_{\text{ap}}^2 \rangle_{\text{th}}^{1/2}$ . Therefore, the normalisation error for  $r_{2D}$  in low- $z$  samples is approximately that of  $b_{2D}$  in Fig. 10. For  $|A_{\text{ia}}| \lesssim 2$ , the normalisation error of  $b_{2D}$  and  $r_{2D}$  is typically within  $\pm 5\%$  at scales  $\theta_{\text{ap}} \gtrsim 1'$ .

A summary of normalisation errors and their estimated magnitude is listed in Table 4. We find that the response to errors in the redshift distributions is approximately linear for  $\delta_z$  and  $\delta_\sigma$  that are within several per cent so that the quoted values could be scaled.

#### 7.4. Shear bias and reduced shear

As another source of systematic error, we consider a residual bias in the shear estimators that has not properly corrected for in the lensing pipeline. Following Kitching et al. (2012) (K+12 hereafter), we quantify a shear bias by  $\langle \gamma \rangle = (1 + m)\gamma + c$  for average estimated shear  $\langle \gamma \rangle$  in an ensemble of sources that are subject to the same  $\gamma$ :  $m$  is the so-called multiplicative bias and  $c$  is the additive bias. For a crude estimate of the impact of  $m$  on the measurement of  $b_{2D}(\theta_{\text{ap}})$  and  $r_{2D}(\theta_{\text{ap}})$ , we assume a constant and real-valued  $m$ . A value of  $m \neq 0$  produces a bias of  $1 + m$  in the measured aperture statistics  $\langle M_{\text{ap}}^2 \rangle^{1/2}$  and  $\langle NM_{\text{ap}} \rangle$ . Therefore, applying our methodology while ignoring  $m$  will scale the amplitude of  $b(k)$ , Eq. (14), by  $(1 + m)^{-1} = 1 - m + O(m^2)$  but

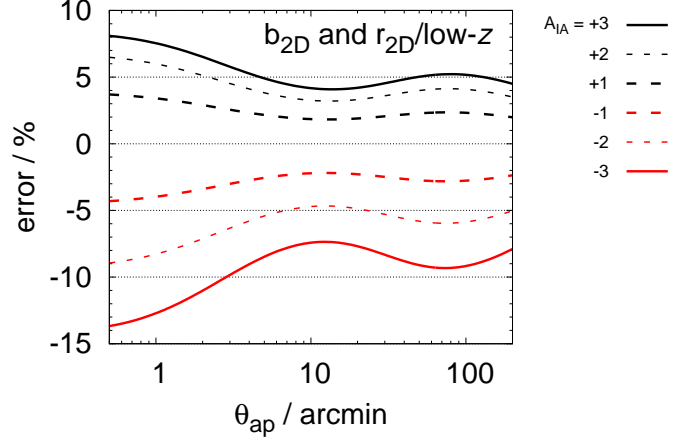


**Fig. 10.** Systematic relative errors in  $b_{2D}(\theta_{\text{ap}})$  (low- $z$  and high- $z$ ) and  $r_{2D}(\theta_{\text{ap}})$  (only low- $z$ ) when II and GI terms are ignored in the normalisation of the galaxy bias. Different lines show predictions for different values of  $A_{\text{ia}}$  with sources as in our mock survey. The fiducial cosmology is WMAP9.

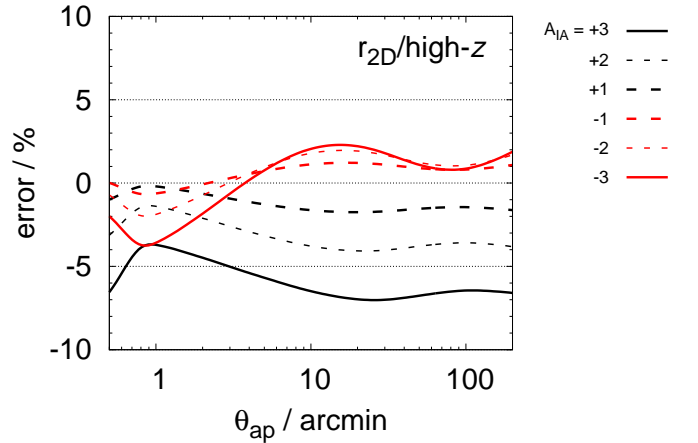


**Fig. 11.** As in Fig. 10 but now for  $r_{2D}(\theta_{\text{ap}})$  high- $z$ . Shown are results from SM4 but the values are similar for the other samples.

it will not change  $r(k)$  in Eq. (15). Contemporary lensing techniques reach a typical accuracy of  $|m| \approx 1\%$ , therefore we expect a similarly small systematic error for  $b(k)$  (K+12).

A residual additive bias  $c$  does not affect the aperture statistics if it is constant. If, on the other hand,  $c$  varies at a scale within the sensitive  $\ell$ -range of the aperture filter, we could have significant contributions to the measured  $\langle M_{\text{ap}}^2 \rangle$ , depending on the power of the  $c$ -fluctuations. Our polynomial filter in Eq. (12) has its maximum sensitivity for the angular wave number  $\ell_c \approx 4.25/\theta_{\text{ap}} \approx 1.5 \times 10^4 (\theta_{\text{ap}}/1')^{-1}$  or angular scale  $\theta_c = 2\pi/\ell_c \approx 1.44 \theta_{\text{ap}}$  (van Waerbeke 1998). The typical residual amplitudes of  $c$  after a calibration correction of  $\xi_{\pm}$  are of the order of  $10^{-5}$  (K+12; Appendix D4 in Hildebrandt et al. 2017) so that systematic errors owing to  $c$  fluctuations are probably below a per cent for  $\langle M_{\text{ap}}^2 \rangle^{1/2} \gtrsim 10^{-3}$ , which is the case for  $\theta_{\text{ap}} \lesssim 2$  deg and typical sources with  $z_s \approx 1$ ; see the data points in Fig. 2. The

statistic  $\langle NM_{\text{ap}} \rangle$  is not affected by the additive shear bias in the likely absence of correlations between lens positions and fluctuations of  $c$ , or is presumably corrected for by subtracting the correlation between random lens positions and shear in the data; see the estimator in Eq. (B.3).

With regard to reduced shear, our analysis assumes that the  $\epsilon_i$  are estimates of shear  $\gamma(\theta_i)$ , whereas they are in reality estimates of the reduced shear  $g_i = \gamma_i/(1 - \kappa_i)$ . While  $\langle \epsilon_i \rangle = \gamma_i$  is a good approximation for weak gravitational-lensing and substantially simplifies the formalism in Sect. 3, we will have some systematic error. To quantify this error, we redo the reconstruction of the biasing functions for a new shear catalogue where the intrinsic source ellipticities are sheared by  $g_i$  rather than  $\gamma_i$ ; source positions and intrinsic shapes do not match between the old and new catalogues. For the new catalogues, we obtain a set of values  $\sigma_f^{\text{red}}$ , Eq. (100), which we statistically compare to the previous values  $\sigma_f$  in Table 3 by fitting an average parameter  $\delta_{\text{red}}$  for the relative difference, defined by  $\sigma_f^{\text{red}} = (1 + \delta_{\text{red}}) \sigma_f$ , to all samples and redshift bins. For all values of  $\sigma_b$  and  $\sigma_r$  combined, we find no significant differences between the new and old shear catalogues, this means  $\delta_{\text{red}}$  is consistent with zero; the upper limit is  $\delta_{\text{red}} \lesssim 13\%$  (68% CL). For an average of  $\langle \sigma_f \rangle = 3.8\%$ , the additional inaccuracy due to reduced shear is therefore less than  $13\% \times \langle \sigma_f \rangle \approx 0.5\%$ .

### 7.5. Garching-Bonn Deep Survey

Finally, we apply our procedure in a first demonstration to data in the GaBoDS (Simon et al. 2007, SHS07 hereafter; Hettetscheidt et al. 2007). Because of its comparatively small effective survey area of roughly 15 square degree, the statistical power of GaBoDS is no longer competitive to measurements in contemporary surveys. Nevertheless, the results presented here shed some new light on the nature of the lens galaxies in SHS07 and round off the past GaBoDS analysis. We plan to apply our methodology to more recent lensing data in an upcoming paper.

As lens sample in GaBoDS we choose FORE-I galaxies, which comprise  $R \leq 21.0$  flux-limited galaxies with mean redshift  $\bar{z}_d = 0.35$ ; the RMS dispersion of the lens redshifts is 0.16. The source galaxies are flux-selected between  $21.5 \leq R \leq 24.0$  and have  $\bar{z}_s = 0.68$ ; see Figure 3 in SHS07 for the redshift distributions of lenses and sources in these samples. For the estimators, we bin the two-point correlation functions (B.2)-(B.4) between 7 arcsec and 46 arcmin using 4100 linear bins and merge the catalogues of the  $n_{\text{patch}} = 52$  GaBoDS fields also used in SHS07. In contrast to SHS07, we only use six aperture scales between 2 and 23 arcmin, equidistant on a logarithmic scale, because of the strong correlation of errors between similar aperture scales. The correlation matrix of statistical (jackknife) errors can be found in Fig. 12. Furthermore, we normalise the new measurements by a WMAP9 cosmology, Eq. (103). In contrast to the foregoing analyses with our mock MS data, for which we measure the aperture statistics up to degree scales, we here have to use Eq. (69) to extrapolate the large-scale bias  $b_{\text{ls}}$ , which is then no longer a free parameter. For the halo bias-factor  $b_h(m)$ , needed in this extrapolation, we employ the fitting formula in Tinker et al. (2005). Owing to lacking information on an IA of GaBoDS sources, we do assume  $A_{\text{ia}} = 0$ . A value of  $|A_{\text{ia}}| \lesssim 2$  could therefore shift the amplitude of  $b_{2D}$  by up to 10 to 15 per cent, mainly because of the GI term, and that of  $r_{2D}$  by up to 2 per cent.

Our updated measurements are shown in the left panel of Fig. 13 as  $b_{2D}$  and  $r_{2D}$  by the black data points designated SHS+07. To obtain these points from the observed aperture-moment statis-

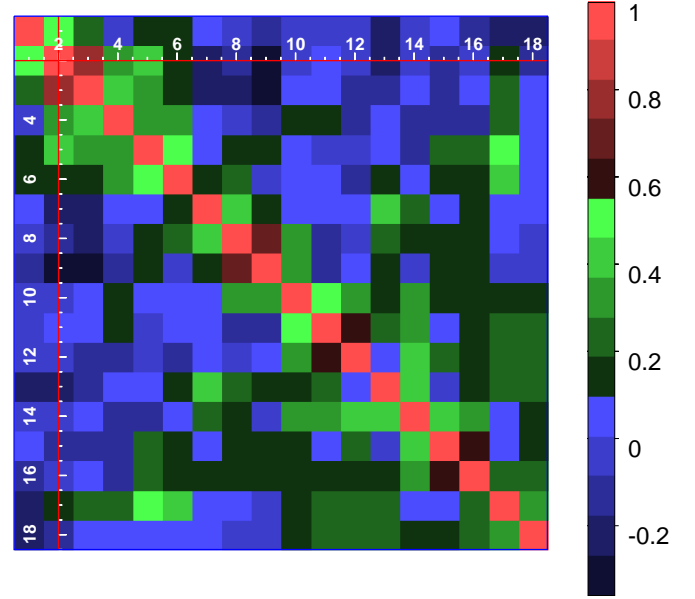


**Fig. 12.** Correlation matrix  $C_{ij}$  of measurements errors for three kinds of aperture statistics of FORE-I lenses in the GaBoDS analysis. The integers on the two axes inside the matrix refer to either the  $i$  or  $j$  index. Values  $1 \leq k \leq 6$  for  $k$  being either  $i$  or  $j$  refer to errors of  $\langle N^2(\theta_k) \rangle$ , values of  $7 \leq k \leq 12$  to  $\langle NM_{\text{ap}}(\theta_{k-6}) \rangle$ , and values  $13 \leq k \leq 18$  to  $\langle M_{\text{ap}}^2(\theta_{k-12}) \rangle$ . The aperture scales  $\{\theta_k/\text{arcmin}\}$  are  $\{2, 3.3, 5.3, 8.7, 14.1, 23\}$ . The matrix is estimated from 52 jackknife samples.

tics, we randomly draw realisations of the aperture statistics from a Gaussian likelihood based on our jackknife data covariance. The open squares show the median and 68 percentiles of the normalised bias parameters from this Monte-Carlo process, computed with Eqs. (14) and (15) for each realisation; the open circles are the mean of the realisations which are different to the median owing to the skewness in the error distribution. The shaded regions indicate the 68% and 95% PI of the posterior (projected) biasing functions. The red stars are measurements in VIRMOS/DESCART, broadly consistent with ours, for flux-limited galaxies with a similar selection function (Hoekstra et al. 2002).

The right panel of Fig. 13 depicts the posterior of the template parameters that provide a physical interpretation of the galaxy bias. We take from here that the scale-dependence of the galaxy bias mainly originates in a scale-dependence of  $b(m)$ : between halo masses of  $10^{13}$  to  $10^{14} h^{-1} M_{\odot}$  there is a relative scarcity of galaxies, which is qualitatively comparable to the BLUE low- $z$  sample (see Fig. D.1). The HOD variance is consistent with a Poisson model, that means  $V(m) = 0$ , albeit only weakly constrained. The 68% PI of the pivotal halo mass is  $m_{\text{piv}} = 10^{11.48+0.72-0.81} h^{-1} M_{\odot}$ , and the fraction  $f_{\text{cen}} = 0.50 \pm 0.31$  of halos open for central galaxies is essentially the uniform prior which has the variance  $1/\sqrt{12}$  and the mean 0.5. The posterior galaxy number density is  $\bar{n}_g = 0.19^{+0.33}_{-0.13} h^3 \text{Mpc}^{-3}$ .

Fig. 14 displays the posterior distribution of the deprojected biasing functions and the 68% PI for FORE-I galaxies. The biasing functions are an average for the redshift range covered by the lens galaxies. The GaBoDS data probe primarily the one-halo regime  $\theta_{\text{ap}} \lesssim 20$  arcmin; the large-scale bias of  $b_{\text{ls}} = 0.92^{+0.04}_{-0.03}$  visible at  $k \ll 1 h \text{Mpc}^{-1}$  is extrapolated. The red data points

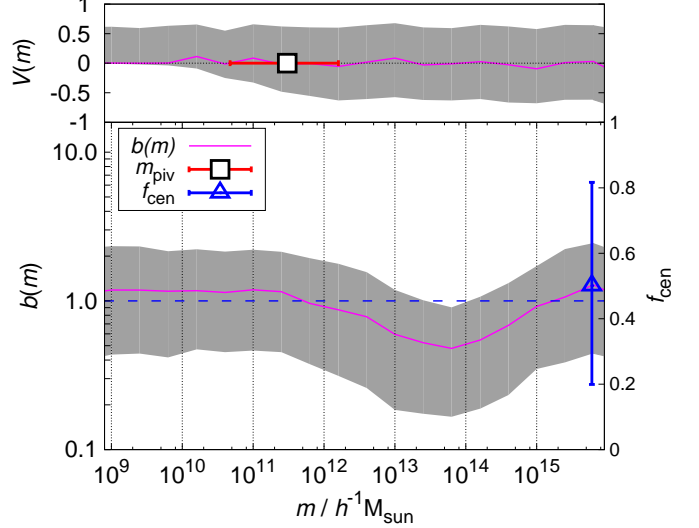
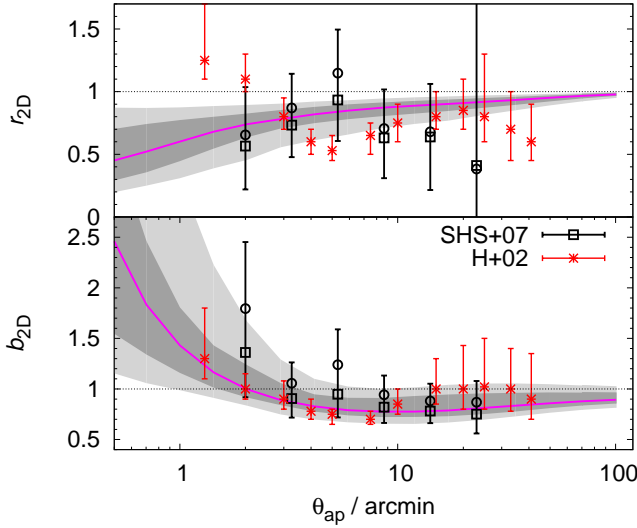


**Fig. 13.** *Left:* Posterior model of  $r_{2D}(\theta_{ap})$  (top) and  $b_{2D}(\theta_{ap})$  (bottom) based on the GaBoDS measurements FORE-I (shaded regions with 68% and 95% PI). Shown as black open squares are the median values and a 68% interval around the median for the measured  $b_{2D}$  and  $r_{2D}$ ; the open circles indicate the mean. The red-star data points H+02 show the measurements by Hoekstra et al. (2002) for comparison. *Right:* 68% PI posterior of the excess HOD variance  $V(m)$  with open box for the mass scale of the pivotal mass  $m_{piv}$  (top); 68% PI posterior of the mean biasing function  $b(m)$  and  $f_{cen}$  as open triangle (bottom). The fiducial model has WMAP9 parameters.

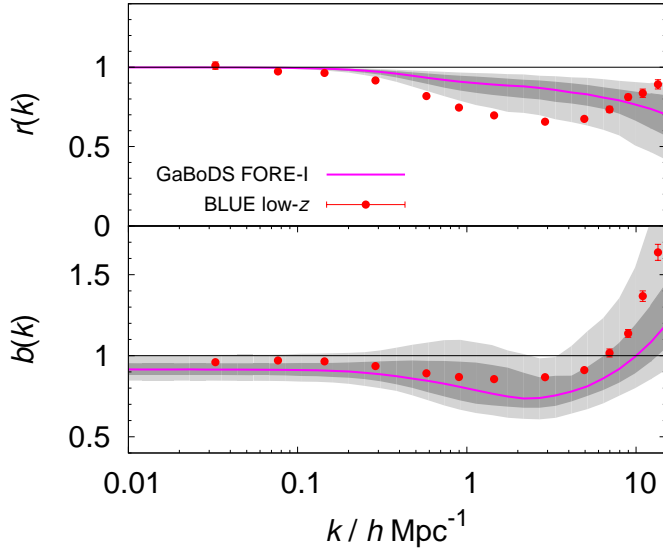


**Fig. 14.** Reconstructed biasing functions of FORE-I galaxies in GaBoDS. Shown are the 68% and 95% PI of  $b(k)$  in the bottom panel and that of  $r(k)$  in the top panel. The biasing function are an average over the redshift range  $0.34 \pm 0.16$  for a WMAP9 cosmology. The red data points show the biasing function of BLUE low- $z$ , which have a similar  $b(m)$ .

show the biasing functions of BLUE low- $z$  for a qualitative comparison.

## 8. Discussion

In this study, we have outlined and successfully tested a refined technique to measure in contemporary lensing surveys the scale-dependent galaxy bias down to non-linear scales of

$k \sim 10 h^{-1} \text{Mpc}$  for lens galaxies at  $z \lesssim 0.6$ . To test our reconstruction technique, we employ a fiducial survey with a sky coverage of  $\sim 1000 \text{deg}^2$ , and a photometry and a survey depth as in CFHTLenS. To construct realistic samples of lenses and sources, we have prepared mock catalogues that are consistent with those used in SES13 and Saghiha et al. (2017). Despite some variations in survey depth and area, these survey parameters are similar to the ongoing Kilo-Degree Survey (KiDS), Dark Energy Survey (DES), or the survey with the Hyper Suprime-Cam (Kuijken et al. 2015; Becker et al. 2016; Aihara et al. 2017). If the galaxy-bias normalisation is perfect, our technique applied to these data can achieve a statistical precision within the range of 5 – 10% (68% CL), if similar lens and source samples are targeted, and a slightly better accuracy of 3 – 7% (68% CL), see Table 3. For the high- $z$  samples, the accuracy will be somewhat higher with 3 – 5%. On the other hand, it is clear from our overview Table 4 that the accuracy of the galaxy-bias normalisation is in fact limited, mainly by our knowledge of the intrinsic alignment of sources, cosmological parameters, and the galaxy redshift-distributions. With a broad knowledge of  $|A_{ia}| \lesssim 2$  and the specifications for the normalisation errors in Table 4, we conclude that systematic errors would potentially degrade the overall accuracy to approximately 15% for  $b(k)$  and 10% for  $r(k)$ . For fully controlled intrinsic alignment of sources, these errors could be reduced by 5%. An additional reduction by 3% may be possible by controlling the redshift distributions (their mean and variance) in the normalisation to 1% accuracy. For the fiducial cosmology, the knowledge of  $\Omega_m$  is of most importance while the normalisation of the ratio statistics is less affected by  $\sigma_8$ .

For a future method improvement, various problems could be of interest: (i) approximations in the formalism or estimators of Sect. 3; (ii) an inaccurate statistical model for the likelihood function; (iii) a model bias in the templates. We discuss a few problems in the following. With regard to our statistical model, we find indeed evidence for deviations from a Gaussian model of the joint aperture statistics which is explicitly assumed in Eq. (91) (see Appendix C). However, the magnitude of a bias owing to a Gaussian model is not clear and requires more re-

search. For example, deviations from a Gaussian distribution in broadly related cosmological analyses with the aperture mass  $M_{\text{ap}}$  are reported in Simon et al. (2015) and Hartlap et al. (2009) where non-Gaussian corrections to the likelihood produce insignificant changes in one case but not in the other. Interestingly for our data, the most inaccurate reconstruction (for small  $k$ ) is that of RED low- $z$  which shows a strong indication of a non-Gaussian error-distribution for  $\langle N^2 \rangle$  at large angular scales; see Table B.1. Moreover, our likelihood model employs an error covariance that we estimate by the jackknife technique. The jackknife technique is known to underestimate cosmic variance, in particular for angular scales comparable to the size of sub-fields used for the jackknife sample (Friedrich et al. 2016). However, this problem is partly addressed in our analysis by using ratio statistics which is less affected by cosmic variance (Bernstein & Cai 2011). While this may not be sufficient for future surveys, it seems to be so for contemporary surveys because cosmic variance is included in our assessment of the reconstruction accuracy. Finally, a model bias in our templates for  $b(k)$  and  $r(k)$  is arguably unlikely, at least for our simulated galaxy samples, because the purely generic models in Eq. (102) do not produce a more accurate reconstruction of the biasing functions although they are excellent fits to the true biasing functions (see Table 3). Nevertheless, a relevant model bias could arise through our assumption of a non-evolving galaxy bias for galaxy samples with a distance distribution that is broad compared to the galaxy-bias evolution.

Our physical templates for the biasing functions  $b(k)$  and  $r(k)$  are also insightful for a basic physical interpretation of the scale-dependence of galaxy bias. On the one hand, the physical parameters in the physical templates describe the HOD of the actual galaxy population. On the other hand, these HOD parameters have only a moderate accuracy because our relatively simple halo model lacks the implementation of recently identified effects such as halo exclusion, non-linear or stochastic halo clustering, assembly bias, galaxy conformity, or a scale-dependent halo-bias function (Baldauf et al. 2013; Gao & White 2007; Kauffmann et al. 2013; Tinker et al. 2005). And our model has a comparably simplistic treatment of central galaxies. According to Cacciato et al. (2012), by taking ratios of the aperture statistics we are, however, probably less sensitive to these shortfalls in the halo model. We therefore expect the HOD parameters in our templates not to be more accurate than 10 – 20% compared to the true HOD in the lens sample, based on the reported biases in the cited literature. We stress that this does not necessarily pose a problem for the deprojection as long as the templates are good fits to the true biasing functions. With regard to a basic interpretation of galaxy bias, we nevertheless take from the discussion in Sect. 5.3 that central galaxies and a non-Poisson HOD variance produce a scale-dependent bias most prominently towards small scales, namely in the regime that is dominated by low-occupancy halos with  $m \lesssim m_{\text{piv}}$ . A strong scale-dependence over a wider range of spatial or angular scales and a non-monotonic behaviour may be produced by a mean biasing function  $b(m)$  that varies with halo mass  $m$ ; in particular only  $b(m)$  affects the large-scale bias. Interestingly here, the effect of central galaxies is different from that of a non-Poisson variance: central galaxies increase both  $b(k)$  and  $r(k)$  for larger  $k$ , whereas a non-Poisson variance induces opposite trends for  $b(k)$  and  $r(k)$ . Therefore, the measurement of biasing functions can in principle constrain both  $b(m)$  and the excess variance  $V(m)$  to test galaxy models, although predictably with limited accuracy in contemporary surveys (see Fig. D.2).

A demonstration of our reconstruction technique to data in the GaBoDS suggests that the  $R \leq 21$  flux-limited sample of lens galaxies FORE-I consists mainly of blue galaxies in the field. Fig. 14 reports our reconstruction of the biasing functions for the FORE-I sample in Simon et al. (2007). The physical parameters in the right panel of Fig. 13 show that these galaxies tend to avoid halos in the broad mass-range  $10^{13} - 10^{14} h^{-1} M_{\odot}$  and thereby produce the relatively low (mean) values of  $b_{2D} \approx 0.8$  and  $r_{2D} \approx 0.6$  and their scale-dependence between a few and 20 arcmin (left panel); see also the measurements by H+02 for similar lens galaxies with comparable results. Consequently, they are presumably in majority field and group galaxies. The reconstructed biasing functions also broadly match those of BLUE low- $z$  which supports this interpretation. Clearly, the BLUE low- $z$  sample does not have the same selection function as FORE-I so that this comparison is certainly only qualitative. For a quantitative test of galaxy models with more recent galaxy surveys, simulated and observed galaxies have to be carefully selected to obtain consistent samples. If this succeeds, both our little demonstration with the  $15 \text{ deg}^2$  GaBoDS data and the multiplicity of biasing functions visible in the Figs. 7 and 8 promise useful constraints for galaxy models.

## Acknowledgements

We thank Hananeh Saghiha for preparing the RED and BLUE galaxy samples. We also thank Catherine Heymans and Indiarose Friswell for comments on the shear bias, and Peter Schneider for general comments on the paper. This work has been supported by Collaborative Research Center TR33 ‘The Dark Universe’ and by the Deutsche Forschungsgemeinschaft through the project SI 1769/1-1. Patrick Simon also acknowledges support from the German Federal Ministry for Economic Affairs and Energy (BMWi) provided via DLR under project no. 50QE1103. Stefan Hilbert acknowledges support by the DFG cluster of excellence ‘Origin and Structure of the Universe’ ([www.universe-cluster.de](http://www.universe-cluster.de)).

## References

- Abbott, T., Abdalla, F. B., Allam, S., et al. 2016, *Phys. Rev. D*, 94, 022001
- Aihara, H., Arimoto, N., Armstrong, R., et al. 2017, *arXiv:1704.05858*
- Baldauf, T., Seljak, U., Smith, R. E., Hamaus, N., & Desjacques, V. 2013, *Phys. Rev. D*, 88, 083507
- Baldauf, T., Smith, R. E., Seljak, U., & Mandelbaum, R. 2010, *Phys. Rev. D*, 81, 063531
- Bardeen, J. M., Bond, J. R., Kaiser, N., & Szalay, A. S. 1986, *ApJ*, 304, 15
- Bartelmann, M. & Schneider, P. 2001, *Phys. Rep.*, 340, 291
- Becker, M. R., Troxel, M. A., MacCrann, N., et al. 2016, *Phys. Rev. D*, 94, 022002
- Benson, A. J., Cole, S., Frenk, C. S., Baugh, C. M., & Lacey, C. G. 2000, *MNRAS*, 311, 793
- Bernstein, G. M. & Cai, Y.-C. 2011, *MNRAS*, 416, 3009
- Bertone, G., Hooper, D., & Silk, J. 2005, *Phys. Rep.*, 405, 279
- Bridle, S. & King, L. 2007, *New Journal of Physics*, 9, 444
- Buddendiek, A., Schneider, P., Hildebrandt, H., et al. 2016, *MNRAS*, 456, 3886
- Bullock, J. S., Kolatt, T. S., Sigad, Y., et al. 2001, *MNRAS*, 321, 559
- Cacciato, M., Lahav, O., van den Bosch, F. C., Hoekstra, H., & Dekel, A. 2012, *MNRAS*, 426, 566
- Chang, C., Pujol, A., Gaztañaga, E., et al. 2016, *MNRAS*, 459, 3203
- Clowe, D., Gonzalez, A., & Markevitch, M. 2004, *ApJ*, 604, 596
- Cole, S., Percival, W. J., Peacock, J. A., et al. 2005, *MNRAS*, 362, 505
- Comparat, J., Jullo, E., Kneib, J.-P., et al. 2013, *MNRAS*, 433, 1146
- Conselice, C. J., Wilkinson, A., Duncan, K., & Mortlock, A. 2016, *ApJ*, 830, 83
- Cooray, A. & Sheth, R. 2002, *Phys. Rep.*, 372, 1
- Dekel, A. & Lahav, O. 1999, *ApJ*, 520, 24
- Desjacques, V., Jeong, D., & Schmidt, F. 2016, *arXiv:1611.09787*
- Dodelson, S. 2003, *Modern cosmology*

- Einstein, A. 1917, Sitzungsberichte der Königlich Preußischen Akademie der Wissenschaften (Berlin), Seite 142-152.
- Eisenstein, D. J. & Hu, W. 1998, *ApJ*, 496, 605
- Erben, T., Hildebrandt, H., Miller, L., et al. 2013, *MNRAS*, 433, 2545
- Foreman, S., Becker, M. R., & Wechsler, R. H. 2016, *MNRAS*, 463, 3326
- Friedrich, O., Seitz, S., Eifler, T. F., & Gruen, D. 2016, *MNRAS*, 456, 2662
- Gao, L. & White, S. D. M. 2007, *MNRAS*, 377, L5
- Gelman, A., Carlin, J., Stern, H., & Rubin, D. 2003, *Bayesian Data Analysis*, Second Edition, Chapman & Hall/CRC Texts in Statistical Science (Taylor & Francis)
- Guzik, J. & Seljak, U. 2001, *MNRAS*, 321, 439
- Harnois-Déraps, J., van Waerbeke, L., Viola, M., & Heymans, C. 2015, *MNRAS*, 450, 1212
- Hartlap, J. 2009, PhD thesis, AIfA - Argelander-Institut für Astronomie, Rheinische Friedrich-Wilhelms Universität Bonn, Germany, <http://hss.ulb.uni-bonn.de/2009/1796/1796.htm>
- Hartlap, J., Schrabback, T., Simon, P., & Schneider, P. 2009, *A&A*, 504, 689
- Hartlap, J., Simon, P., & Schneider, P. 2007, *A&A*, 464, 399
- Henriques, B. M. B., White, S. D. M., Thomas, P. A., et al. 2015, *MNRAS*, 451, 2663
- Hetterscheidt, M., Simon, P., Schirmer, M., et al. 2007, *A&A*, 468, 859
- Heymans, C., Grocutt, E., Heavens, A., et al. 2013, *MNRAS*, 432, 2433
- Heymans, C., Van Waerbeke, L., Miller, L., et al. 2012, *MNRAS*, 427, 146
- Hilbert, S., Hartlap, J., White, S. D. M., & Schneider, P. 2009, *A&A*, 499, 31
- Hildebrandt, H., Erben, T., Kuijken, K., et al. 2012, *MNRAS*, 421, 2355
- Hildebrandt, H., van Waerbeke, L., Scott, D., et al. 2013, *MNRAS*, 429, 3230
- Hildebrandt, H., Viola, M., Heymans, C., et al. 2017, *MNRAS*, 465, 1454
- Hinshaw, G., Larson, D., Komatsu, E., et al. 2013, *ApJS*, 208, 19
- Hirata, C. M. & Seljak, U. 2004, *Phys. Rev. D*, 70, 063526
- Hockney, R. W. & Eastwood, J. W. 1981, *Computer Simulation Using Particles* (Computer Simulation Using Particles, New York: McGraw-Hill, 1981)
- Hoekstra, H., van Waerbeke, L., Gladders, M. D., Mellier, Y., & Yee, H. K. C. 2002, *ApJ*, 577, 604
- Hoekstra, H., Yee, H. K. C., & Gladders, M. D. 2001, *ApJ*, 558, L11
- Jing, Y. P. 2005, *ApJ*, 620, 559
- Joachimi, B., Mandelbaum, R., Abdalla, F. B., & Bridle, S. L. 2011, *A&A*, 527, A26
- Joudaki, S., Blake, C., Johnson, A., et al. 2017, *arXiv:1707.06627*
- Jullo, E., Rhodes, J., Kiessling, A., et al. 2012, *ApJ*, 750, 37
- Kaiser, N. 1984, *ApJ*, 284, L9
- Kauffmann, G., Li, C., Zhang, W., & Weinmann, S. 2013, *MNRAS*, 430, 1447
- Kilbinger, M. 2015, *Reports on Progress in Physics*, 78, 086901
- Kilbinger, M., Benabed, K., Guy, J., et al. 2009, *A&A*, 497, 677
- Kilbinger, M., Fu, L., Heymans, C., et al. 2013, *MNRAS*, 430, 2200
- Kilbinger, M., Heymans, C., Asgari, M., et al. 2017, *MNRAS*, 472, 2126
- Kilbinger, M., Schneider, P., & Eifler, T. 2006, *A&A*, 457, 15
- Kilbinger, M., Wraith, D., Robert, C. P., et al. 2010, *MNRAS*, 405, 2381
- Kirk, D., Brown, M. L., Hoekstra, H., et al. 2015, *Space Sci. Rev.*, 193, 139
- Kitching, T. D., Balan, S. T., Bridle, S., et al. 2012, *MNRAS*, 423, 3163
- Knight, K. 1999, *Mathematical Statistics*, Chapman & Hall/CRC Texts in Statistical Science (CRC Press)
- Kuijken, K., Heymans, C., Hildebrandt, H., et al. 2015, *MNRAS*, 454, 3500
- Landy, S. D. & Szalay, A. S. 1993, *ApJ*, 412, 64
- Loverde, M. & Afshordi, N. 2008, *Phys. Rev. D*, 78, 123506
- Mandelbaum, R., Hirata, C. M., Ishak, M., Seljak, U., & Brinkmann, J. 2006, *MNRAS*, 367, 611
- Martino, L. & Read, J. 2012, *arXiv:1201.0646*
- Mehta, K. T., Seo, H.-J., Eckel, J., et al. 2011, *ApJ*, 734, 94
- Mo, H., van den Bosch, F. C., & White, S. 2010, *Galaxy Formation and Evolution*
- Munshi, D., Valageas, P., van Waerbeke, L., & Heavens, A. 2008, *Phys. Rep.*, 462, 67
- Navarro, J. F., Frenk, C. S., & White, S. D. M. 1996, *ApJ*, 462, 563
- Peacock, J. A. & Smith, R. E. 2000, *MNRAS*, 318, 1144
- Peebles, P. J. E. 1980, *The large-scale structure of the universe* (Princeton University Press, USA)
- Pen, U.-L., Lu, T., van Waerbeke, L., & Mellier, Y. 2003, *MNRAS*, 346, 994
- Planck Collaboration, Ade, P. A. R., Aghanim, N., et al. 2016, *A&A*, 594, A13
- Prat, J., Sánchez, C., Miquel, R., et al. 2016, *arXiv:1609.08167*
- Pujol, A., Chang, C., Gaztañaga, E., et al. 2016, *MNRAS*, 462, 35
- Reyes, R., Mandelbaum, R., Seljak, U., et al. 2010, *Nature*, 464, 256
- Saghiha, H., Simon, P., Schneider, P., & Hilbert, S. 2017, *A&A*, 601, A98
- Schneider, P. 1998, *ApJ*, 498, 43
- Schneider, P., Kochanek, C., & Wambsganss, J. 2006, *Gravitational lensing: strong, weak and micro*, Saas-Fee Advanced Course: Swiss Society for Astrophysics and Astronomy (Springer)
- Schneider, P., van Waerbeke, L., Kilbinger, M., & Mellier, Y. 2002, *A&A*, 396, 1
- Seljak, U. 2000, *MNRAS*, 318, 203
- Sellentin, E. & Heavens, A. F. 2016, *MNRAS*, 456, L132
- Semboloni, E., Hoekstra, H., Schaye, J., van Daalen, M. P., & McCarthy, I. G. 2011, *MNRAS*, 417, 2020
- Sheth, R. K. & Tormen, G. 1999, *MNRAS*, 308, 119
- Simon, P. 2012, *A&A*, 543, A2
- Simon, P. 2013, *A&A*, 560, A33
- Simon, P., Erben, T., Schneider, P., et al. 2013, *MNRAS*, 430, 2476
- Simon, P., Hetterscheidt, M., Schirmer, M., et al. 2007, *A&A*, 461, 861
- Simon, P., Hetterscheidt, M., Wolf, C., et al. 2009, *MNRAS*, 398, 807
- Simon, P., Saghiha, H., Hilbert, S., Schneider, P., & Boever, C. 2017, *arXiv:1710.09902*
- Simon, P., Semboloni, E., van Waerbeke, L., et al. 2015, *MNRAS*, 449, 1505
- Singh, S., Mandelbaum, R., Seljak, U., Slosar, A., & Vazquez Gonzalez, J. 2016, *arXiv:1611.00752*
- Smith, R. E., Peacock, J. A., Jenkins, A., et al. 2003, *MNRAS*, 341, 1311
- Somerville, R. S., Lemson, G., Sigad, Y., et al. 2001, *MNRAS*, 320, 289
- Springel, V., Frenk, C. S., & White, S. D. M. 2006, *Nature*, 440, 1137
- Springel, V., Pakmor, R., Pillepich, A., et al. 2017, *arXiv:1707.03397*
- Springel, V., White, S. D. M., Jenkins, A., et al. 2005, *Nature*, 435, 629
- Takahashi, R., Sato, M., Nishimichi, T., Taruya, A., & Oguri, M. 2012, *ApJ*, 761, 152
- Tegmark, M. & Bromley, B. C. 1999, *ApJ*, 518, L69
- Tegmark, M. & Peebles, P. J. E. 1998, *ApJ*, 500, L79
- Tinker, J. L., Weinberg, D. H., Zheng, Z., & Zehavi, I. 2005, *ApJ*, 631, 41
- Troxel, M. A. & Ishak, M. 2015, *Phys. Rep.*, 558, 1
- van Uitert, E., Joachimi, B., Joudaki, S., et al. 2017, *arXiv:1706.05004*
- van Waerbeke, L. 1998, *A&A*, 334, 1
- Velander, M., van Uitert, E., Hoekstra, H., et al. 2014, *MNRAS*, 437, 2111
- Weinberg, D. H., Davé, R., Katz, N., & Hernquist, L. 2004, *ApJ*, 601, 1
- Ziour, R. & Hui, L. 2008, *Phys. Rev. D*, 78, 123517

## Appendix A: Impact of shot-noise subtraction on real-space biasing functions

Let the functions  $\xi_g(x) = \langle \delta_g(0)\delta_g(x) \rangle$ ,  $\xi_{mg}(x) = \langle \delta_g(0)\delta_m(x) \rangle$ , and  $\xi_m(x) = \langle \delta_m(0)\delta_m(x) \rangle$  be the correlation between density contrasts of galaxies and matter at lag  $x$ , and

$$b(x) = \sqrt{\frac{\xi_g(x)}{\xi_m(x)}}; \quad r(x) = \frac{\xi_{mg}(x)}{\sqrt{\xi_g(x)\xi_m(x)}} \quad (\text{A.1})$$

the biasing functions in real space. We show for two specific scenarios of the toy model in Sect. 4.3 that the subtraction of Poisson-shot noise can produce  $r(x) > 1$  for  $x > 0$ . To this end, we first work out the real-space biasing functions  $b(x)$  and  $r(x)$  for the toy model. The correlation function  $\xi(x)$  for a given power spectrum  $P(k)$  is

$$\xi(x) = [P](x) := \frac{1}{2\pi^2 x} \int_0^\infty dk \, k P(k) \sin(kx), \quad (\text{A.2})$$

where we have defined the integral operator  $[P](x)$  on the function  $P(k)$ . For our toy model, we hence find  $\xi_g(x) = [P_g](x)$ ,  $\xi_{gm}(x) = [P_{gm}](x)$ , and  $\xi_m(x) = [P_m](x)$  with the one-halo terms Eqs. (46)–(48) and  $n(m) \propto \delta_D(m - m_0)$ . We assume  $x > 0$  in the following. After some algebra, we find

$$b(x) = \frac{[\tilde{u}_m \cdot \tilde{u}_g^q](x)}{[\tilde{u}_m^2](x)} \frac{1}{r(x)}; \quad (\text{A.3})$$

$$r(x) = \frac{[\tilde{u}_m \cdot \tilde{u}_g^q](x)}{\sqrt{[\tilde{u}_m^2](x)[\tilde{u}_m^2](x)}} \left( 1 + \frac{\Delta\sigma_N^2(m_0)}{\langle N|m_0 \rangle} \right)^{-1/2}; \quad (\text{A.4})$$

where  $[\tilde{f} \cdot \tilde{g}](x)$  denotes the Fourier back-transform of the product  $\tilde{f}(k) \times \tilde{g}(k)$ ; it is hence the convolution of  $f(x)$  and  $g(x)$ . These equation assume  $u_m(x) \geq 0$  for all lags  $x$  such that the convolution  $[\tilde{u}_m^2](x) = [\tilde{u}_m \cdot \tilde{u}_m](x)$  is positive definite as well. Now, for



faithful galaxies we have  $\tilde{u}_m(k, m_0) = \tilde{u}_g(k, m_0)$  and  $p = q = 1$ , and therefore analogous to  $(b(k), r(k))$

$$b(x) \times r(x) = 1 ; r(x) = \left( 1 + \frac{\Delta\sigma_N^2(m_0)}{\langle N|m_0 \rangle} \right)^{-1/2}. \quad (\text{A.5})$$

Clearly, we find  $r(x) > 1$  for a sub-Poisson HOD variance also for real-space biasing functions. Moreover, for galaxies with  $\tilde{u}_m(k, m_0) = \tilde{u}_g(k, m_0)$ , Poisson HOD variance ( $\Delta\sigma_N^2 = 0$ ), and central galaxies in low-occupancy halos ( $p = 1/2, q = 0$ ), we arrive at

$$\frac{b(x)}{r(x)} = 1 ; r(x) = \sqrt{\frac{[\tilde{u}_m](x)}{[\tilde{u}_m^2](x)}}. \quad (\text{A.6})$$

Therefore, also here we find  $r(x) > 1$  for at least some lags  $x$  because the convolution of  $u_m(x)$  with itself has to be  $[\tilde{u}_m^2](x) < u_m(x)$  for some  $x$ .

## Appendix B: Estimators of aperture statistics

The aperture statistics can be obtained from three kinds of two-point correlation functions based on the positions  $\theta_i^d$  of  $n_d$  lens galaxies on the sky and the positions  $\theta_i^s$ , shear estimators  $\epsilon_i$ , and statistical weights  $w_i$  of  $n_s$  source galaxies. We estimate these correlation functions as follows.

First, we estimate the shear-shear correlation functions  $\xi_{\pm}(\vartheta) = \langle \gamma_t(\theta + \vartheta) \gamma_t(\theta) \rangle \pm \langle \gamma_{\times}(\theta + \vartheta) \gamma_{\times}(\theta) \rangle$  for a separation  $\vartheta$  of two sources, where the tangential,  $\gamma_t$ , and cross components,  $\gamma_{\times}$ , of  $\gamma$  at the source positions are defined relative to the vector  $\vartheta$  connecting a source pair through  $\gamma_t + i \gamma_{\times} = -\vartheta^* / \vartheta \gamma$ ; position or separation vectors use the usual complex-valued notation in a local Cartesian frame on the sky (Bartelmann & Schneider 2001). We define for all estimators a galaxy pair  $ij$  with positions  $\theta_i^s$  and  $\theta_j^s$  to be within the separation bin  $(\bar{\vartheta}, \Delta\vartheta)$  if  $\Delta_{ij}^{xy}(\bar{\vartheta}, \Delta\vartheta) \neq 0$  for

$$\Delta_{ij}^{xy}(\bar{\vartheta}, \Delta\vartheta) := \begin{cases} 1 & \text{if } \bar{\vartheta} - \Delta\vartheta/2 \leq |\theta_i^x - \theta_j^x| < \bar{\vartheta} + \Delta\vartheta/2 \\ 0 & \text{otherwise} \end{cases}. \quad (\text{B.1})$$

Then we estimate the average  $\xi_{\pm}(\vartheta)$  for source pairs within the bin  $(\bar{\vartheta}, \Delta\vartheta)$  by

$$\widehat{\xi}_{\pm}(\bar{\vartheta}, \Delta\vartheta) = \frac{\sum_{i,j=1}^{n_s} w_i w_j \Delta_{ij}^{ss}(\bar{\vartheta}, \Delta\vartheta) (\epsilon_{t,i} \epsilon_{t,j} \pm \epsilon_{\times,i} \epsilon_{\times,j})}{\sum_{i,j=1}^{n_s} w_i w_j \Delta_{ij}^{ss}(\bar{\vartheta}, \Delta\vartheta)}, \quad (\text{B.2})$$

where  $\epsilon_{t,i}$  and  $\epsilon_{\times,i}$  refer to the tangential components of the shear estimator of the  $i$ th or  $j$ th source in the pair  $ij$  relative to  $\vartheta = \theta_i^s - \theta_j^s$ , and likewise for  $\epsilon_{\times,i}$  and  $\epsilon_{\times,j}$  (Schneider et al. 2002).

Second, we estimate the mean tangential shear  $\bar{\gamma}_t(\vartheta) = \langle \gamma_t(\theta^d + \vartheta) | \theta^d \rangle$  of sources at separation  $\vartheta$  from lenses located at  $\theta^d$  by

$$\widehat{\gamma}_t(\bar{\vartheta}, \Delta\vartheta) = \frac{\sum_{i=1}^{n_d} \sum_{j=1}^{n_s} w_j \Delta_{ij}^{ds}(\bar{\vartheta}, \Delta\vartheta) \epsilon_{t,j}}{\sum_{i=1}^{n_d} \sum_{j=1}^{n_s} w_j \Delta_{ij}^{ds}(\bar{\vartheta}, \Delta\vartheta)} - \widehat{\gamma}_t^{\text{rand}}(\bar{\vartheta}, \Delta\vartheta), \quad (\text{B.3})$$

where now  $\epsilon_{t,j}$  is the tangential component of  $\epsilon_j$  relative to  $\vartheta = \theta_i^d - \theta_j^s$ , and  $\widehat{\gamma}_t^{\text{rand}}(\bar{\vartheta}, \Delta\vartheta)$  is the first term on the right-hand side of (B.3) for a large sample of random lens positions (Singh et al. 2016).

Third, for the correlation function  $\omega(\vartheta) = \langle \kappa_g(\theta + \vartheta) \kappa_g(\theta) \rangle$  of the lens clustering on the sky, we employ the estimator in Landy & Szalay (1993),

$$\widehat{\omega}(\bar{\vartheta}, \Delta\vartheta) = \frac{dd(\bar{\vartheta}, \Delta\vartheta)}{rr(\bar{\vartheta}, \Delta\vartheta)} - 2 \times \frac{dr(\bar{\vartheta}, \Delta\vartheta)}{rr(\bar{\vartheta}, \Delta\vartheta)} + 1, \quad (\text{B.4})$$

where  $dd$  is the normalised number of lens pairs in the separation bin,  $rr$  the normalised number of pairs with random positions  $\theta_i^r$  out of  $n_r \gg n_d$  in total, and  $dr$  is the normalised number of lens-random pairs:

$$\begin{aligned} dd(\bar{\vartheta}, \Delta\vartheta) &= \sum_{i,j=1}^{n_d} \frac{\Delta_{ij}^{dd}(\bar{\vartheta}, \Delta\vartheta)}{n_d^2}; \\ rr(\bar{\vartheta}, \Delta\vartheta) &= \sum_{i,j=1}^{n_r} \frac{\Delta_{ij}^{rr}(\bar{\vartheta}, \Delta\vartheta)}{n_r^2}; \quad dr(\bar{\vartheta}, \Delta\vartheta) = \sum_{i,j=1}^{n_d, n_d} \frac{\Delta_{ij}^{dr}(\bar{\vartheta}, \Delta\vartheta)}{n_d n_r}. \end{aligned} \quad (\text{B.5})$$

To combine the estimates from  $n_{\text{patch}}$  different patches, we merge their lens and source catalogues with constant position offsets for each patch such that we never have pairs of galaxies from different patches inside a separation bin. The probability to find a random-lens position inside a particular patch in the merged catalogue is proportional to the effective, unmasked area of the patch, which is always  $16 \text{ deg}^2$  for the mock data. For the analysis of the 64 patches mock-data, we use as angular binning 5000 linear bins between  $1.4 \text{ arcsec}$  and  $5.7 \text{ deg}$ .

We transform the estimates of the three two-point correlation functions into estimates of the aperture statistics for several  $\theta_{\text{ap}} \in [1', 140']$  by a numerical integration of the following equations

$$\left. \begin{aligned} \langle M_{\text{ap}}^2 \rangle(\theta_{\text{ap}}) \\ \langle \mathcal{N} M_{\text{ap}} \rangle(\theta_{\text{ap}}) \\ \langle \mathcal{N}^2 \rangle(\theta_{\text{ap}}) \end{aligned} \right\} = \int_0^\infty dx \, x \times \begin{cases} \frac{1}{2} (\xi_+(x\theta_{\text{ap}}) T_+(x) + \xi_-(x\theta_{\text{ap}}) T_-(x)) \\ \bar{\gamma}_t(x\theta_{\text{ap}}) F(x) \\ \omega(x\theta_{\text{ap}}) T_+(x) \end{cases} \quad (\text{B.6})$$

based on the auxiliary functions

$$\left. \begin{aligned} T_{+,-}(x) \\ F(x) \end{aligned} \right\} = (2\pi)^2 \int_0^\infty ds \, s \, I^2(s) \times \begin{cases} J_{0,4}(sx) \\ J_2(sx) \end{cases} \quad (\text{B.7})$$

with analytic expressions for  $T_{\pm}(x)$  and  $F(x)$  as in Simon et al. (2007). Because of the lower cutoff at  $1.4 \text{ arcsec}$  in the correlation functions (we set them zero here), we cannot use values of the aperture statistics below around two arcmin where the transformation bias grows to about 10 per cent (Kilbinger et al. 2006). To estimate the statistical errors or covariances between the three aperture statistics and angular scales  $\theta_{\text{ap}}$ , we employ the jackknife technique with  $n_{\text{patch}}$  sub-samples that we obtain by removing one patch from the merged catalogue at a time (Friedrich et al. 2016).

In Fig. 2, we plot estimates of  $\langle M_{\text{ap}}^2 \rangle(\theta_{\text{ap}})$  in our mock data as points with statistical errors obtained with the jackknife technique (inflated by a factor of five). The three different styles of the data points are for: (i) shear with shape noise of sources (solid squares); (ii) reduced shear with shape noise (open circles); and (iii) shear without shape noise (solid triangles). The data points are a very good match to a theoretical model GG for the MS cosmology (blue solid line), and they are consistent with



each other at the same  $\theta_{\text{ap}}$ . The statistical errors of data without shape noise are similar to those for sources with shape noise for  $\theta_{\text{ap}} \gtrsim 10'$  which indicates that cosmic variance dominates in this regime for our fiducial survey.

### Appendix C: Non-Gaussianity of measurement errors

In this appendix, we test for a non-Gaussian distribution of statistical errors in the aperture statistics  $\langle \mathcal{N}^2 \rangle(\theta_{\text{ap}})$ ,  $\langle \mathcal{NM}_{\text{ap}} \rangle(\theta_{\text{ap}})$ , and  $\langle M_{\text{ap}}^2 \rangle(\theta_{\text{ap}})$  with a one-dimensional Kolmogorov-Smirnov (KS) test. We perform the KS tests separately for each aperture statistics, denoted by  $x$  in the following, and the aperture scales  $\theta_{\text{ap}} \in \{2', 20', 60', 120'\}$ . Since we have only one simulated lensing survey with  $1024 \text{ deg}^2$  of data, we split the data into independent patches and test the empirical distributions of measurements  $x_i$  in  $n = 64$  patches of area  $4 \times 4 \text{ deg}^2$  each. We standardise the measurements by computing  $z_i = (x_i - \bar{x})/\sigma_x$ , where  $\bar{x}$  and  $\sigma_x$  are the mean and standard deviation, respectively, of the sample  $\{x_i : i = 1 \dots n\}$ . For the KS test, we then compare the distribution  $F_n(z) = n^{-1} \sum_{i=1}^n I(z_i - z)$  in the mock data to the average distribution  $F(z)$  of  $n$  normally distributed measurements using the test statistic  $D_n = \sup_z \{|F_n(z) - F(z)|\}$ ; here we define the function  $I(z) = 1$  for  $z \leq 0$  and  $I(z) = 0$  otherwise.

The resulting  $p$ -values of our  $D_n$  are listed in Table B.1;  $p$ -values in boldface are smaller than 0.05 and indicate a conflict with a Gaussian distribution (95% CL). We perform the test for each galaxy sample and redshift bin. For every galaxy sample, we make new realisations of the source catalogues by randomly changing the source positions in the patch and the intrinsic shapes. This explains the differences in the test results for  $\langle M_{\text{ap}}^2 \rangle$  at identical angular scales. While we expect some failures of the KS test by chance, tensions are clearly visible for  $\langle M_{\text{ap}}^2 \rangle$  at  $\theta_{\text{ap}} \gtrsim 60'$  and for  $\langle \mathcal{N}^2 \rangle$  of the strongly clustered sample RED low- $z$ .

In summary, for  $\langle \mathcal{N}^2 \rangle$  and  $\langle \mathcal{NM}_{\text{ap}} \rangle$  a Gaussian likelihood of errors is a fair approximation, whereas for  $\langle M_{\text{ap}}^2 \rangle$  and around degree scales or more, non-Gaussian features in the error distribution, mainly cosmic variance, are detectable. We note that evidence for non-Gaussian distributions does not necessarily mean that a Gaussian likelihood is an insufficient approximation for a shear analysis.

### Appendix D: Template parameters of reconstructed biasing functions

Table D.1 and the Figs. D.2 and D.1 summarise the posterior distribution of template parameters that are the basis for the inferred biasing function shown in the Figs. 7 and 8. The high uncertainties of most parameters therein reflect the high degeneracy of the template model. We see weak trends for the mean biasing function  $b(m)$  in Fig. D.1: galaxies with low stellar masses or blue galaxies prefer a relatively high number of galaxies inside halos below  $\sim 10^{13} h^{-1} \text{ M}_{\odot}$  while higher stellar masses or red galaxies are underrepresented in this regime; see in particular the RED high- $z$  sample. The excess variance  $V(m)$ , shown in Fig. D.2, is almost always consistent with a Poisson variance although a very tentative sub-Poisson variance may be visible just below  $m_{\text{piv}}$  in some cases (SM3 or SM4, for instance), but usually gets smeared out by the uncertainty of  $m_{\text{piv}}$ .

**Table B.1.** Results of KS-test for Gaussianity for three kinds of the aperture statistic at scales  $\theta = 2, 20, 60, 120$  arcmin (in this order). Quoted are the  $p$ -values of the test statistic. Values  $p \leq 0.05$  indicate a tension with a Gaussian distribution at 95% confidence or higher (bold face). The tests use the empirical distribution of the aperture statistics in 64 fields of our mock data with  $4 \times 4 \text{ deg}^2$  area each. Realisations of the source shape-noise and positions are different for each lens sample.

Sample <sup>a</sup>	$\langle \mathcal{N}^2(\theta) \rangle^b$				$\langle \mathcal{N}M_{\text{ap}}(\theta) \rangle^c$				$\langle M_{\text{ap}}^2(\theta) \rangle^d$			
SM1 low- $z$	0.54	0.08	0.35	0.16	0.44	0.28	0.06	0.05	<b>0.01</b>	<b>0.02</b>	<b>0.00</b>	<b>0.01</b>
SM2 low- $z$	0.52	0.23	0.97	0.35	0.71	0.90	0.25	0.06	0.31	<b>0.04</b>	0.06	<b>0.01</b>
SM3 low- $z$	<b>0.04</b>	0.18	0.35	<b>0.00</b>	0.44	0.74	0.61	0.84	0.76	0.28	<b>0.03</b>	<b>0.00</b>
SM4 low- $z$	0.08	0.16	0.20	0.76	0.86	0.94	0.23	<b>0.01</b>	0.41	0.05	0.07	0.16
SM5 low- $z$	0.52	0.05	0.95	0.16	0.16	<b>0.04</b>	0.31	<b>0.01</b>	0.16	0.20	0.20	0.16
SM6 low- $z$	0.22	0.44	0.65	0.82	0.08	0.18	0.84	0.08	0.12	0.22	<b>0.02</b>	<b>0.00</b>
RED low- $z$	0.31	<b>0.00</b>	<b>0.00</b>	<b>0.00</b>	0.67	<b>0.02</b>	0.56	<b>0.00</b>	0.06	<b>0.03</b>	<b>0.02</b>	0.06
BLUE low- $z$	0.47	0.96	0.47	0.71	0.77	0.89	0.12	0.77	0.31	0.07	0.20	0.05
SM1 high- $z$	0.08	0.07	0.93	0.28	0.33	0.44	<b>0.02</b>	0.24	0.24	0.08	<b>0.00</b>	<b>0.00</b>
SM2 high- $z$	0.57	0.37	0.50	0.44	0.79	0.64	0.44	0.41	0.31	0.12	<b>0.00</b>	<b>0.01</b>
SM3 high- $z$	1.00	0.28	0.12	0.89	0.84	0.23	0.06	0.87	0.44	<b>0.04</b>	<b>0.04</b>	<b>0.00</b>
SM4 high- $z$	0.50	0.44	0.50	0.06	0.94	0.50	0.96	0.64	0.08	0.22	<b>0.00</b>	<b>0.00</b>
SM5 high- $z$	0.71	0.13	0.61	<b>0.01</b>	0.47	0.24	0.71	<b>0.00</b>	0.86	0.06	<b>0.00</b>	0.44
SM6 high- $z$	0.64	0.08	0.64	0.18	0.52	0.86	0.61	0.23	0.52	<b>0.01</b>	0.06	0.18
RED high- $z$	0.07	0.41	0.20	<b>0.00</b>	0.41	0.05	0.41	0.54	0.31	0.20	0.25	<b>0.00</b>
BLUE high- $z$	0.08	0.67	0.08	0.55	0.46	0.22	0.63	<b>0.02</b>	0.86	0.17	0.55	0.08

**Notes.** <sup>(a)</sup> mock sample used in analysis (lenses); <sup>(b)</sup> variances of aperture number count for sequence of aperture scales; <sup>(c)</sup> sequence of covariances between aperture number count and aperture mass; <sup>(d)</sup> sequence of variances of aperture mass

**Table D.1.** Summary of estimated model parameters in our simulated lensing analysis for the various galaxy samples and redshift bins. The quoted values are medians and 68% PIs of the marginal posterior distributions. The statistical errors assume our fiducial survey for sources including shape noise.

Sample <sup>a</sup>	$\log_{10} (\bar{n}_g/h^3\text{Mpc}^{-3})^b$	$b_{\text{ls}}^c$	$\log_{10} (m_{\text{piv}}/h^{-1}\text{M}_{\odot})^d$	$f_{\text{cen}}^e$
SM1 low- $z$	$-1.69^{+1.38}_{-0.51}$	$1.00^{+0.05}_{-0.05}$	$12.44^{+0.74}_{-1.29}$	$0.59^{+0.27}_{-0.32}$
SM2 low- $z$	$-2.08^{+0.42}_{-0.26}$	$1.09^{+0.05}_{-0.05}$	$12.92^{+0.39}_{-0.60}$	$0.75^{+0.17}_{-0.29}$
SM3 low- $z$	$-2.69^{+0.17}_{-0.16}$	$1.19^{+0.05}_{-0.05}$	$13.52^{+0.24}_{-0.27}$	$0.86^{+0.09}_{-0.15}$
SM4 low- $z$	$-3.07^{+0.23}_{-0.32}$	$1.28^{+0.05}_{-0.06}$	$13.80^{+0.49}_{-0.32}$	$0.82^{+0.12}_{-0.18}$
SM5 low- $z$	$-3.48^{+0.18}_{-0.26}$	$1.35^{+0.06}_{-0.06}$	$14.26^{+0.31}_{-0.30}$	$0.80^{+0.13}_{-0.17}$
SM6 low- $z$	$-3.66^{+0.20}_{-0.18}$	$1.55^{+0.06}_{-0.07}$	$14.31^{+0.34}_{-0.32}$	$0.82^{+0.11}_{-0.15}$
BLUE low- $z$	$-1.97^{+0.32}_{-0.24}$	$0.93^{+0.04}_{-0.05}$	$13.06^{+0.61}_{-0.53}$	$0.69^{+0.21}_{-0.29}$
RED low- $z$	$-3.37^{+0.21}_{-0.14}$	$1.30^{+0.08}_{-0.06}$	$14.00^{+0.31}_{-0.21}$	$0.90^{+0.07}_{-0.10}$
SM1 high- $z$	$-0.86^{+0.65}_{-1.31}$	$1.09^{+0.04}_{-0.04}$	$11.89^{+1.30}_{-0.87}$	$0.56^{+0.28}_{-0.32}$
SM2 high- $z$	$-0.51^{+0.35}_{-0.86}$	$1.15^{+0.04}_{-0.04}$	$11.43^{+0.93}_{-0.52}$	$0.52^{+0.31}_{-0.33}$
SM3 high- $z$	$-2.57^{+0.29}_{-0.31}$	$1.28^{+0.04}_{-0.04}$	$13.31^{+0.41}_{-0.32}$	$0.70^{+0.20}_{-0.27}$
SM4 high- $z$	$-3.13^{+0.24}_{-0.32}$	$1.34^{+0.04}_{-0.04}$	$13.85^{+0.44}_{-0.28}$	$0.85^{+0.10}_{-0.18}$
SM5 high- $z$	$-3.44^{+0.17}_{-0.30}$	$1.53^{+0.05}_{-0.05}$	$14.09^{+0.46}_{-0.34}$	$0.79^{+0.14}_{-0.18}$
SM6 high- $z$	$-3.82^{+0.21}_{-0.22}$	$1.61^{+0.07}_{-0.07}$	$14.41^{+0.34}_{-0.27}$	$0.90^{+0.07}_{-0.11}$
BLUE high- $z$	$-0.42^{+0.28}_{-0.41}$	$1.11^{+0.04}_{-0.03}$	$11.34^{+0.57}_{-0.48}$	$0.51^{+0.32}_{-0.32}$
RED high- $z$	$-3.55^{+0.32}_{-0.81}$	$1.62^{+0.07}_{-0.08}$	$14.13^{+0.82}_{-0.34}$	$0.88^{+0.08}_{-0.14}$

**Notes.** <sup>(a)</sup> sample used for the emulated lensing analysis; SM samples are selected in stellar mass, RED and BLUE are selected by colour (see Table 1); low- $z$  samples have a mean redshift of  $\bar{z} \approx 0.36$ , high- $z$  samples have  $\bar{z} \approx 0.52$ ; <sup>(b)</sup> mean galaxy number-density (comoving); <sup>(c)</sup> large-scale bias factor; <sup>(d)</sup> pivital halo mass; <sup>(e)</sup> fraction of halos with central galaxies (*not* the fraction of central galaxies)

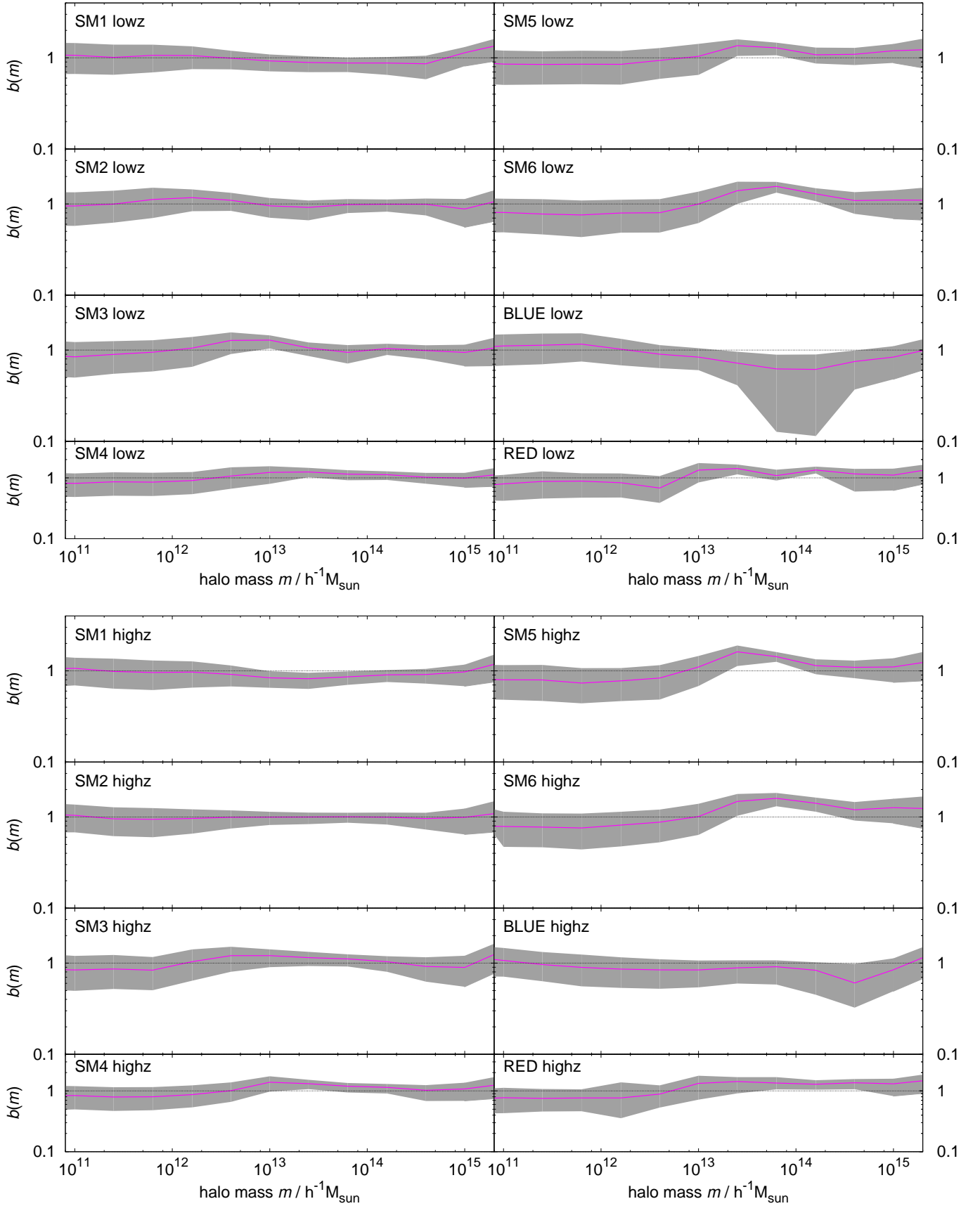


**Fig. D.1.** Mean biasing function  $b(m)$  for the mock galaxy samples SM1 to SM6 and the colour-selected samples BLUE and RED in the low- $z$  (top) and high- $z$  (bottom) redshift bin. The shaded regions indicate the 68% PI about the median for our fiducial mock survey.

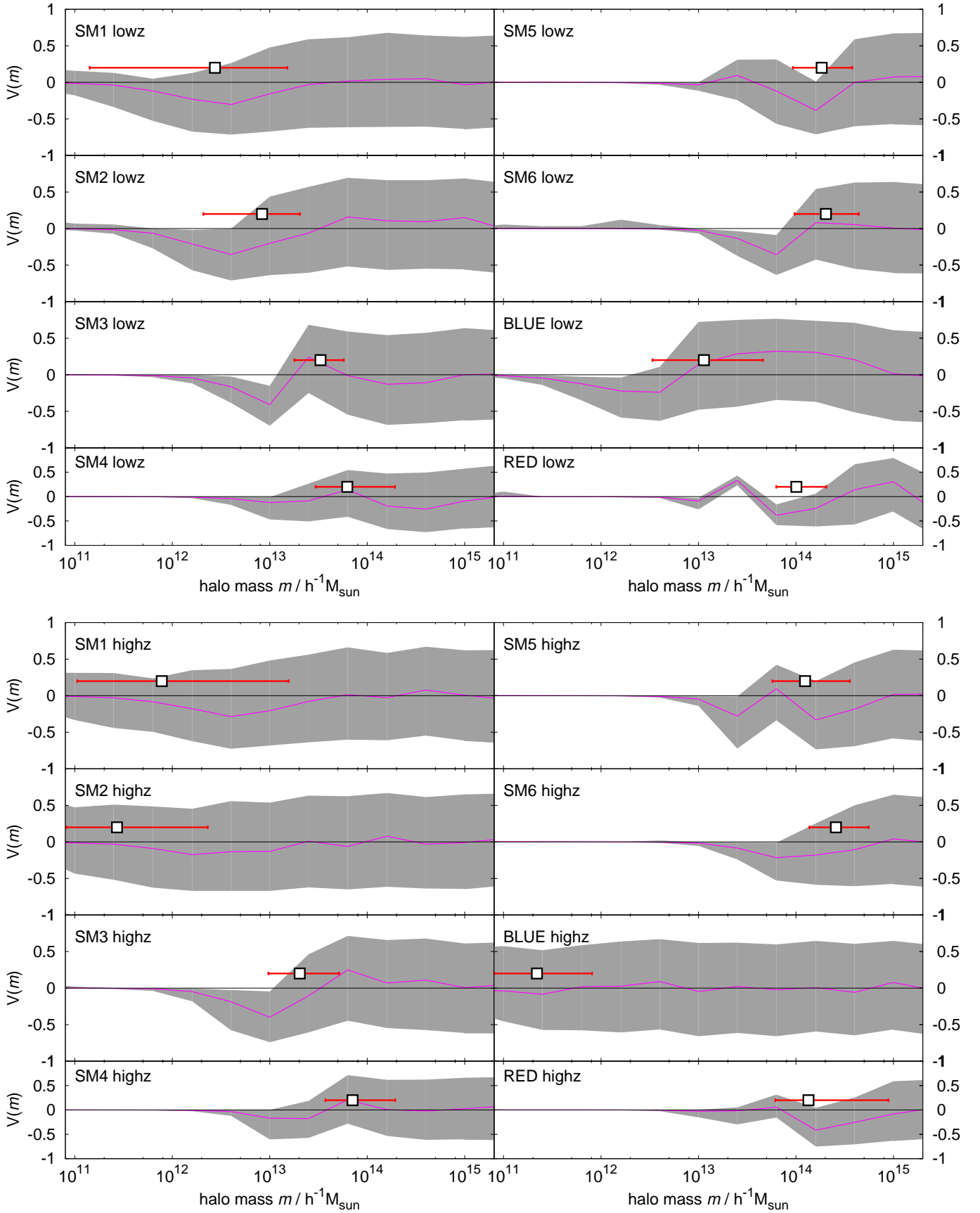


**Fig. D.2.** Excess variance  $V(m)$  for the mock galaxy samples SM1 to SM6 and the colour-selected samples BLUE and RED in the low- $z$  (top) and high- $z$  (bottom) redshift bin. The shaded regions indicate the 68% PI about the median for our fiducial mock survey. For each panel, the open square shows the median mass-scale of the pivotal mass  $m_{\text{piv}}$  and its errorbars the 68% PI.